NEGATIVE HYPERON AND MULTIPLE STRANGE PARTICLE PRODUCTION IN K^-p INTERACTIONS AT 6 GEV/C

by

LEONARD KEITH SISTERSON

A Thesis presented for the
degree of Doctor of Philosophy
in the University of London.

Department of Physics,
Imperial College of Science
and Technology,
London S.W.7.
March 1967

ABSTRACT

This thesis contains some of the results obtained from a Hydrogen Bubble Chamber Experiment with a beam of 6 Gev/c K^- mesons. A brief description is given of the beam and bubble chamber and of the techniques used in the data analysis. The experimental data considered here was obtained from those events in which either three strange particles were produced or a negative hyperon was produced. Ideas based on the simple peripheral and double peripheral model are used to give a simple physical picture of the angles involved in the analysis. In the case of three strange particle events emphasis is placed on the production properties of the φ meson which are considered in some detail in the final chapter. The systematics of the production angular distributions of the negative hyperons are examined and an enhancement in the effective mass of $Y_1^{*\pm}(1385)\pi^{\mp}$ is noted, but it is not possible to ascertain its precise nature.

CONTENTS

PREFACE

The author joined the bubble chamber film analysis group at Imperial College in October 1963 and gained initial experience by assisting in the routine work for experiments with 4 Gev/c π^+p and 3.5 Gev/c K^-p interactions. The present experiment with K^- mesons at 6 Gev/c was started in the summer of 1964 and the author was present at some of the bubble chamber runs, assisting in film quality control. He took part in scanning the Imperial College quota of film, a process that took about seven months, and he was responsible for the practical setting up of much of the programming system used in the analysis. Besides this he wrote or modified a number of minor programs which were required to perform some of the thousand and one minor tasks which an experiment such as this in practice involves.

The author was responsible for the analysis of those events in which at least two strange particle decays were observed.

CHAPTER ONE

INTRODUCTION

The experiment described in this thesis was undertaken by six separate groups working in collaboration. These were the bubble chamber groups at the Universities of Birmingham, Glasgow and Oxford, Imperial College, the Rutherford Laboratory and the Max Planck Institüt für Physik und Astrophysik at Munich. The five British groups had previously collaborated in a K^-p experiment at 3.5 Gev/c, so that the present experiment may be regarded as a continuation of the study of K^-p interactions at high energies.

One specific motivation for performing this experiment was to search for the Ω^- particle predicted by SU(3) symmetry theory. To some extent this motive was removed, or at least its priority was lowered, by the publication(1), while this experiment was still in its early stages, of an event definitely identified as Ω^- production and decay. Since then several such events have been published, including one from this experiment(2), so that the existence of the Ω^- is now well established. Correspondingly, the belief in the fundamental correctness of SU(3) has also been strengthened. Although the Ω^- is, of course, a negative hyperon its production is not considered in this thesis.

The aim of the present work is to present the results of an examination of those events in which either three strange particles are produced or a Ξ^- or negative hyperon is produced. In the case of the three strange particle final states the $K\bar{K}$ system and in particular the φ meson is found to be most interesting, so φ production is considered in some detail.

The basic properties of Feynman diagrams have been found useful as a picture on which to base the experimental analysis. Three basic types are used, the s-, t-, and u-channel diagrams. As examples we can cite:-

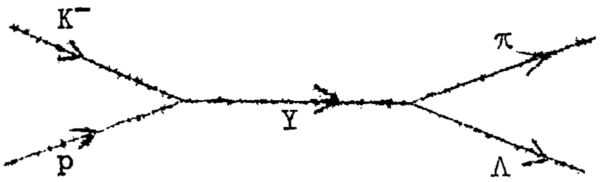

s - channel

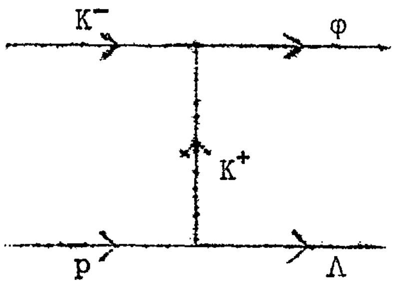

t - channel

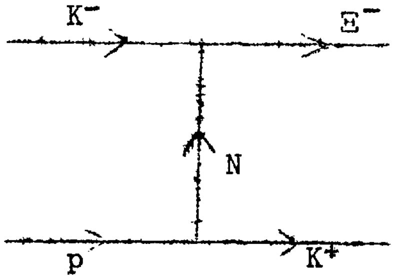

u - channel

the most useful of these being the t- and u- channel diagrams (e.g. see chapters 4 and 5). The t- (and u-) channel diagram corresponds to the peripheral or Born Term model(3) which is simply a lowest order pertubation theory calculation. It should be remembered that the external lines need not correspond to single particles and that these are only the lowest order diagrams. Since the perturbation theory expansion of strong interactions does not converge, the higher order diagrams ought to swamp the lowest. This disasterous fact is ignored in strong interaction physics as the lowest order diagrams give a useful qualitative description of the physical facts.

The majority of bubble chamber experiments are very much alike as regards the process of extracting physical information about the interactions being studied. Thus the following résumé of such an experiment would fit the work being done by most bubble chamber groups throughout the world, and its elaboration for this particular experiment forms the subject of the next chapter.

The pictures taken with the bubble chamber are first examined (scanned) by physicists and their assistants for events of the required topology. The specified events are then measured by special measuring machines which produce the measurements in a form such as punched tape suitable for the use of a computer. From the measurements a series of computer programs reconstruct the event in space in terms of the momenta and angles of all the tracks and then test various hypotheses regarding the nature of the event. Events which satisfy the tests of particular hypotheses are then used in the plotting of histograms, graphs and scatter plots in order to obtain information about the nature of the interaction leading to the final state specified by the hypothesis concerned.

Except for special cases such as the search for an Ω^- particle, the physical knowledge learnt from a bubble chamber experiment depends upon the number of events studied i.e. the amount of film taken. Because the bubble chamber is a completely non-selective detecting device - as opposed to counters say, which can be arranged to detect only a specific particle with a particular momentum - in order to study a microscopic state such as the production of φ mesons, a large amount of data has to be examined most of which may not be related to φ meson production. Only after the data has been assembled can that part relating to such a specific process be extracted. For such reasons the statistical significance of the data in many channels is sadly low with the result that statistical errors frequently outweigh all other sources of errors. This is particularly true in a study of multiple strange particle production.

A number of conventions are used in this thesis which it may be useful to define. First, in refering to production angular distributions, the direction taken as forward is always that of the incident K^- meson seen in the overall centre of mass. Secondly, we use units in which c=1, so that momentum, mass and energy are all simply given as Gev, and finally, when specifying a final state which has been kinematically fitted, a K^o,Λ or a Σ^o in brackets means that the decay of that particle was not seen but the particle's presence was inferred from the requirements of momentum and energy conservation.

CHAPTER TWO

BASIC EXPERIMENTAL PROCEDURE

In this chapter a description is given of the beam and the bubble chamber, and of the techniques used in scanning, measuring and data analysis. Possible biases and errors will only be indicated; their detailed treatment is left to the next chapter.

2.1 The Beam

This experiment used the 02 beam at CERN(4) (Fig. 2.1) which was designed to operate with either radiofrequency separators or electrostatic separators, the latter being used to obtain K^- particles at 6 Gev as reported here. The beam had a single stage of separation, as calculations indicated that this would give a higher flux of wanted particles than two stages, while maintaining the muon contamination at an acceptable level, provided that phase space acceptance and momentum bite were redefined after separation. This arrangement in practice gave a muon background of 20 to 30%.

In order to have available the maximum possible particle flux, it is necessary to make use of the strong forward peaking of particles produced in the target by the Proton Synchrotron beam. For the 02 beam this was achieved by placing the target inside one of the magnet units of the P.S., since with this arrangement the beam line accepted particles with essentially zero production angle. During the actual runs the beam was tuned to give about 10 kaons and 3 muons at the bubble chamber per burst.

Details of the value of the beam momentum and its spread and estimates of the pion contamination will be given in the next chapter.

2.2 The Bubble Chamber

The O2 beam was operated in conjunction with the 150 cm. British National Hydrogen Bubble Chamber, technical details of which may be found in References 5, 6, and 7; only a brief description is given here.

The principal feature of interest is the optical system (Fig. 2.2) which was of the 'straight through illumination' type. As a result of the illumination system the volume of chamber visible to each camera was slightly different. Thus the region of illuminated hydrogen common to all three cameras was 64% of the total, while 80% was visible to any combination of two cameras. The linear dimensions of the visible region were approximately 50 x 140 cm. by 50 cm. deep.

Two sets of chamber based fiducial marks were available, one set on the inside of the front glass and another set on the inside of the back glass (Fig. 2.3), while a further camera-based fiducial system was printed onto the film by the glass plates onto which it was sucked to hold it in the correct focal plane. The relative positions of the fiducials on each chamber window are known to ± 10 microns and the lines of the camera based system are known to be straight to within a micron. This accuracy is required to allow accurate calibration of the cameras and optical parameters used by the geometry program.

The magnetic field(7) differed in each run with the chamber.

For the so called D and F run it was 13.54 kg., while for the E run it was 12.267 kg.

Altogether some 390 thousand pictures were taken, though not all were of usable quality. The film was divided equally amongst the six collaborating groups who separately scanned, measured and computed the events found on it. Basic policies for this processing were decided at collaboration meetings, but the actual details of the way they were applied varied from group to group. For this reason the rest of this chapter relates specifically to the work done at Imperial College.

2.3 Scanning and Measuring

Scanning criteria were drawn up to enable events to be classed as specifically as possible.

The film was scanned for all interactions with the exception of those which produced only neutral particles, none of which were seen to decay. In addition tau decays of the beam tracks were noted; these were to be used to determine absolute values of cross-sections. Every event found was described by a topology $AB^{\pm}C$ where

A is the number of charged tracks leaving the production vertex,

B is the number and charge of such tracks that are believed to be strange particle decays: all charged decays were taken to be strange particle decays unless the bubble density and curvature of the track definitely identified the decay as that of a pion.

C is the number of neutral particle decays (V^{0}'s) apparently associated with the event.

An event had to satisfy the following criteria to be recorded in the scan:-

(a) It must have been produced by a beam track. Events arising from incoming tracks making a visible angle on the scanning table with the general beam direction were rejected.

(b) Events with none or only one visible strange particle decay ('common' events) were only noted if they were 'Region A' events. An event was said to lie within region A if (i) the beam entered through the top of the 24cm. by 90cm. region (as measured on the back glass of the chamber) defined on View 2; (ii) the production vertex of the event lay in the region and (iii) any decay lay within the 32cm. by 102 cm. region (Fig. 2.3). Any other event was said to be in Region B.

(c) Events with more than one visible strange particle decay ('rare' events) and tau decays of the beam track were noted wherever they occurred, together with their region, A or B.

The scanning of V^o's posed two problems. First, the association or non-association of a V^o with an event had to be assessed. A V^o was assigned to an event if its line of flight, as estimated on the scanning table, passed within 2cm. of the production vertex or a negative decay. This very loose criterion was adopted in order to include Ξ^o decays. Secondly, to avoid unnecessary measurement, electron pairs were to be distinguished from V^o's where possible. If the opening angle was greater than 3^o on all views the pair of tracks was classified as a V^o; if less than 3^o then they were classified as a V^o if neither of the tracks was obviously an electron (from bubble density and curvature) and if the ratio of the momentum of the positive track to that of the negative track was approximately 3. This latter condition was invoked in order to avoid loss of fast Λ particles which decayed with the proton going backwards in the centre of mass of the Λ.

Other useful information recorded while scanning were the presence of stopping protons, stopping $\pi \to \mu \to e$ decays and Dalitz pairs. If the length of a track before decay was less than 3 mm. on all views this fact was recorded. These events were not measured because such short tracks do not allow an accurate determination of their direction.

British National scanning tables, which had a magnification of 10, were used for scanning. Three scans were made, the first two being independent, while the third scan checked the results of the previous two, especially the discrepancies. A card containing the frame number, topology, and a sketch of the event to aid the measurer, plus any other information considered useful, was filled in for every event verified by this scan.

Measurement of the scanned events was made with digitised measuring machines. X and Y coordinate pairs, together with sufficient information to identify them, were punched on paper tape in the form of octal numbers. The least count of the digitiser was 2 microns on the film. For more detailed descriptions of these machines see for example References 8 and 9. The measurement of an event involved the measurement of five specified fiducial marks, the vertices and a series of points along each of the tracks on all three stereoscopic views of the event.

The measurements thus obtained were processed by a series of computer programs to give information about the physical nature of the event.

2.4 Data Analysis

The first step was to transfer the information on paper tape to magnetic tape by means of an Elliot paper tape reader coupled to an I.B.M. 1401 computer. A program called PING, run on an I.B.M. 7090 computer, was then used to organise the measurements into a form suitable for input to the geometry program. PING performed elementary checking operations on the labelling of the measurements and rejected incorrectly labelled events, converted the octal numbers of the measured points to decimal numbers, and wrote the events which passed its tests onto a magnetic tape in the format used by the geometry program.

The Geometry Program

This was the first major program used in the data processing. It was originally written by the staff of the Rutherford Laboratory and modified during the course of this experiment at Imperial College (by Mrs. M. Acraman). A detailed description of the mathematical methods used by the program can be found in Reference 10 and the practical running of the program in Reference 11, only an outline of these being given here.

The aim of the program is to calculate the vector momentum of all the tracks and the space coordinates of the vertices, together with their errors, and to write these on magnetic tape in a form useful both for book-keeping and hypothesis testing.

First, a set of expected fiducial positions is supplied for each view in a standard reference frame for that view. The measured set of fiducials is then fitted by a least squares procedure to the corresponding standard set and the transformation coefficients thus found are used to transform all measured points on the view to the standard reference frame. After this transformation, all the film points are converted to rays defined by the point at which the ray cuts the front-glass liquid interface and the direction cosines of the ray with respect to the x and y axes of the chamber.

The method of corresponding points is then used to find space points on each track(12). A 'best' view is selected for each track, and for each ray on this view corresponding rays are determined on each of the other views. A weighted mean of the points of intersection of these corresponding rays is taken to give the coordinates of the space points. A circle or parabola fit is then made to the x-y projection of the space points and a simple helix fit is made to the z-coordinate. At this stage, tracks which are found to be straight within errors are fitted by a straight line.

Finally, a mass dependent helix is fitted to the measured film points. The best fit helix is obtained by projecting a helix back onto the film plane and minimising $\sum_i d_i^2$ where d_i is the distance from the i^{th} measured point to the image of the helix. The circle or parabola fit already obtained is used to rotate the track so that the standard helix

$$x = \alpha + \rho \cos\theta + C_x(\theta)$$

$$y = \beta + \rho \sin\theta + C_y(\theta)$$

$$z = \gamma + \rho\theta \tan\lambda$$

can be used, where α and β specify the axis, ρ the radius, λ the pitch and γ the z-coordinate at $\theta = 0$. C_x and C_y are mass dependent corrections to allow for the slowing down of the particle by the liquid. The fitting is done three times using C_x and C_y appropriate to the kaon, pion and proton mass in turn. The physical parameters obtained from the helix fit which are used for hypothesis testing are the azimuthal angle, the tangent of the dip angle and the reciprocal of the momentum, all defined at the centre of the track.

Vertex coordinates are determined by projecting a space point onto the film and minimizing

$$\sum_{\substack{\text{Vertex}\\ \text{points}}} \frac{d_{v_i}^2}{\sigma_v^2} + \sum_{\substack{\text{Track}\\ \text{images}}} \frac{d_{T_{ij}}^2}{\sigma_T^2}$$

where d_{v_i} is the distance of the image of the space point from the point measured as the vertex on the i^{th} view, σ_v is a standard error on this quantity, $d_{T_{ij}}$ is the distance of the image of the space point from the i^{th} image of the j^{th} reconstructed track and σ_T is its standard error. If after this fitting $\sum d_{v_i}^2 = \sigma_{nv}^2 > k\sigma_v^2$ and/ or $\sum d_{T_{ij}}^2 = \sigma_{nT}^2 > k\sigma_T^2$, k being a specified constant (typically 2 or 3), then the minimizing process is repeated using σ_{nv} and σ_{nT} in place of σ_v and σ_T.

In the version described in Reference 10, vertex coordinates were determined from vertex points only. At the beginning of this experiment, vertex points and track images were used separately to determine vertex positions, and the one with smaller $\sum d^2$ taken. Towards the end of the experiment the above method was introduced into the program and is now standard.

Originally the program produced a library tape containing the results of the reconstruction only for completely reconstructed events. Towards the end of the experiment a version was introduced which also produced a library tape of events in which one or more tracks could not be reconstructed. This library was used together with new measurements of the failed tracks to produce completely reconstructed events. Thus, whereas previously the whole of an event which failed partially in reconstruction was remeasured, with the new program only individual failed tracks were remeasured, a useful saving of effort.

The Kinematics Program

The events on the library tape were kinematically tested by the Hypothesis Assigning and Testing Program, known briefly as the 'Kinematics Program', written at the Rutherford Laboratory(11,13,14).

Masses are assigned by the program to the tracks of an event by mapping the hypothesis tracks and vertices onto the geometry tracks and vertices in all physically different ways. For example, if the hypothesis tracks are given as $K^-\pi^+\pi^-\pi^+$ the hypothesis will be mapped onto the geometry tracks 1,2,3,4 in the two ways

$$\begin{array}{cccc} 1 & 2 & 3 & 4 \\ K^- & \pi^+ & \pi^- & \pi^+ \end{array} \quad \text{and} \quad \begin{array}{cccc} 1 & 2 & 3 & 4 \\ \pi^- & \pi^+ & K^- & \pi^+ \end{array}$$

Every assignment is tested by performing a least squares fit to momentum and energy conservation at each vertex in turn, then at all vertices simultaneously. The fitting is done by minimising

$$M = \sum_{ij} (x_i - x_i^m)\, G_{ij}\, (x_j - x_j^m) + \sum_k a_k f_k(\underline{x}) \;,$$

the first term being the χ^2 for the fit and where x_i are the kinematical variables, x_i^m are the measured values (from the geometry program) of these variables, G_{ij}^{-1} is the error matrix associated with the x_i^m, a_k are the Lagrangian multipliers and the $f_k(\underline{x})$ satisfy the constraint equations

$$f_k(\underline{x}) = 0 \;.$$

At each vertex there are four constraints (three of momentum and one of energy) so if all parameters are known, i.e. vector momentum of all tracks known, the fit is a four constraint (4C) fit. If there is assumed to be a single missing neutral particle, this has three unknown parameters and the fit is a one constraint (1C) fit. When a fit or hypothesis is described as 4C or 1C in the rest of this thesis, this refers to the number of constraints at the production vertex unless otherwise specified. For each track parameter in a successful fit a quantity known as the normalised Stretch, defined by

$$S_i = \frac{x_i - x_i^m}{\langle \delta(x_i - x_i^m)\, \delta(x_i - x_i^m) \rangle^{\frac{1}{2}}}$$

is calculated. The use of this in detecting systematic errors is discussed in section 3.5.

Given that a minimum was found for M and the constraint equations were satisfied within specified limits, then the fit was said to be successful provided that the probability of χ^2 was greater than 0.001. In the final compilation of data, it was usually necessary to apply a higher cut-off on the probability of χ^2 for reasons which are given in the following chapter. The results of hypothesis testing are written onto a new library tape together with the original geometry information and a summary of these results is printed out for examination by the physicist.

After analysis of the results of kinematic fitting, events which had fits satisfying the selection criteria discussed in section 3.5 were written onto a Data Summary Tape in preparation for the statistics program.

The Statistics Program

This program was also written at the Rutherford Laboratory(15). Its basic operations are those of calculating and histogramming physically valuable quantities from the events which it reads on the Data Summary Tape. The quantities which may be histogrammed are:-

(i)effective masses of all combinations of particles;

(ii)missing mass at the production vertex;

(iii)centre of mass angles and momenta;

(iv)resonance production and decay angles (the Smith and Treiman Yang angles);

(v)hyperon polarisation angles;

(vi)4-momentum transfer.

The missing mass squared at a vertex is defined by

$$M^2 = (\sum E_{in} - \sum E_{out})^2 - (\sum \underset{\sim}{p}_{in} - \sum \underset{\sim}{p}_{out})^2$$

where E_{in} and p_{in} are the energy and momentum of the incoming tracks (including any target proton) and E_{out} and p_{out} are the energy and momentum of the outgoing tracks as given by the geometry program (i.e. before kinematic fitting is attempted).

4- momentum transfer is defined by

$$t = (\underset{\sim}{p}_2 - \underset{\sim}{p}_1)^2 - (E_2 - E_1)^2 = - (m_2^2 + m_1^2) + 2E_1 E_2 - 2p_1 p_2 \cos\theta$$

where E_2 and p_2 are the energy and momentum of the outgoing group of particles at a Feynman vertex, E_1 and p_1 are the energy and momentum of the incoming particle and θ is the production angle, all in the centre of mass of the complete system. This definition makes t positive for most physical processes.

The Smith and Treiman-Yang angles are a set of four angles which have been found useful for analysing resonance production and decay (see for example Reference 16). In the present program they are defined as follows (Fig. 2.4):-

Smith I (S1);

$$\text{Cos (S1)} = \underset{\sim}{I} \cdot \underset{\sim}{D} \qquad \text{(unit vectors)}$$

Smith II (S2);

$$\text{Cos (S2)} = \underset{\sim}{N} \cdot \underset{\sim}{D}$$

Smith III (S3);

$$\text{Cos (S3)} = \underset{\sim}{I} \wedge \underset{\sim}{N} \cdot \underset{\sim}{D}$$

where $\underset{\sim}{I}$ is the direction of the incident K^- as seen in the rest frame of the resonance, $\underset{\sim}{D}$ is the direction of one of the decay particles of the resonance and $\underset{\sim}{N}$ is the normal to the production plane.

The Treiman-Yang angle (T-Y) is the azimuthal angle of $\underset{\sim}{D}$ with respect to $\underline{I} \wedge \underline{N}$ in the plane perpendicular to $\underline{I}$.

These angles are clearly not all independent and in this thesis only Smith I and Treiman-Yang distributions are shown. In each case the cosine of the Smith I is plotted while the Treiman-Yang angle is plotted in radians.

It has been found useful to generalise the Smith I angle slightly and call it the 'scattering angle'. Its definition is the same as above, but it is regarded in a different way and compared to the usual production angle. This is illustrated in Fig. 2.5 and its use is described in chapter 4.

In addition the program permits multiple selection on ranges of effective mass, centre of mass angle and 4-momentum transfer, and two dimensional plots of any of the histogrammed quantities against any other can be produced. The histograms may be produced in either weighted or unweighted form. The method of weighting is discussed in section 3.6.

The program was modified by the Imperial College group to enable unfitted events to be handled. The Data Summary Tape for unfitted events contained fitted information for all decay vertices, but at the production vertex geometrical track parameters were used and a fictitious particle was inserted which had a mass equal to the missing mass and a momentum equal to the missing momentum.

2.5 Determination of Spin Density Matrix Elements

To determine the spin density matrix elements of a resonance from its decay distributions in Smith I and Treiman-Yang angles the 'method of moments' has been used. Writing the Smith I angle as θ and the Treiman-Yang angle as φ, the decay distribution of a 1^- particle into two 0^- particles in terms of the spin density matrix elements is$^{(17)}$

$$W(\theta,\varphi) = \frac{3}{4\pi}\left[\rho_{11}\sin^2\theta + (1-2\rho_{11})\cos^2\theta - \rho_{1\,-1}\sin^2\theta\cos2\varphi - \sqrt{2}\,\mathrm{Re}\,\rho_{10}\sin2\theta\cos\varphi \right]$$

It may then be shown that the matrix elements can be estimated from the experimental distributions in θ and φ by

$$\rho_{11} = \frac{1}{4}\,(3 - 5\overline{\cos^2\theta})$$

$$\rho_{1\,-1} = -\frac{5}{4}\,(\overline{\sin^2\theta\cos2\varphi})$$

$$\mathrm{Re}\,\rho_{10} = -\frac{5}{4\sqrt{2}}\,(\overline{\sin2\theta\cos\varphi})\,.$$

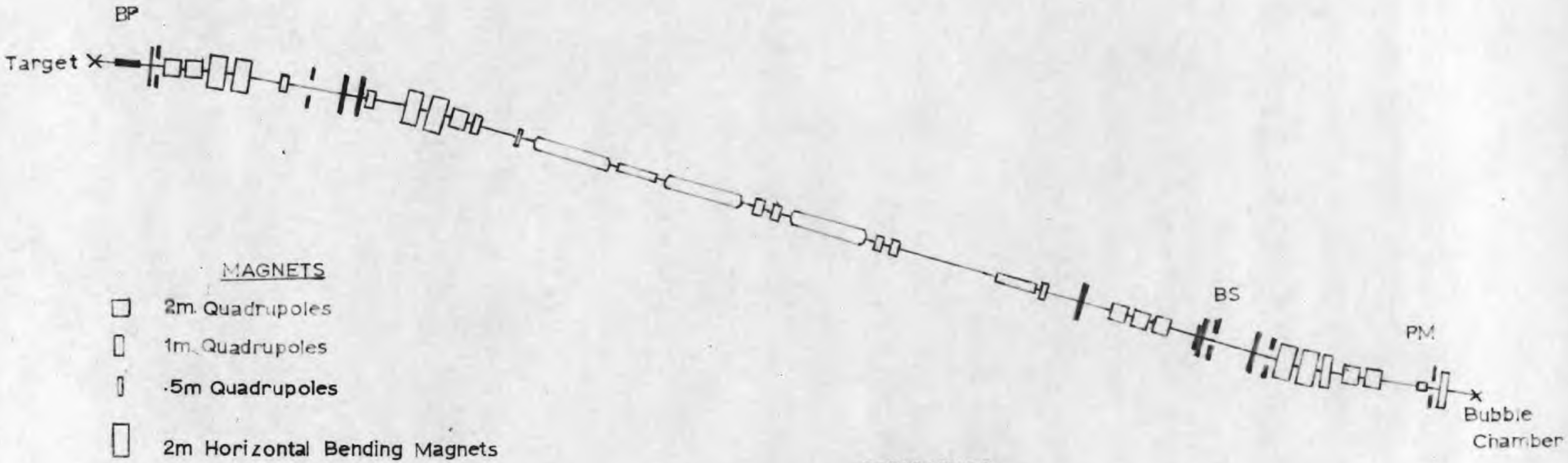

MAGNETS

□ 2m. Quadrupoles
▯ 1m. Quadrupoles
▯ ·5m Quadrupoles
▯ 2m Horizontal Bending Magnets
▯ 1m Vertical Bending Magnet
▫ 1m Pulsed Vertical Bending Magnet

SEPARATORS

▭ Electrostatic Separators
▭ Radiofrequency Separators

COLLIMATORS

▮ Horizontal Collimators
| Vertical Collimators
▮ Beam Stopper (BS)
BP Beam Pipe

Fig. 2.1 LAYOUT OF THE CERN O2 BEAM

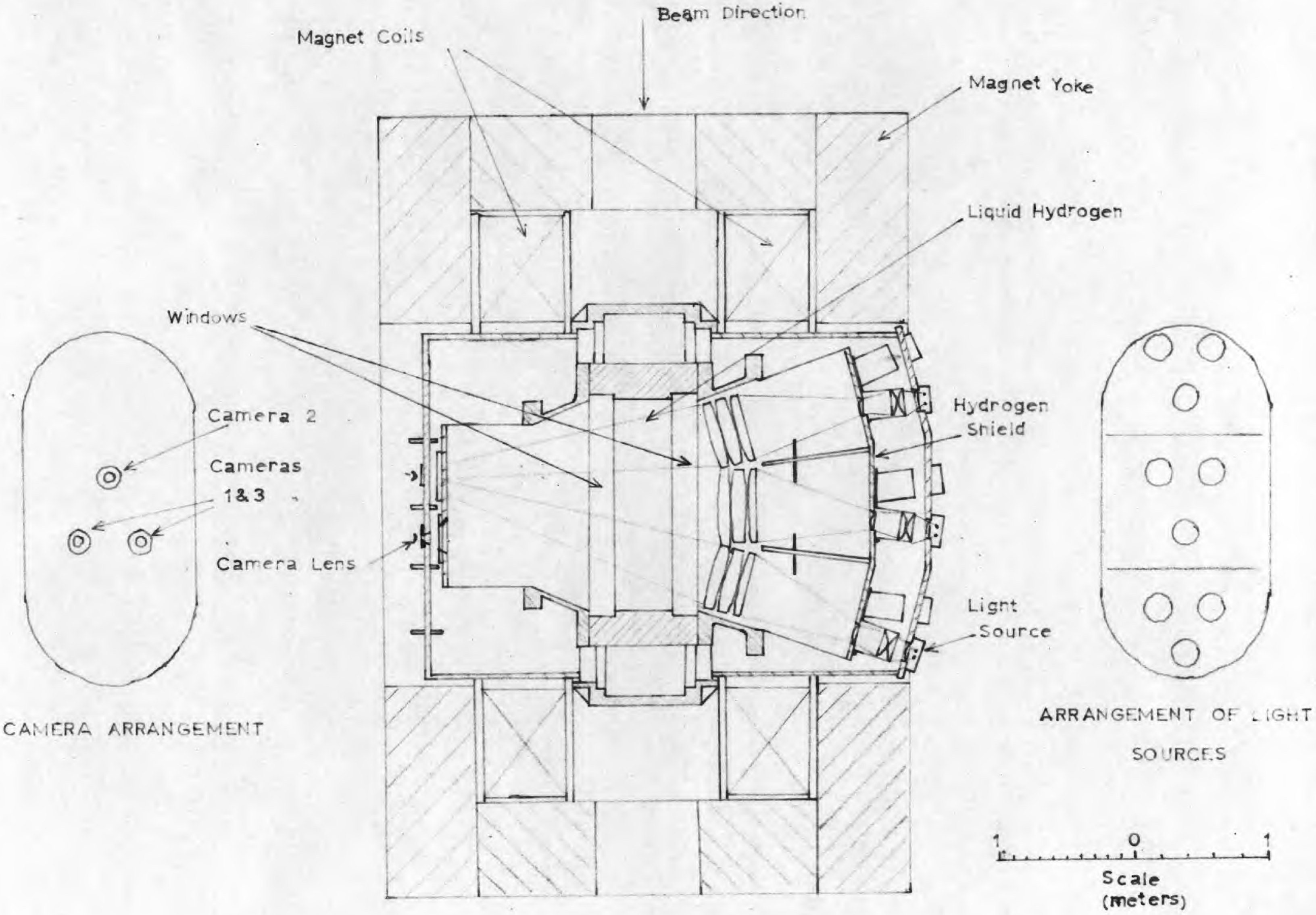

Fig. 2.2 HORIZONTAL SECTION OF THE 150cm. BRITISH HYDROGEN BUBBLE CHAMBER

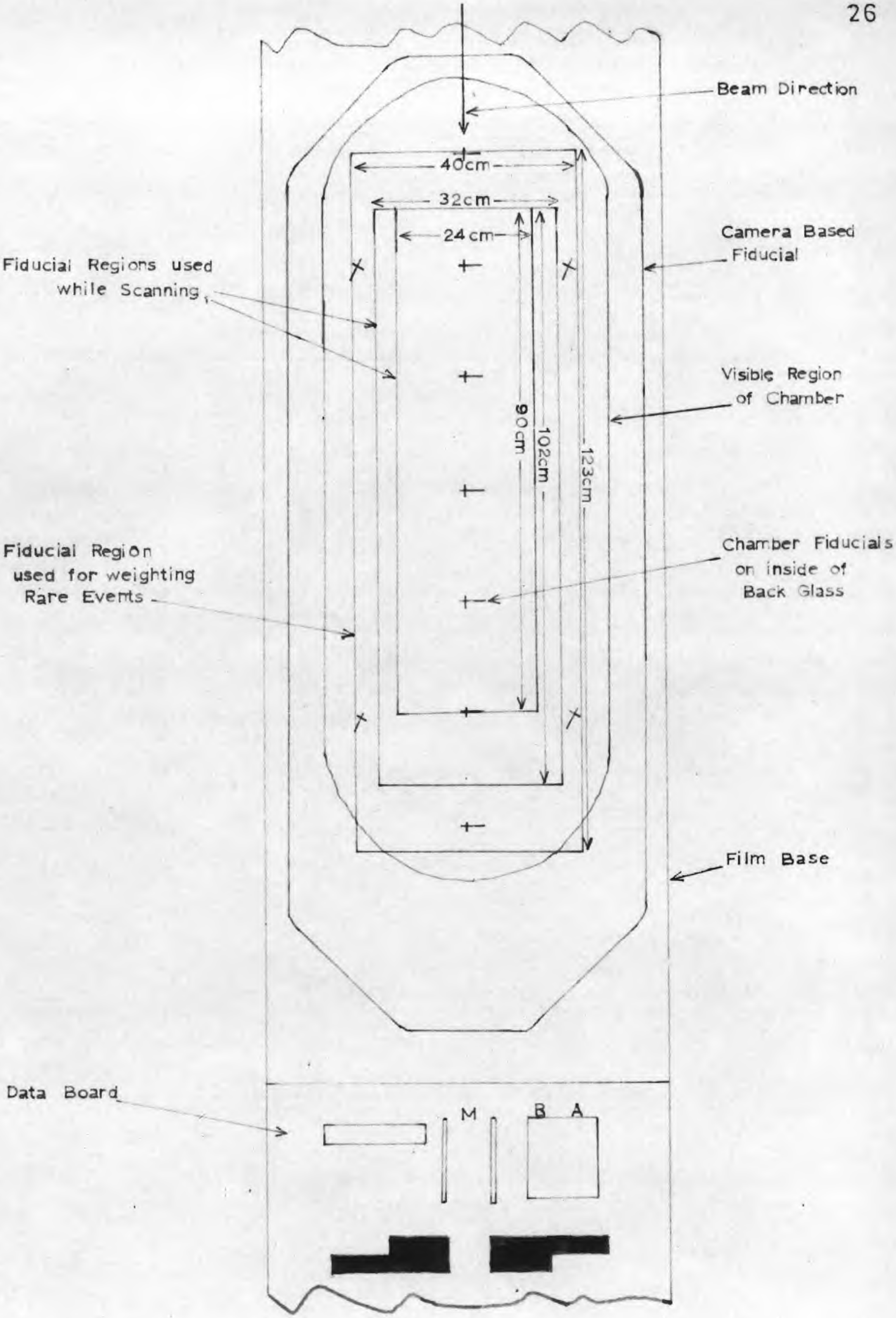

Fig. 2.3 VIEW TWO AND THE FIDUCIAL REGIONS

Fig. 2.4

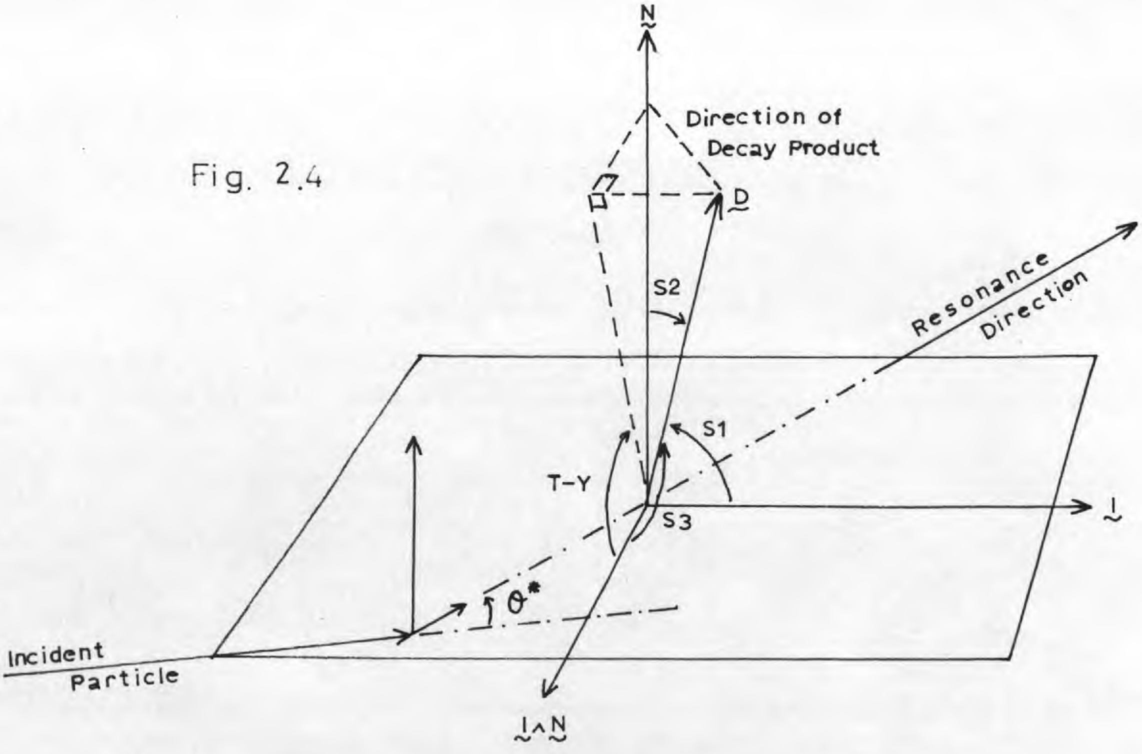

RESONANCE PRODUCTION AND DECAY ANGLES

Fig. 2.5

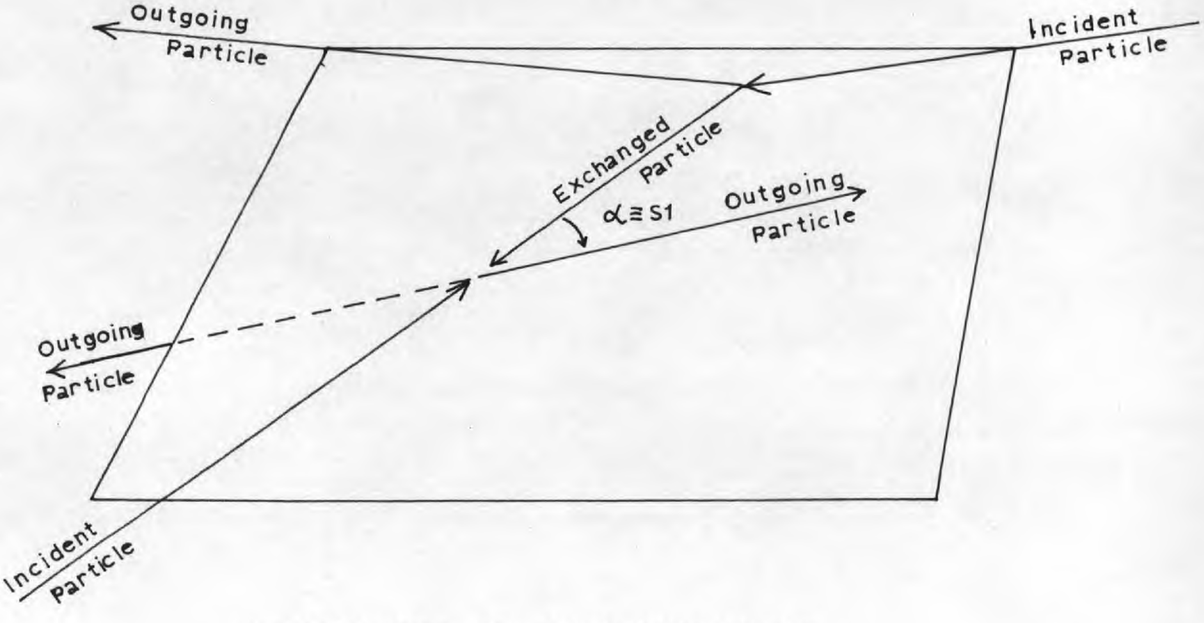

ILLUSTRATION OF SCATTERING ANGLE

CHAPTER THREE

BIASES AND ERRORS

Biases and errors which can affect all events are discussed in this chapter. The following list indicates where they occur:-

1) Constants used in the geometry program
2) Magnetic field in the bubble chamber
3) Beam momentum
4) Scanning
5) Kinematic fitting and event selection
6) Particle decays
7) Beam contamination.

Most of the constants and errors required in the analysis can best be determined at the end of the experiment when all the data is available. As it would have been impractical to recompute and re-analyse all the data, the values used for such quantities as the beam momentum and its error are those determined using a relatively small initial sample of the events, even though much improved values are now available. Besides, the statistical nature of the final results of the experiment are such that quite gross errors would have to be made in order to change them significantly. This, however, is not an argument in favour of laxness on the part of the experimenter as good constants and errors will mean that his results will at least be statistically unbiased even though they be of low statistical significance.

At the end of the chapter the method of calculating cross-sections is discussed.

3.1 Geometry Constants

The optical constants used by the geometry program to reconstruct events were determined by the Oxford group(18). First, any distortions introduced by the camera lenses were estimated by fitting the measured positions of a photographed grid of points to their known positions in space. The points were measured with respect to the camera based fiducial lines using the standard film measuring machines and the photographs of the grid were taken with the cameras removed from the chamber and with the grid placed at distances equal to the camera to front-glass and camera to back-glass separations in turn. When this was done, the camera coordinates and the parameters used in the points to rays conversion formulae were determined by fitting the measured positions on the film of the chamber based fiducial marks to their known positions in space.

The points to rays conversion equations used by the program had the form

$$p = 1 + c_1x + c_2y + c_3r^2 + c_4r^4 \qquad (r^2 = x^2 + y^2)$$

$$X = -b_1pxf(r^2) + b_3$$

$$Y = -b_1pyf(r^2) + b_4$$

$$U = -xf_1(r^2)$$

$$V = -yf_1(r^2)$$

where $(X,Y;U,V)$ are the ray coordinates, (x,y) are the film point coordinates, b_3 and b_4 are the coordinates in the chamber of the optic axis of the camera and b_1 is a magnification. The expression p allows for lens distortion and the functions f and f_1 define the ray tracing through the window of the chamber. The parameter c_3 is that referred to in section 3.5.

The error matrix for the physical parameters calculated by the program depends directly on the root mean square scatter of measured points about a reconstructed track or vertex. To avoid difficulty with bad measurements a cut-off, σ_c, was applied on the R.M.S. scatter. For tracks with a scatter $< \sigma_c$, a standard value, σ_s, the mean of the scatter distribution (Fig. 3.1a), was used, while for tracks with a scatter $> \sigma_c$, the actual value of the scatter was used. Vertices were treated in a similar manner (Fig. 3.1b). In addition tracks with a scatter $> 50\mu$ were rejected and had to be remeasured after careful examination, which frequently revealed that such tracks contained a small angle decay.

3.2 Magnetic Field in the Bubble Chamber

The absolute value of the magnetic field at the centre of the chamber was measured by proton spin resonance with the chamber itself absent; deviations from the central value over the volume of the chamber were measured using the Hall effect(7). As a check that the magnetic field with the chamber in position was correct, the K^o mass was determined from its decay into $\pi^+\pi^-$. An ideogram (Fig. 3.2) of the invariant mass of a sample of V^o's believed to be K^o decays gives a K^o mass of 497.9 ± 0.4 Mev. (The error quoted here is only that due to statistics.) The ideogram also gives an indication of the mass resolution obtained in the experiment.

3.3 Beam Momentum

Having established the magnetic field and optical constants, the beam momentum was determined by reconstructing beam tracks and taking a weighted mean of the calculated momentum for tracks over 50 cm. long. The value obtained was 6.02 Gev for the D and F runs and 6.04 Gev for the E run. The error on this quantity was taken as ± 1% which may be considered as being made up of $\frac{1}{2}$% uncertainty in the mean beam momentum and $\frac{1}{2}$% momentum bite, the latter being an engineering parameter for the beam.

3.4 Scanning

The usual formula for calculating scanning efficiency after a double scan has been made is

$$E = N_{12}(N_1 + N_2 - N_{12}) / N_1 N_2$$

where N_1 is the number of events found in scan 1

N_2 is the number of events found in scan 2

N_{12} is the number of events found in both scans.

To derive this, it was necessary to assume that the probability of seeing an event in a particular scan was the same for all events, which is certainly not true as some events were much clearer than others. Further, especially with rare events, many events were misidentified so that the number of events found in each scan was not straightforward to count. Be this as it may, an application of the formula to the scanning results for various topologies yields efficiencies ranging from about 80% to 100% with multiple vertex (rare) events lying mainly in the lower half of this range. As the value of the efficiency for individual topologies derived by this method is unreliable, all cross-sections derived from rare events have been calculated assuming a 10% scanning loss, and a 5% uncertainty in this is folded into the errors.

The same remarks apply to τ decays of the beam track which are difficult to see because the maximum opening angle for the decay is only $\sim 10^{\circ}$ at 6 Gev. Greater certainty about scanning loss could be obtained by further scans of this film and in fact this was done on a few rolls. The scanners searched only for τ decays in these additional scans, but failed to find a significantly greater number. Superficially, their results did show an increase in the number of decays found, but careful examination of them by a physicist showed that the majority of the new decays were in fact some other kinds of events which the scanner had misidentified as τ decays. The moral of this cautionary tale may well be that when the scanner is searching only for rare events such as τ decays there is a tendency on his or her behalf to give an event the benefit of any doubt. This is permissible, and in fact desirable, when the events are to be subjected to kinematic analysis, but when the appearance on the scanning table is to be the sole guide, much greater care must be taken.

The scanning results for rare events found at Imperial College are given in Table 3.

3.5 Kinematic Fitting and Event Selection

In an ideal bubble chamber experiment, the probability distribution for the χ^2 of correctly selected kinematically fitted events is flat, and the Stretch functions for all track parameters are distributed as normal

Gaussians. Any deviations from this ideal represent the presence of systematic errors and/or badly estimated measurement errors.

Thus the dip Stretch function for a sample of τ decays of the beam track indicated that there was a systematic error in the dip which had opposite sign for the beam and outgoing tracks (Fig. 3.3a,b). The probability of χ^2 distribution for these τ's was sharply peaked at the lower end (Fig.3.3c) for the same reason. A possible explanation of this effect lay in incorrect geometrical reconstruction, and in particular in the constants used in the point to ray conversion formulae. The constants which corrected for curvature in the vertical plane were varied and the Stretch functions and probability plots were found to improve somewhat when they were decreased (Fig. 3.3,d,e,f). (It has since been shown that this curvature effect can be overcome by using point to ray conversion parameters which depend upon the depth of the track in the chamber.) The effect that this variation had on the important physical parameters such as effective masses and centre of mass angles was well within their errors, so that, as this was discovered late in the experiment, it was decided to ignore it. However, if 4C fits were taken down to a probability level of 1% it was estimated that 10% of true 4C type events would fail to fit above this level (compare the probability distribution in Fig.3.3c with that of Fig.3.7c). 1C fits have not been significantly affected as can be seen from the sample of Stretch function distributions in Fig. 3.5. Moreover, the half widths of these distributions are constitent with unity indicating that the errors are essentially correct.

The angular Stretch distributions for neutral tracks (i.e. those connecting a V^{o} to its production vertex) are a good test of vertex reconstruction, as the positions of the two vertices define the measured direction of the track. The appropriate distributions for this experiment (Fig. 3.6) are consistent with unit Gaussians indicating correct vertex reconstruction.

Even allowing for a small bias due to the above effect, the probability distributions for 1C fits has a large peak at the bottom end (Fig. 3.7a). This is caused by misfitting, particularly by fitting one missing π° hypotheses to events which really had two π°'s missing and $\Lambda\pi^{\circ}$type hypotheses to events which were really of the $\Sigma^{\circ}\pi^{\circ}$ type. That this is occurring can be seen from missing mass distributions, Fig.4.4 for example. It was, therefore, necessary to impose either limits on the missing mass or on the probability of the production vertex fit. Except for the above effects the probability distributions for the Imperial College rare events (Fig. 3.7) are flat.

Some further criteria besides goodness of kinematic fit were necessary in order to make the best assignment of events to hypotheses. Except for considerations specific to individual channels which will be dealt with later, the following were the criteria applied, and events selected on this basis were put onto a Data Summary Tape:-

(i) the bubble density calculated from the fitted parameters for all the tracks should agree with that observed;

(ii) 4C fits taken in preference to 1C fits;

(iii) single strange particle hypotheses taken in preference to triple strange particle hypotheses which in turn were taken in preference to quintuple strange particle hypotheses;

(iv) probability cutoff of 0.1% applied for all fits;

(v) charged K decay fits rejected in preference to hyperon decays if the length of the decaying track was less than 10 cm/Gev of fitted momentum.

The bubble density of a track was the one specific piece of physical information not available to the kinematics program. Fits were accepted or rejected on the grounds of bubble density by physicists examining all events and comparing the observed bubble density with that given by any fit. It was found possible to distinguish K from π mesons up to a momentum of 0.7 Gev and protons from mesons up to a momentum of 1.4 Gev.

Criteria (ii),(iii) and (v) are based on the idea of a difference in a priori probability(19) for producing a particular kind of event. Thus 4C fits were accepted in preferrence to 1C fits because the kinematic limits (within errors) of the former overlap a small region of those of the latter, whereas the kinematic limits (within errors) of the latter overlap a large proportion of those of the former. Hence, with this criterion we lose no genuine 4C events, while a few genuine 1C events are misidentified as 4C events. With the opposite criterion (i.e. 1C fits taken in preference to 4C fits) we would have no contamination in the 4C category, but a large proportion of genuine 4C would be misidentified as 1C, and it is this loss of 4C events which we wish to avoid.

The cross-section for single strange particle production is at least an order of magnitude larger than that for triple strange particle production. The cross-section for producing five strange particles is not known, but as few examples of events with four (or more) strange particle decays have been found it must be extremely small ($\lesssim 5\,\mu b$).

The a priori probability of a short decaying track being a K meson decay rather than a hyperon decay is small, since the decay length of a charged K meson is about 7 metres per Gev while that of a hyperon is a few centimetres/Gev. The decay length chosen as cutoff is arbitrary, but was sufficient to resolve all the ambiguities of this kind that occurred.

The probability of χ^2 cutoff was set low initially because it was easier to raise it if necessary than to re-select the events if the cutoff was thought to be too high. In practice, rather than alter this cutoff, limits were imposed on the missing mass and its error.

3.6 Particle Decays

A number of corrections are necessary to allow for loss of particle decays. These corrections divide into three classes:

(i) unseen neutral decays i.e. $\Lambda \rightarrow n + \pi^o$; $K^o \rightarrow \pi^o + \pi^o$

(ii) decay of Λ and K_1^o outside the chamber;

(iii) small angle decays of charged particles.

All appropriate cross-sections contain a factor of 3/2 to allow for the decay $\Lambda \rightarrow n + \pi^o$. The correction for events with a single K_1^o decay is 3. Events with a $K^o\,\bar{K}^o$ system are more complex as the $K^o\bar{K}^o$ system can be any mixture of the states $K_1^oK_1^o$, $K_1^oK_2^o$, $K_2^oK_2^o$. The fraction of these states which are observed as none, one or two K_1^o decays is given in the table below. (The branching ratios used for these corrections are

$\frac{\Lambda \rightarrow n\,\pi^0}{\Lambda \rightarrow p\,\pi^-} = \frac{1}{2}$, $\frac{K_1^o \rightarrow \pi^+\pi^-}{K_1^o \rightarrow \pi^o\pi^o} = 2$.)

State	No Decay Seen	One Decay Seen	Two Decays Seen
$K^o\bar{K}^o$	4/9	4/9	1/9
$K_1^oK_1^o$	1/9	4/9	4/9
$K_1^oK_2^o$	1/3	2/3	0
$K_2^oK_2^o$	1	0	0

The correction for the loss of Λ's and K^o's which decay too close to the production vertex or outside the chamber is done by calculating a weight W for each event:-

$$W = F / \{F.\exp(-lm/pct) - p\ [\exp(-(F + D)m/pct) - \exp(-Dm/pct)]\}$$

where F is the length of the region in which the production vertex can occur, D is any additional length in which a decay can occur, l is the minimum track length, m is the rest mass and t the proper lifetime of the decaying particle, p is its momentum and c is the velocity of light.

This expression was derived from the more usual one using potential lengths by integrating over the fiducial volume the probability of seeing an event. As an exact solution of the three dimensional problem is complex, the integration was performed along a single axis, the choice of axis being fixed for each event by determining which face of the fiducial box the particle would have passed through if it had not decayed. In practice, the majority of decaying tracks would have passed through the downstream end of the fiducial box used for rare events. Although nominally the production vertex is allowed to be anywhere within the fiducial region, the majority of events occur in quite a narrow region down the chamber because of the beam profile. This region was determined by plotting out the positions of all the production vertices, and the coordinates of its boundaries and those of the fiducial box used for rare events are given in the table below.

	Production Region	Fiducial Region (see Fig. 2.3)	D	F
X	55 to -55 cms.	55 to -55 cms.	0	110 cms.
Y	8 to -8 cms.	17.5 to -17.5 cms.	9.5 cms.	16 cms.
Z	22 to 26 cms.	5 to 40 cms.	16 cms.	4 cms.

This method avoids giving excessive weights to events at the extreme downstream end of the chamber. These are the events which are likely to be most poorly measured and identified.

No correction has been made for loss of $\Sigma^{\mp}$ decaying outside the chamber as this would be small, but a correction has been worked out to allow for the loss of small angle decays. These were estimated by examining the distributions of $\cos\theta$, θ being the Σ decay angle in its centre of mass, and φ, defined below, as functions of momentum (Fig. 3.8).

$$\varphi = \cos^{-1}\left\{\frac{(P_\Sigma \wedge P_\pi)\cdot(P_\Sigma \wedge Z)}{|P_\Sigma \wedge P_\pi|\ |P_\Sigma \wedge Z|}\right\}$$

which is the azimuthal angle of the Σ decay. A comparison of these distributions for the three decays $\Sigma^{\pm} \rightarrow n + \pi^{\pm}$ and $\Sigma^{+} \rightarrow p + \pi^{0}$ indicated that the proton decay mode of the Σ^{+} was so badly biased that any attempt at correction was useless, while the losses in the $\Sigma^{\pm} \rightarrow n + \pi^{\pm}$ decays were similar, making it possible to combine the data for the two. Assuming that no events were lost for the intervals $\varphi > 0.3\frac{\pi}{2}$ for all

Σ momenta, and $-0.8 < \cos\theta < 0.6$ for $P_\Sigma < 1.2$ Gev, $-0.8 < \cos\theta < 0.4$ for $1.2 < P_\Sigma < 3.6$ Gev and $-0.8 < \cos\theta < 0.$ for $P_\Sigma > 3.6$ Gev, the expected total number of events in each momentum interval was calculated. A weight given by the expected number divided by the observed number of events was then calculated, and parameterised by $W = 1 + (0.13 \pm 0.03) P_\Sigma$ (Fig. 3.4). This expression was incorporated into the statistics program together with a factor exp(ml/Pct) which corrects for the loss of short Σ tracks.

Applying the same principle to all Ξ^- decays in which the Λ was seen gives a correction factor of 1.07 ± 0.1. There were too few events to investigate the momentum dependence of any loss.

3.7 Beam Contamination

The π/K ratio of the beam was determined in several ways. Measurements made by absorbing the beam in lead, by counting the number of interactions with the beam tuned to the 'mirror point' and by calculation from the Čerenkov and scintillation counters gave a π/K ratio of $15 \pm 5\%$ for run D and the first half of run E and $2 \pm 2\%$ for the second half of run E and all run F(20). The Munich group obtained a value of $6 \pm 3\%$ for runs E and F by fitting the number of interactions to the Čerenkov and scintillation counters readings(21). A further estimate of the π/K ratio is given in the next section.

3.8 Calculation of Cross-sections

The cross-section for a process is conveniently given by

$$\sigma(\text{microbarns}) = n\mu$$

where n is the number of events corresponding to the process and μ is the microbarn equivalent (μb/event). μ is calculated from the observed number of τ decays of the beam track by

$$\mu = 10^{30} mf/A\rho Npct \ \mu b/\text{event}$$

where m is the K^- mass in Gev (0.4938)

f is the branching ratio of K^- to three charged particles (5.8 ± 0.2%)

A is Avogardro's number (6.02×10^{23})

ρ is the density of liquid hydrogen (0.061 ± 0.001 gm/cm^3)

N is the number of τ decays corrected for scanning loss

p is the beam momentum (6.02 ± 0.06 Gev)

c is the velocity of light (3.00×10^{10} cm/sec)

and t is the K lifetime (1.229×10^{-8} sec).

This becomes $\mu = (2110 \pm 90)/pN$ μb/event.

At Imperial College the number of τ decays observed in region A was 421 with a calculated efficiency of 91%, so

$$\mu = 0.758 \pm 0.05 \ \mu b/\text{event}.$$

It is also possible to estimate μ from the total number of events observed, the pion contamination and the Kp and πp total cross-sections. However, it is useful to reverse the calculation and to use the value of μ obtained above to give a further estimate of the pion contamination in the beam. Thus the ratio of pions to kaons in the beam is given by

$$\frac{\mu N_T - \sigma_K}{\sigma_\pi}$$

where N_T is the total number of events observed and σ_K and σ_π are the total K^-p and π^-p cross-sections respectively.

After correcting for the loss of low momentum transfer elastic scatter events, N_T for Imperial College data is 33,900 ± 1000. Using $\sigma_K = 24.0 \pm 0.3$ mb and $\sigma_\pi = 28.5 \pm 0.3$ mb(22), the pion contamination is calculated as 6 ± 6%. This is a useful confirmation of the previous estimates.

The calculation of many of the cross-sections presented in this thesis was complicated by the fact that not all the data was available from all the collaborating groups. The differences in the quantity of data available for different final states is reflected in their errors and in the fact that histograms of events from different topologies can not always be directly compared.

To compute the cross-section and its error for a particular process the number of events contributing to this process must be calculated. This is obtained from the observed number of events by multiplying by the correction factors required to compensate for

(a) the loss of events in data analysis because of poor film, computing and book-keeping errors,

(b) the branching ratio of V^o's to neutral particles,

(c) the loss of particles decaying outside the chamber or at small angles.

We have already dealt with points (b) and (c). The losses in (a) arise partly from human error and partly because some events are unmeasurable as they are obscured by other tracks, or the film was damaged in some way. For Imperial College this correction factor is

1.25 ± 0.06 (see footnote to Table 3) and for other groups it is about 1.34 (these numbers refer to rare events only). A breakdown of what happened to Imperial College rare events is given in Table 3.

The number of events observed was also corrected for those events which are ambiguous between two or more hypotheses. In general, if an event was ambiguous between m hypotheses it was assigned to each hypothesis with weight 1/m. The error in the total number of events, N_T, assigned to an hypothesis is then

$$\surd[\, N_T + \sum_i \frac{1}{m_i}\left(1 - \frac{1}{m_i}\right)]$$

where $N_T = N_{unique} + \sum_i \frac{1}{m_i}$, the summation being over the ambiguous events, each with ambiguity m_i.

The error on the correction factor (a), on the microbarn equivalent, and the statistical error on the observed number of events, were added in quadrature to give the error on the cross-section.

TABLE 3

	Numbers of Events				
Topology	Scanned	Unmeasurable	Failed to pass Analysis System	Successful in passing Analysis System	Total After Analysis
002	96	7	7	60	74
003	15	1	1	9	11
202	225	26	17	84	127
203	15	1	2	8	11
$21^{-}1$	126	12	10	62	84
$41^{-}1$	137	13	11	77	101
$21^{+}1$	80	11	3	42	56
$41^{+}1$	71	10	6	16	32
$61^{-}1$	14	1	2	4	7
Others	170	13	13	65	91
TOTALS	949	95	72	427	594

Footnote:- The total number of events after data analysis is less than that scanned because many events were misclassified by the scanners. The events that did not pass through the data analysis system will contain some that are misclassed, and this was allowed for when the correction factor required to determine cross-sections was calculated. If T1,2,..5 are the numbers in columns 1,2,..5 of the TOTALS row, then instead of calculating the correction factor as T5/T4, the following expression was used:-

$$\frac{T4 + T5(T2 + T3)/T1}{T4}$$

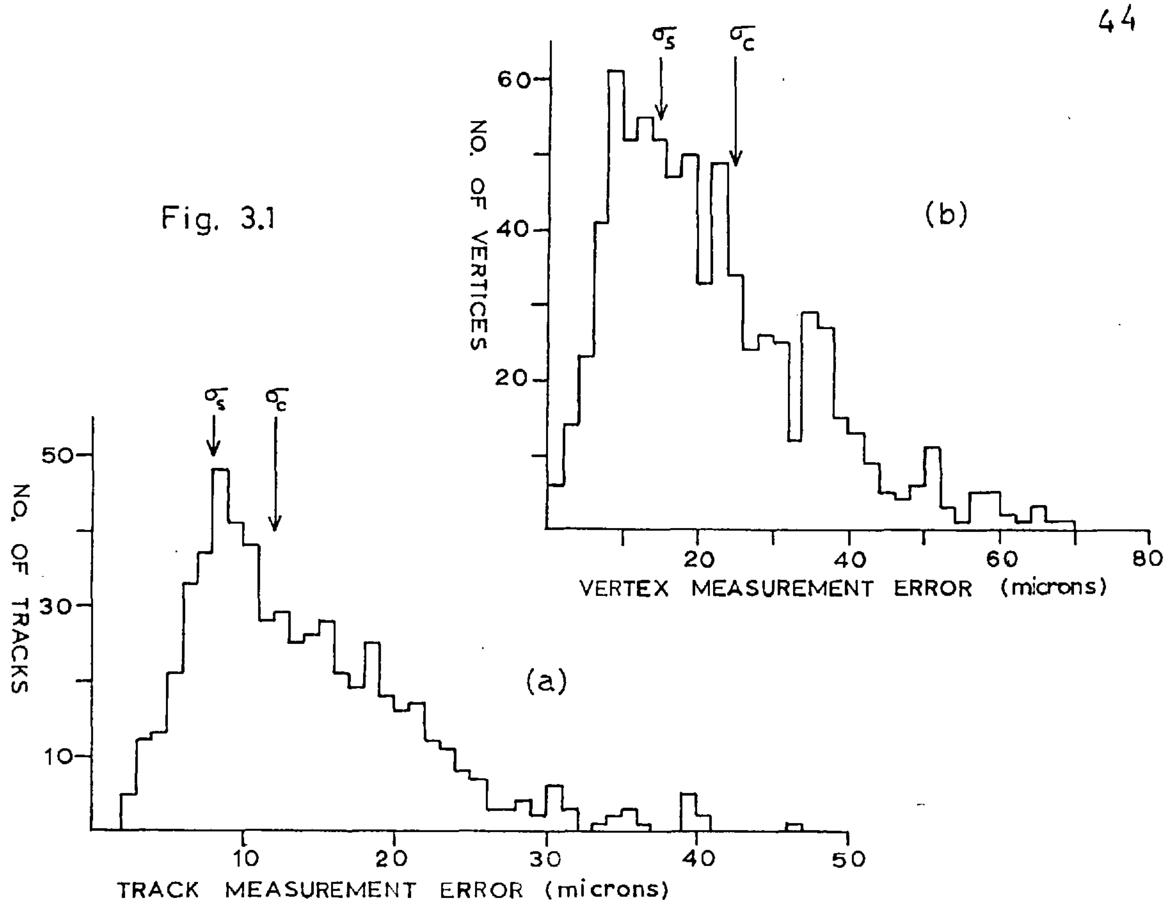

Fig. 3.1

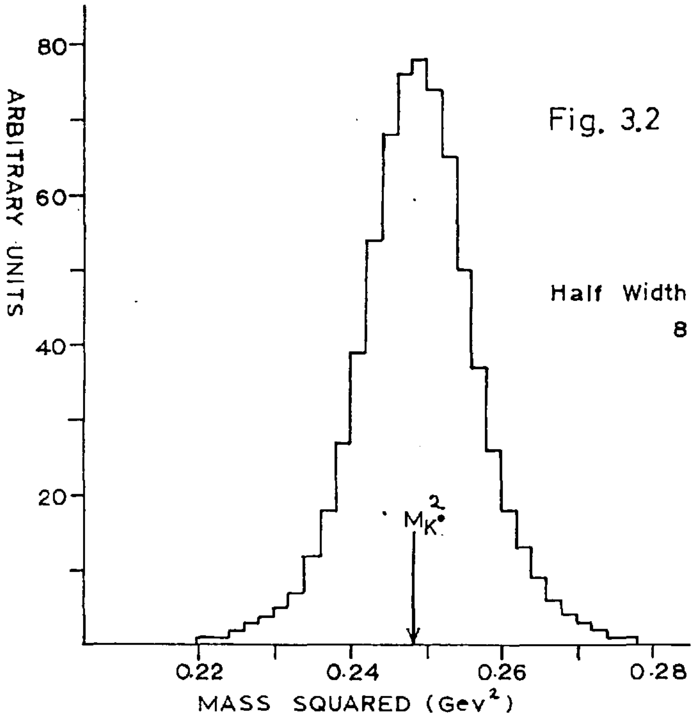

Fig. 3.2

Half Width at Half Height
8 Mev

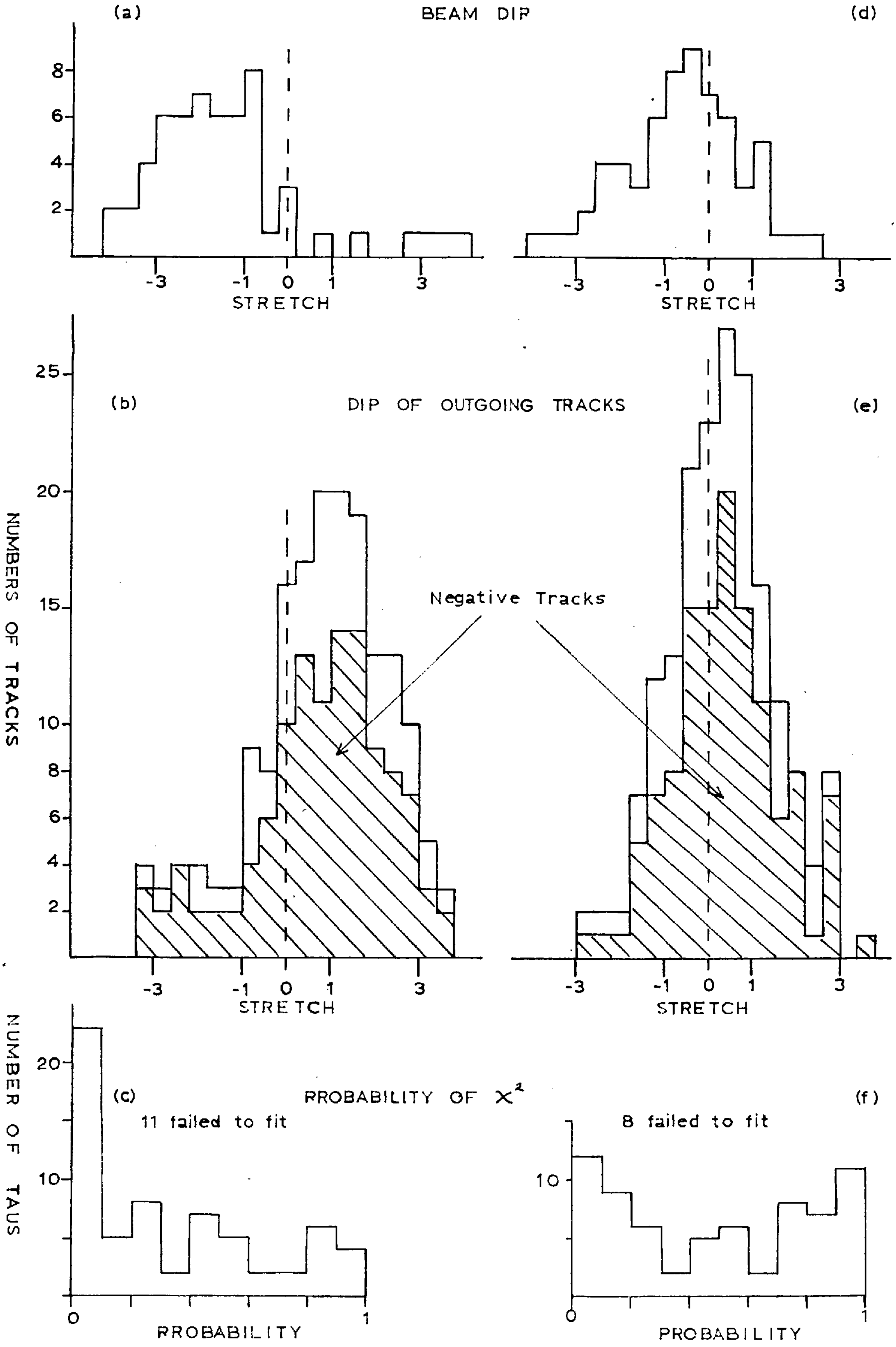
(a)
BEAM DIP
(d)
8
6
4
2
-3
-1
0
1
3
STRETCH
25
20
15
10
8
6
4
2
(b)
DIP OF OUTGOING TRACKS
(e)
NUMBERS OF TRACKS
Negative Tracks
STRETCH
NUMBER OF TAUS
20
10
(c)
PROBABILITY OF χ^2
(f)
11 failed to fit
8 failed to fit
0
1
PROBABILITY

Fig. 3.3

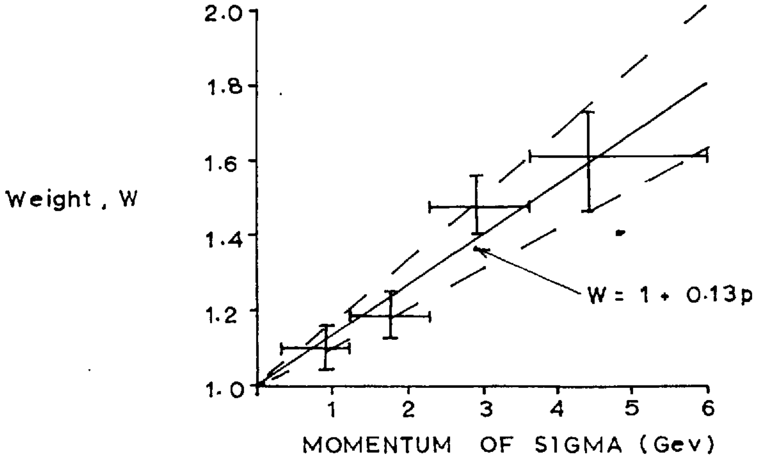

Fig. 3.4

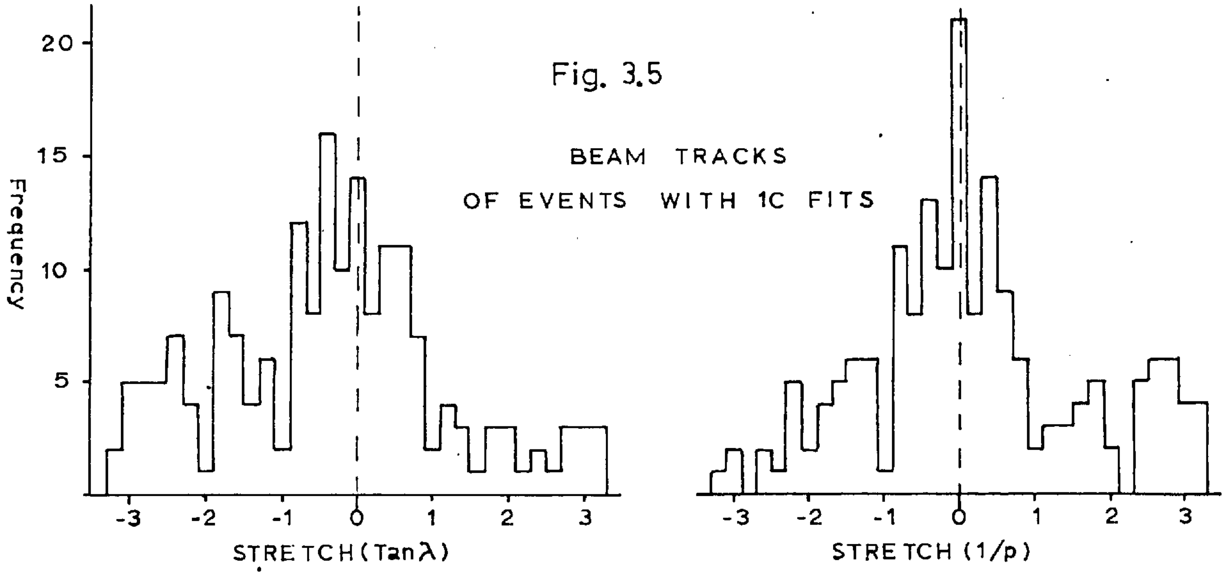

Fig. 3.5

BEAM TRACKS
OF EVENTS WITH 1C FITS

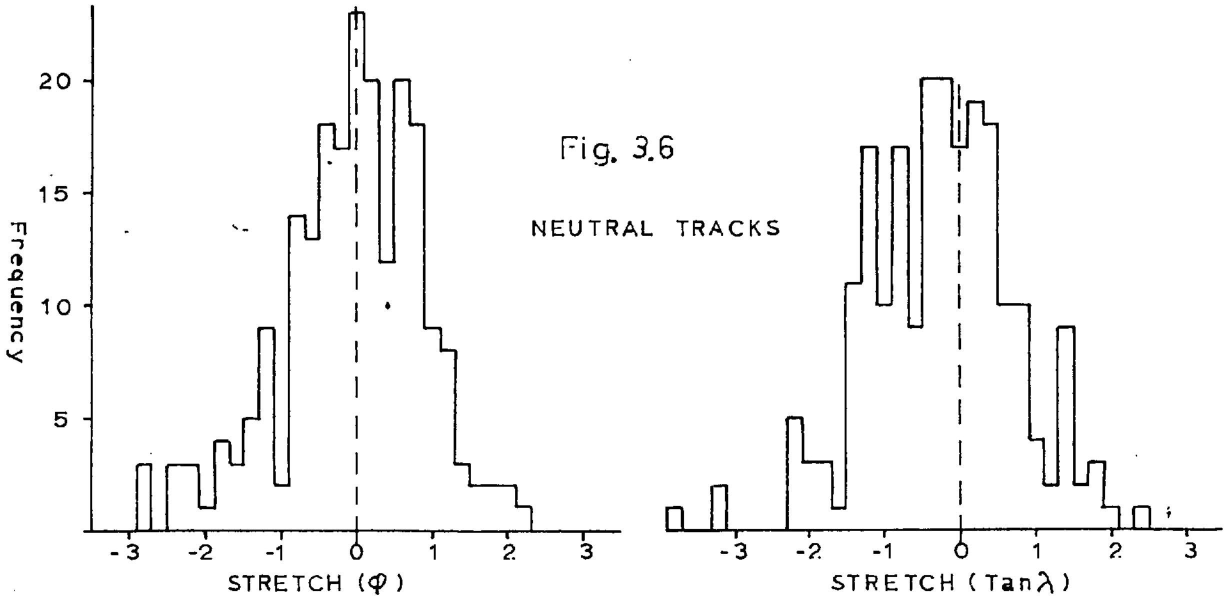

Fig. 3.6

NEUTRAL TRACKS

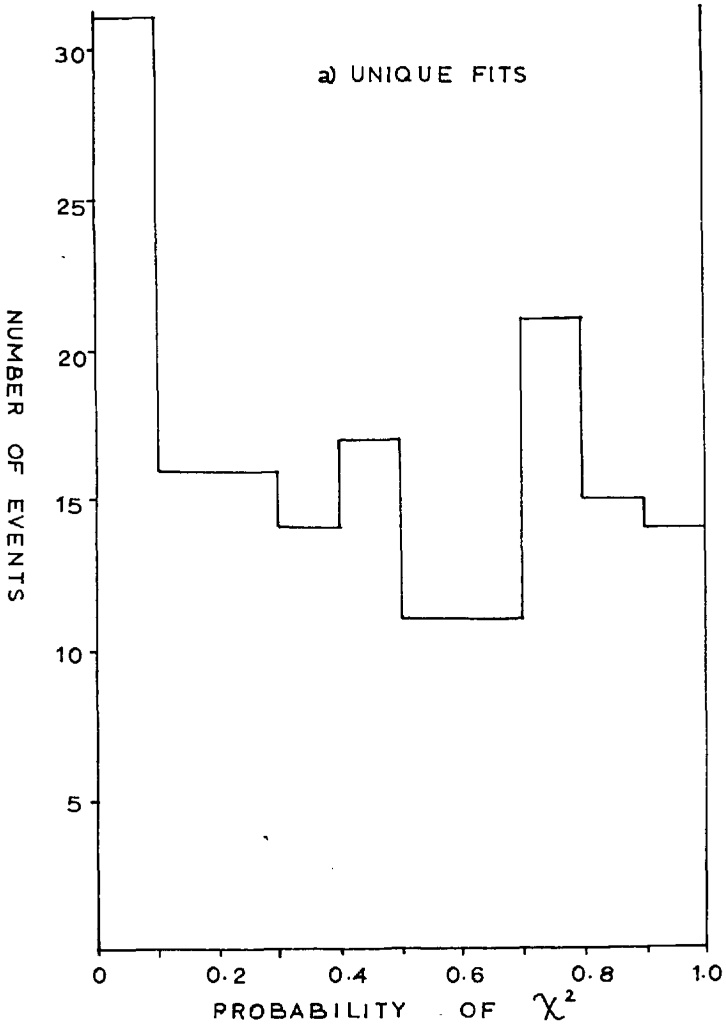

Fig. 3.7

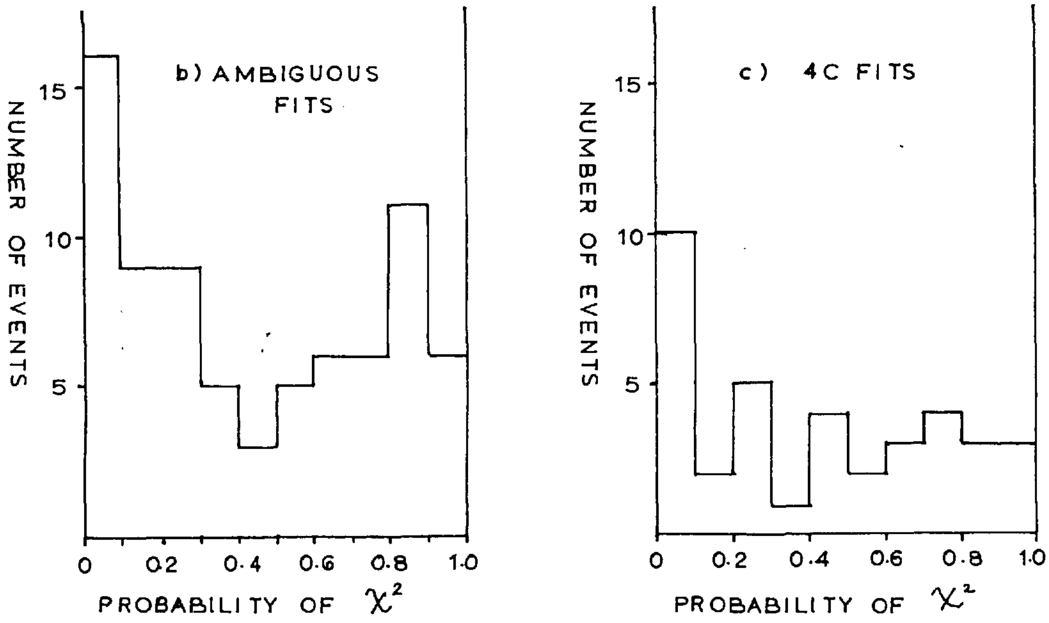

PRODUCTION FIT PROBABILITY DISTRIBUTIONS FOR I.C. RARE EVENTS

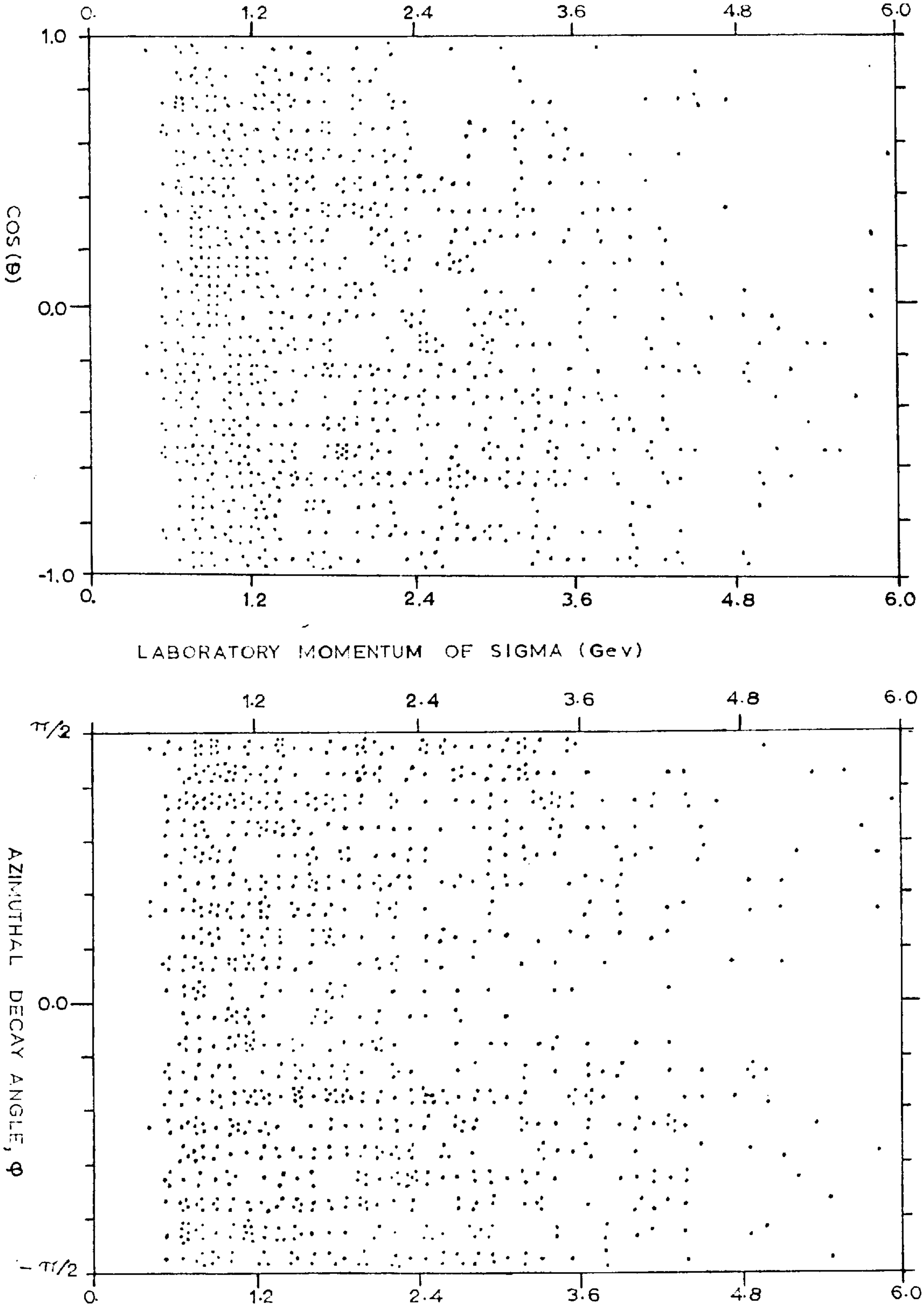
0.
1.2
2.4
3.6
4.8
6.0
1.0
0.0
-1.0
COS (θ)
0.
1.2
2.4
3.6
4.8
6.0
LABORATORY MOMENTUM OF SIGMA (Gev)
1.2
2.4
3.6
4.8
6.0
π/2
0.0
−π/2
AZIMUTHAL DECAY ANGLE, Φ
0.
1.2
2.4
3.6
4.8
6.0

Fig. 3.8

CHAPTER FOUR

$YK\bar{K}$ PRODUCTION

A number of final states containing $YK\bar{K}$ were produced with sufficiently large a cross-section to allow some analysis of resonance production. Unfortunately, the number of events in any single channel was so small that the results presented here can only be a guide to what occurs in these interactions. In a few specific cases the data is such that a quantitative analysis seems useful.

In any final state involving a Λ there exists the possibility that it arose from the decay $\Sigma^0 \rightarrow \Lambda + \gamma$. As the Q-value for this decay is small, corresponding Λ and Σ^0 hypotheses are frequently kinematically ambiguous to such an extent that separation of the two can only be achieved in part by an examination of missing mass and momentum distributions. Such a separation was not possible with the statistics available for the final states discussed here, so that Σ^0 contamination is largely unknown.

We examine each of the final states $\Lambda K\bar{K}$, $\Lambda K\bar{K}\pi$, $\Lambda K\bar{K}\pi\pi$, $\Sigma^{\pm}\pi^{\mp}K\bar{K}$, and $\Sigma^- K^+ \bar{K}^0$, which were all produced relatively strongly. All cross-sections mentioned in the text are tabulated in Table 4 at the end of the chapter. In addition, this table contains some cross-sections for those final states in which the number of events produced was so small as to preclude further analysis. Discussion of the results in the context of other experiments and theory is left to chapter 6.

4.1 The $\Lambda K\bar{K}$ Final States

These final states were observed both as $\Lambda K^o\bar{K}^o$ and ΛK^+K^-. Σ^o contamination in the latter case seems to be small as none of the Imperial College events which fitted ΛK^+K^- also fitted $\Sigma^o K^+K^-$(with probability >1%). A plot (Fig. 4.1) of missing mass against its error for events in which a Λ and K_1^o were seen shows that the peak corresponding to a missing K^o has an asymmetry of about one standard deviation, indicating the possible presence of Σ^o contamination. At lower energies (e.g. 3.5 Gev, Reference 8) $\sigma(\Sigma^o\varphi) \doteqdot \frac{1}{2}\sigma(\Lambda\varphi)$ and at 5 Gev, Barnes et al.(23) estimate a Σ^o contamination of about 10% in their $\Lambda K^o(K^o)$ final state. It would therefore appear that Σ^o contamination is unimportant in this channel.

The Dalitz plot and $K\bar{K}$ mass spectrum (Figs. 4.4, 4.6) show a strong φ and possibly some f' production. As expected the φ contains no $K_1^oK_1^o$ events (because its C-parity is negative), these contributing mainly to the f' region, indicating positive C-parity. There is no evidence for any resonance in either ΛK or $\Lambda\bar{K}$ states (Fig 4.5).

Taking the φ as those states having a $K\bar{K}$ effective mass in the range 1.0 to 1.04 Gev (this effective mass range is used throughout this thesis when the φ is specified) we find that it is all produced at low t (Fig. 4.7), there being no event in the backward hemisphere. The spin density matrix elements calculated from the Smith I and Treiman-Yang angle decay distributions (Fig. 4.9) are

$$\rho_{11} = 0.45 \pm 0.07 \; ; \quad \rho_{1-1} = 0.39 \pm 0.13 \; ; \quad \mathrm{Re}\rho_{10} = -0.07 \pm 0.08,$$

and the Λ polarisation is given by

$$\alpha P_\Lambda = (3/N)\sum_i \mathrm{Cos}\,\theta_i = 0.28 \pm 0.26$$

where θ_i is the polarisation angle and N is the total number of events (Fig. 4.8).

The total cross-section for $\Lambda\varphi(\varphi \rightarrow K\bar{K})$ is 11 ± 2 μb.

A useful parameterisation for the t distribution of 2-body processes (see Reference 24 and chapter 6 for the reasons for this) is

$$\frac{d\sigma}{dt} \propto \exp\ (-At)$$

The data here is inadequate to provide a good test of this form, but if we assume it, (and the data is certainly compatible with it), we can determine the value of A from the maximum likelihood estimate

$$\frac{1}{A} = \bar{t} - t_{min}$$

where $\bar{t}$ and t_{min} are the mean and minimum values of t respectively. The t distribution for $\Lambda\varphi$ in this case gives $A = 2.67 \pm 0.53$ Gev^{-2}. The production angular distribution for ω in $\Lambda\omega$ is also shown for comparison with that of the φ (Fig. 4.10).

Since its statistical significance is so small, we can only quote a cross-section for $\Lambda f'$ production, which is 2.2 ± 0.9 μb. f' production is considered again at the end of this chapter when a value for its branching ratio $f' \rightarrow K^+K^- \ /\ f' \rightarrow K_1^oK_1^o$ is derived.

4.2 The $\Lambda K\bar{K}\pi$ Final States

The final states which were observed are $\Lambda K_1^oK_1^o\pi^o$, $\Lambda K^+K^-\pi^o$, $\Lambda K_1^oK^+\pi^-$ and $\Lambda K_1^o\pi^+K^-$. The first was well identified while the identification of the other three was somewhat problematical. The $\Lambda K^+K^-\pi^o$ events were extracted from all events with topology 201 by taking kinematic fits with a probability greater than 1% which were consistent with bubble density, and then applying a 2.5 standard deviation cut as well as cuts at -0.04 Gev^2 and 0.08 Gev^2 on the missing mass squared. In addition the missing momentum was required to be greater than 100 Mev to eliminate possible mis-fitting of ΛK^+K^- and $\Sigma^o K^+K^-$. These cuts were arrived at after careful examination of both fitted and unfitted data. It was estimated from comparison of the missing mass squared spectrum of $\Lambda K^+K^-\pi^o$ with that for $\Lambda\pi^+\pi^-\pi^o$ (Fig. 4.11) that the cuts used gave a loss of about 30% of true $\Lambda K^+K^-\pi^o$ while passing a background of mis-fits of about the same figure. This background should be fairly smoothly distributed in the mass distributions unless a strong sharp resonance was being produced in another final state which was mis-fitting to $\Lambda K^+K^-\pi^o$. There should, therefore, be no serious effect on well known resonances such as the φ except for a slight increase in background.

The φ is produced quite strongly in this final state (Fig. 4.12), the cross-section for $\Lambda\varphi\pi^o$ being $9 \pm 3\,\mu$b, no significant portion of this being $Y^{*o}(1385)\varphi$.

The production angular distributions of the Λ, φ and π^o (Fig. 4.15) indicate that the Λ and φ are produced peripherally i.e. at small production angles and small t, while the π^o is not. We might therefore consider this channel as a candidate for a double peripheral graph after the manner of Joseph and Pilkuhn(26) (Fig. 4.16). We look at the scattering angles between the K^- and φ in the $\varphi\pi^o$ centre of mass and the p and Λ in the $\Lambda\pi^o$ centre of mass (Fig. 4.15) for events in which

$\cos\theta^*_\Lambda < -0.6$ and $\cos\theta^*_\varphi > 0.6$ (this corresponds in practice to a t cut at 2 Gev^2); these distributions should be symmetric about zero if either $\varphi\pi^\circ$ or $\Lambda\pi^\circ$ resonant states are formed or if the particles are produced according to Lorentz invariant phase space. If a double peripheral model is applicable then these distributions should look like the production angular distributions of low energy two-body production processes i.e. something like $K^-(K^+$ or $K^{*+}) \rightarrow \varphi\pi^\circ$ and $(K^-$ or $K^{*-})p \rightarrow \Lambda\pi^\circ$. This is, of course, a rather naive picture, as the K or K^* exchange particles are "off their mass-shell" and there are numerous difficulties with even the simple peripheral model where both incoming particles are physical. The present data does show a slight peripheral-like peaking, though even taking the two distributions together, they are asymmetric by only two standard deviations.

There is a second peak in the K^+K^- effective mass distribution (Fig. 4.12) at ~1.2 Gev in which the K^+K^- are as peripheral as the φ. As this does not occur elsewhere, nor does it correspond to a known resonance, it must be presumed to be the result of mis-fitting rather than a previously unobserved resonance. In particular, it could occur as the result of mis-fitting $\Lambda K^+\pi^-(\bar{K}^0)$ events in which K^{*0} is strongly produced. (Mis-identifying the π^- as a K^- will certainly give a mass of about 1.23 Gev for K^+K^- if the genuine $K^+\pi^-$ mass was 0.89 Gev.) This possibility is supported by the observations of the following paragraphs.

Another feature of this final state is the production of $K^{*+}(890)$ (Fig. 4.13). To the author's knowledge a positive strangeness K^* has not been previously observed in K^-p interactions, except in conjunction with a Ξ or Ξ^*, or as the decay product of a non-strange meson (e.g. D,E or f'). The $K^-\Lambda$ effective mass distribution for the K^{*+} events (taken as those events with 0.84 Gev $< M(K^+\pi^0) <$ 0.94 Gev, Fig. 4.18) does not show any evidence for Ξ^* production, nor does the $K^{*+}K^-$ effective mass (Fig. 4.20) show any significant structure. The known resonances are indicated on these plots purely for reference.

In the spirit of the double peripheral model, a diagram such as that in Fig. 4.17 might be a useful way of examining this channel. If this is the case, then we might also expect to see the channel $\Lambda K^{*0}\bar{K}^0$ as ρ^0 or ρ^- exchange could mediate between the top two vertices. Indeed, the $K\pi$ mass plot for the final states $\Lambda K_1^0 K_1^0 \pi^0$ and $\Lambda K_1^0 \pi^- K^+$ (Fig. 4.14) does show a K^* peak. Moreover the numbers of events in these two final states and in $\Lambda K^+ K^- \pi^0$ and $\Lambda K^0 \pi^+ K^-$ are compatible with the known branching ratios of the K^*. We feel justified in combining the data from all four $\Lambda K\bar{K}\pi$ final states to look at the channel $\Lambda K^*\bar{K}$, but in practice, because the K^0 can not be distinguished from the $\bar{K}^0$, $\Lambda K_1^0 K_1^0 \pi^0$ events have not been used.

Fig. 4.13 shows the combined $K\pi$ mass plot while Fig. 4.19 shows the production angles of the $\bar{K}$, $K\pi$ and Λ plotted against $K\pi$ effective mass. This method of display gives an easy comparison between resonant and non-resonant events. In the K^* region the Λ is peaked strongly backwards in the centre of mass while the $\bar{K}$ and K^* are peaked forward, the $\bar{K}$ perhaps more so than the K^*. In analogy with $\Lambda\varphi\pi^0$ we look at the scattering angles between the incoming and outgoing $\bar{K}$ and between the Λ and p (Fig. 4.19). These show a significant peaking, indicating a peripheral interaction between each pair of particles, though in the case of the $\bar{K}K^*$ it is not very strong.

The cross-sections for $\Lambda K^{*+}K^-$ and $\Lambda K^{*0}\bar{K}^0$ are 14 ± 4 μb and 14 ± 6 μb respectively.

If a non-strange resonance decayed to $\bar{K}K^*$ we would expect that the amounts of K^-K^{*+} and $\bar{K}^0K^{*0}$ to be the same (because both K and K* have I-spin ½) as observed, and we would also expect to see the same amount of $K\bar{K}^*$. No $\bar{K}^*$ is seen however, and this is qualitatively consistent with the double peripheral model for the following reason. Chan Hong-Mo et al.(27) have shown that, other things being equal, diagrams with a heavy particle coming from the centre vertex are kinematically favoured over those with a light particle coming from this vertex. Hence, the channel $\Lambda K^*\bar{K}$ is kinematically favoured over $\Lambda\bar{K}^*K$ because a K* must be produced at the centre vertex (if we neglect baryon and double strangeness exchange) whereas a $\bar{K}^*$ must be produced at the top vertex.

4.3 The $\Lambda K\bar{K}\pi\pi$ Final States

The total cross-section for these final states is quite high, being 112 ± 12 μb, in strong contrast to the corresponding cross-section of < 3 μb at 3.5 Gev(8). When seen as $\Lambda K^0\bar{K}^0\pi^+\pi^-$ and $\Lambda K^+K^-\pi^+\pi^-$ the contamination was small, but the hypotheses $\Lambda\bar{K}^0K^+\pi^-\pi^0$ and $\Lambda K^0K^-\pi^+\pi^0$ were generally kinematically ambiguous with one another. Permutation of the K's and π's lead to some ambiguities in $\Lambda K^+K^-\pi^+\pi^-$. If only one permutation gave a φ, then this was taken as the 'correct' fit, if neither or both gave φ's, then both permutations were used, each with weight of one half. (In all, this affected only 7 events, 2 of which gave a φ.)

The $K\bar{K}$ mass spectrum from the first two final states (Fig. 4.21) shows strong φ production ($\sigma(\Lambda\varphi\pi^+\pi^-) = 11 \pm 3\,\mu b$) with no sign of associated Y^* production or any structure in the $\pi^+\pi^-$ effective mass; the φ decay distributions (Fig. 4.30) correspond to density matrix elements

$$\rho_{11} = 0.36 \pm 0.07 \qquad \rho_{1\,-1} = -0.01 \pm 0.1 \qquad \mathrm{Re}\,\rho_{10} = -0.02 \pm 0.08.$$

The production angular distributions (Fig. 4.23) of the Λ and φ show strong peripheral peaking, whereas the two pions have this characteristic to a much less marked extent. The scattering angles (Fig. 4.23) for $\varphi\pi^+$ and $\varphi\pi^-$, both strongly asymmetric, indicate that the φ and π's are not produced at the same vertex. In contrast, the scattering angles for $\Lambda\pi^+$ and $\Lambda\pi^-$ are essentially flat indicating that these three particles may be produced at the same vertex either through a resonance or according to phase space. The effective mass plots (not shown) for $\Lambda\pi^+$, $\Lambda\pi^-$ and $\Lambda\pi^+\pi^-$ show no evidence of resonance production.

The only other significant features in $\Lambda K^0\bar{K}^0\pi^+\pi^-$ is some evidence for a K^{*+} and a sharp peak in the $K^0\pi^+\pi^-$ effective mass distribution (not shown). However, we would expect 12 $\Lambda\bar{K}^0K^+\pi^-\pi^0$ for the 11 $\Lambda K^0\bar{K}^0\pi^+\pi^-$ from the channel $\Lambda\bar{K}^0K^{*+}\pi^-$, but the $K^+\pi^0$ mass plot from $\Lambda\bar{K}^0K^+\pi^-\pi^0$ gives only about 6 events at most in the K^* region. The K^* peak in $\Lambda K^0\bar{K}^0\pi^+\pi^-$ therefore seems spuriously large. Likewise, no explanation other than a statistical fluctuation can be found for the $K^0\pi^+\pi^-$ peak; it happens to be at the peak of phase space, has no counterpart elsewhere and corresponds to no known resonance.

4.4 $\Sigma^{\pm}\pi^{\mp}K\bar{K}$ Final States

When these final states were seen as $\Sigma^{\pm}\pi^{\mp}K^{+}K^{-}$, any permutation ambiguities were dealt with in the same way as for $\Lambda\pi^{+}\pi^{-}K^{+}K^{-}$; $\Sigma^{\pm}\pi^{\mp}K^{o}\bar{K}^{o}$ events seem well identified. Although the loss of Σ^{+} decaying to $p + \pi^{o}$ was serious, the effective mass spectra and angular distributions for these were not significantly different from those for events in which $\Sigma^{+} \rightarrow n + \pi^{+}$. Accordingly, $\Sigma^{+} \rightarrow p + \pi^{o}$ events have been used in all histograms, but the cross-sections for Σ^{+} events have been calculated from $\Sigma^{+} \rightarrow n + \pi^{+}$ events and doubled to allow for the proton decay mode.

These final states are again dominated by φ production, but in contrast to the Λ channels which show no $Y^{*}(1385)$ there is also relatively strong Y_{o}^{*} (1405) and Y_{o}^{*} (1520) formation (Figs. 4.22 and 4.24). The final states $\Sigma^{+}\pi^{-}\varphi$ and $\Sigma^{-}\pi^{+}\varphi$ are remarkly similar so the data has been combined.

The $\Sigma\pi$ effective mass for $\Sigma\pi\varphi$ events (Fig. 4.25) shows little Y_{o}^{*} formation, no more than might be expected from an incoherent overlap of Y_{o}^{*} and φ events. No attempt has therefore been made to select out $Y_{o}^{*}\varphi$ events in looking at the channel $\Sigma\pi\varphi$. The Treiman-Yang and Smith I distributions for the φ (Fig. 4.27) give density matrix elements

$$\rho_{11} = 0.43 \pm 0.12 \quad \rho_{1\,-1} = 0.17 \pm 0.09 \quad \mathrm{Re}\,\rho_{10} = -0.04 \pm 0.08$$

indicating that if the φ is produced by a peripheral process it is by a mixture of vector and pseudoscalar exchange. The φ production angular distribution (Fig. 4.27) is of the peripheral type and the $\varphi\pi$ scattering angles (Fig. 4.28) are also peripherally peaked. The φ would therefore again seem to be produced on its own at a separate vertex. Both the Σ^{+} and Σ^{-} are peaked backwards in the overall centre of mass, the Σ^{+} more so than the Σ^- (Fig. 4.27), while the pions are much less peaked. The $\Sigma\pi$ scattering angles (Fig. 4.28) are consistent with being flat, so the Σ and π are presumably produced at the same vertex. This would explain the similarity between Σ^+ and Σ^- channels.

A double peripheral mechanism would be expected to show a distinct difference between the channels because the charges of the Σ and π make it impossible to draw the same diagrams for both Σ^+ and Σ^- (if we neglect the possibility of double charge exchange). The Σ^+ must be produced at the bottom vertex by meson exchange, whereas the Σ^- must be produced at the centre vertex by baryon exchange.

As no difference between the channels is seen, we conclude that the $\Sigma\pi\varphi$ production mechanism is dominated by a single peripheral diagram.

Both Y_0^* (1405) and Y_0^* (1520) are peaked strongly backwards in the centre of mass (Fig. 4.26). The $K^0\bar{K}^0$ scattering angles do not give much information because the K^0 can not be distinguished from the $\bar{K}^0$. There was little Y_0^* production in $\Sigma^{\pm}\pi^{\mp}K^+K^-$ and these would be very susceptible to mis-fitted $\Sigma^{\pm}\pi^{\mp}\pi^+\pi^-$ events.

4.5 $\Sigma^-K^+\bar{K}^0$ Final State

The production mechanism for this final state appears to be different from that for $\Sigma^-\pi^+\varphi$ as is shown by the angular distributions. The K^+ is peaked sharply backwards while the Σ^- and $\bar{K}^0$ are peaked forward in the centre of mass (Fig. 4.29). The K^+peak is similar to that in Ξ^-K^+ (see the next chapter), so the possibility of a $\Sigma^-\bar{K}^0$ resonance (i.e. a Ξ^{*-} decaying to $\Sigma^-\bar{K}^0$) presents itself. However, the $\Sigma^-\bar{K}^0$

effective mass plot, with only 10 events, shows no significant structure.

4.6 The f' (1500) Meson

As the f' has been seen in only two previous experiments(23, 28) a careful examination of the data for possible f' production is useful even though the statistical significance of the present data is poor.

The previous observations of the f' as a $K_1^oK_1^o$ resonance have shown that it is a C = P = +1 resonance with a possible spin of 2. The J^P assignment 2^+ is strongly favoured on theoretical grounds as it would then allow the f' to be classified as the isosinglet member of a 2^+ SU(3) octet which can mix with f(1250). No experimental estimate has been made of its branching ratio to K^+K^-, while its decay into $K\bar{K}^*$ or $\bar{K}K^*$ has been shown to have a small branching ratio (29).

To obtain a reasonable number of events we have combined the $K^o\bar{K}^o$ effective mass plots from $\Lambda K^o\bar{K}^o$, $\Lambda K^o\bar{K}^o\pi^+\pi^-$, and $\Sigma^\pm\pi^\mp K^o\bar{K}^o$ (Fig. 4.31). This plot has a peak of rather more than three standard deviations in the mass range 1.49 to 1.59 Gev, to which events with two seen K_1^o's make a significant contribution. If we assume that the events in the above mass region come from a $K^o\bar{K}^o$ phase space background plus a $K_1^oK_1^o$ state, then we can calculate the relative proportions of the two contributions from the observed number of events;

$$a = 3(N_2 - N_1/4) \; ; \qquad b = 3(N_1 - N_2)$$

where N_1 is the number of events observed with one seen K_1^o, N_2 is the number of events observed with two seen K_1^o's and a is the actual number of $K_1^oK_1^o$ events and b is the actual number of $K^o\bar{K}^o$ events produced. In doing this we neglect any loss of K_1^0's which decay to $\pi^+\pi^-$ outside the chamber as this effect should be small. (The error introduced by neglecting this will certainly be much smaller than the statistical error.) This calculation gives the total number of f' events as 15 and the total number of background events as 30; of these, 7 f' events have two observed K_1^0 decays and 7 have only one observed K_1^0 decay. The estimate of resonant and non-resonant contributions calculated by this method agrees well with that given by drawing a smooth curve through the background events and counting the number of events above this line (Fig. 4.31).

If K^0's obey Bose statistics, a resonant state decaying to $K_1^0K_1^0$ must have even parity and angular momentum and should decay to K^+K^- with a branching ratio $f' \rightarrow K^+K^- / f' \rightarrow K_1^0K_1^0$ of about two. To determine this branching ratio experimentally we have plotted the K^+K^- effective mass from ΛK^+K^-, $\Lambda K^+K^-\pi^+\pi^-$ and $\Sigma^\pm\pi^\mp K^+K^-$ (Fig. 4.31); there is a slight enhancement in the f' region. Unfortunately, as the data for the two mass plots do not come from exactly the same sample of events, the height of the two f' peaks can not be directly compared. We can, however, calculate the total cross-section for f' production in the three final states $\Lambda f'$, $\Lambda f'\pi^+\pi^-$ and $\Sigma^\pm\pi^\mp f'$, from the K^+K^- and $K_1^0K_1^0$ modes separately. Their ratio then gives the f' branching ratio. By this method we obtain $\sigma(f' \rightarrow K^+K^-) = 5.6 \pm 1.8\ \mu b$ and $\sigma(f' \rightarrow K_1^0K_1^0) = 5.5 \pm 1.4\ \mu b$ which gives a branching ratio $f' \rightarrow K^+K^- / f' \rightarrow K_1^0K_1^0 = 1.0 \pm 0.4$.

For comparison, we can calculate, using the same method, the branching ratio for the φ. This gives a value of 1.2 ± 0.3 for $\varphi \rightarrow K^+K^- / \varphi \rightarrow K_1^0K_2^0$. Thus the branching ratio for the φ is in agreement with the accepted value, but that for the f' is some two and a half standard deviations below that expected.

4.7 The Multineutral Two V^0 Events

It is possible to estimate the contribution from $\Lambda K^0\bar{K}^0\pi^0$ and $\Lambda K^0\bar{K}^0\pi^0\pi^0$ to the missing mass spectrum to ΛK_1^0 (Fig. 4.2) in the events with no charged particles at production. The final state $\Lambda K^0\bar{K}^0\pi^0\pi^0\pi^0$ is omitted because the comparable channel $\Lambda K^0\bar{K}^0\pi^+\pi^-\pi^0$ is not strong. The phase space curve drawn on Fig. 4.2 is that for $K\pi$ from $\Lambda KK\pi$ and has been normalised to the number of events below 900 Mev, where the contribution due to $K\pi\pi$ from $\Lambda KK\pi\pi$ is negligible. The numbers of events obtained in this way for $\Lambda K^0\bar{K}^0\pi^0$ and $\Lambda K^0\bar{K}^0\pi^0\pi^0$ are given in Table 4.

The number of events observed of the type $K_1^0K_1^0$ + neutrals (Fig. 4.3) is much larger than expected from the number of $K_1^0K_1^0$ + neutrals. (No events of these final states were found at Imperial College.) There are two possible explanations for this. First, these are events of the type $\pi^-p \rightarrow K_1^0K_1^0n + \pi^0$'s and secondly they are of the type $K^-p \rightarrow K_1^0K_1^0K_2^0n + \pi^0$'s. The first possibility is incompatible with the determination of the beam contamination. Crennell et al.(30) in a 6 Gev π^-p experiment obtain 178 $K_1^0K_1^0n$ events and 206 $K_1^0K_1^0$ + neutrals events, with a microbarn equivalent of about 18 events per microbarn. In this experiment, assuming a 6% pion contamination and a microbarn equivalent of 5 events per microbarn, we expect about 4 events of the type $\pi^-p \rightarrow K_1^0K_1^0$ + neutrals and 2 events of the type $\pi^-p \rightarrow K_1^0K_1^0n$. We do, in fact, see one event consistent with $\pi^-p \rightarrow K_1^oK_1^on$. The second possibility is quite realistic, and it is noticeable that the missing mass spectrum starts above the K^on threshold. As the φ is the only known resonance decaying to $K_1^oK_2^o$ this final state must go dominately through $\bar{K}^o\varphi n$; a comparable channel $pK^-\varphi$ might then be expected to be strong. This is seen as $pK^-K_1^oK_2^o$ (a topology 201 event) and $pK^-K^+K^-$ (400 event). Unfortunately, the missing mass continuum for the interpretation pK^-K^o of a 201 event with identified K^o is such that any possible K^o peak in the missing mass is swamped by mis-fitted final states of the type $p\pi^-K^o$ + m π^o's; topology 400 events had not been processed at the time of writing, so no data is available for the channel $pK^-\varphi$. We thus conclude that the large number of events in the final state $K_1^oK_1^o$ + neutrals can not be explained by pion contamination in the beam giving final states $K^o\bar{K}^on + \pi^o$'s, but might be explained by $\bar{K}^on\varphi$ production, though we can not confirm this.

TABLE 4

Final State	Observed Number of Events	Correction Factor	Cross-Section (μb)
$\Lambda K^o \overrightarrow{K}^o$ (no φ, f')	24	5.00	12 ± 3
$\Lambda K^+ K^-$ (no φ)	30	1.81	15 ± 3
$\Lambda\varphi$ $(\varphi \rightarrow K_1^o K_2^o)$	16	4.37	7 ± 2
$\Lambda\varphi$ $(\varphi \rightarrow K^+ K^-)$	9	1.81	4.5 ± 1.5
$\Lambda f'$ $(f' \rightarrow K_1^o K_1^o)$	8	2.86	2.2 ± 0.9
1) $\Lambda K_1^o (K^o \pi^o)$	74	1	9 ± 3
1) $\Lambda K_1^o (K^o \pi^o \pi^o)$	18	1	2 ± 1
$\Lambda K^+ K^- \pi^o$ (no φ)	92	1.81	53 ± 8
$\Lambda \varphi \pi^o$ $(\varphi \rightarrow K^+ K^-)$	12	2.33	9 ± 3
2) $\Lambda K_1^o K_1^o \pi^o$	8	7.87	6 ± 2
$\Lambda K^o K^- \pi^+$	15	10.0	22 ± 6
$\Lambda \overrightarrow{K}^o \pi^- K^+$	17	10.0	25 ± 6
$\Lambda \overline{K}^o K^{*o}$ $(K^* \rightarrow K^+ \pi^-)$	6	10.0	9 ± 4
$\Lambda \overline{K}^o K^{*o}$ $(K^* \rightarrow K^o \pi^o)$	3	31.5	9 ± 6
$\Lambda K^- K^{*+}$ $(K^* \rightarrow K^+ \pi^o)$	10	2.33	7 ± 2
$\Lambda K^- K^{*+}$ $(K^* \rightarrow K^o \pi^+)$	5	10.0	7 ± 3
$\Lambda K^o \overleftrightarrow{K}^o \pi^+ \pi^-$ (no φ)	34.5	4.86	24 ± 4
$\Lambda K^+ K^- \pi^+ \pi^-$ (no φ)	34	1.93	15 ± 3
$\Lambda \varphi \pi^+ \pi^-$ $(\varphi \rightarrow K_1^o K_2^o)$	8	4.31	5 ± 2
$\Lambda \varphi \pi^+ \pi^-$ $(\varphi \rightarrow K^+ K^-)$	13	1.93	6 ± 2

continued over ...

TABLE 4 (continued)

Final State	Observed Number of Events	Correction Factor	Cross-Section (μb)
$\Lambda \begin{matrix} K^\circ K^-\pi^+ \\ \bar{K}^\circ K^+\pi^- \end{matrix} \pi^\circ$	46.5	9.07	62 ± 11
3) $\Lambda K_1^\circ K_1^\circ \pi^+\pi^-\pi^\circ$	3	22.2	13 ± 8
$\Lambda \begin{matrix} K^\circ K^-\pi^+ \\ \bar{K}^\circ K^+\pi^- \end{matrix} \pi^+\pi^-$	9	9.95	13 ± 4
$\Sigma^+K^-K^\circ$	1	8.15	1 ± 1
$\Sigma^-K^+\bar{K}^\circ$	10	8.15	9 ± 3
$\Sigma^+\pi^-K^\circ\bar{K}^\circ$ (no φ)	11	8.77	11 ± 3
$\Sigma^-\pi^+K^\circ\bar{K}^\circ$ (no φ)	32	4.08	14 ± 3
$\Sigma^+\pi^-K^+K^-$ (no φ)	21	3.13	24 ± 6
$\Sigma^-\pi^+K^+K^-$ (no φ)	18	1.43	10 ± 2
$\Sigma^+\pi^-\varphi$ ($\varphi \rightarrow K_1^\circ K_2^\circ$)	4	7.09	3.1 ± 1.5
$\Sigma^+\pi^-\varphi$ ($\varphi \rightarrow K^+K^-$)	6	3.13	7 ± 3
$\Sigma^-\pi^+\varphi$ ($\varphi \rightarrow K_1^\circ K_2^\circ$)	10	3.30	3.7 ± 1.2
$\Sigma^-\pi^+\varphi$ ($\varphi \rightarrow K^+K^-$)	9	1.43	4.8 ± 1.6
$\Sigma^+K^-K^\circ\pi^\circ$	7	15.3	12 ± 4
$\Sigma^-K^+\bar{K}^\circ\pi^\circ$	13	6.40	9 ± 3
4) $Y_0^*(1405)K^\circ\bar{K}^\circ$	17	4.96	9 ± 2
4) $Y_0^*(1520)K^\circ\bar{K}^\circ$	10	4.96	5 ± 1.6
3) $\Sigma^+\pi^-K_1^\circ K_1^\circ\pi^\circ$	1	26.8	3 ± 3

continued over ...

TABLE 4 (continued)

Final State	Observed Number of Events	Correction Factor	Cross-Section (μb)
3) $\Sigma^-\pi^+K_1^\circ K_1^\circ\pi^\circ$	4.3	26.8	13 ± 7
$\Sigma^+ \begin{matrix} K^\circ K^-\pi^+ \\ \bar{K}^\circ K^+\pi^- \end{matrix} \pi^-$	15	14.2	24 ± 6
$\Sigma^- \begin{matrix} K^\circ K^-\pi^+ \\ \bar{K}^\circ K^+\pi^- \end{matrix} \pi^+$	18	7.1	14 ± 4
3) $pK^-K^\circ\bar{K}^\circ$	6	17.9	16 ± 7
3) $NK^\circ\bar{K}^\circ\bar{K}\pi$	10	13.1	20 ± 6

<u>Footnotes</u>:- The correction factor is the product of the factors which correct for events not passing the analysis system (1.31 for rare topologies, 1.05 for common topologies), scanning loss (1.1 for rare topologies, 1.0 for common topologies), weight and loss of neutral decays. The error on this factor is 6%.

1) See section 4.7. No corrections have been applied in obtaining the cross-section quoted as the state of the $K^\circ\bar{K}^\circ$ system is not known. Assuming it is pure $K^\circ\bar{K}^\circ$ the correcting factor is 6.6.

2) Assuming that the $K^\circ\bar{K}^\circ$ system is in a pure $K_1^\circ K_1^\circ$ state.

3) Assuming that the $K^\circ\bar{K}^\circ$ system is in a pure $K^\circ\bar{K}^\circ$ state.

4) For the $\Sigma^{\pm}\pi^{\mp}$ decay modes of the Y_0^* only.

Fig. 4.1

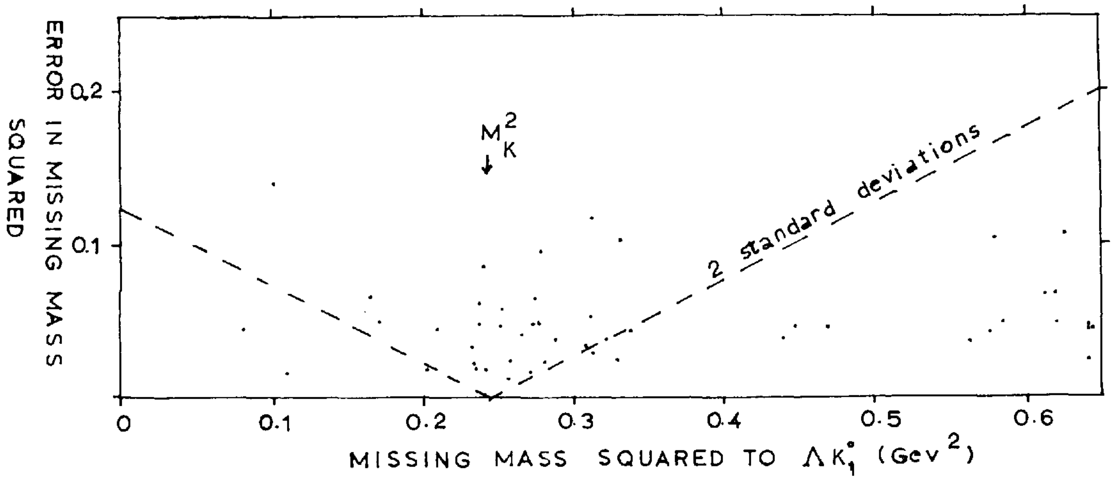

Fig. 4.2

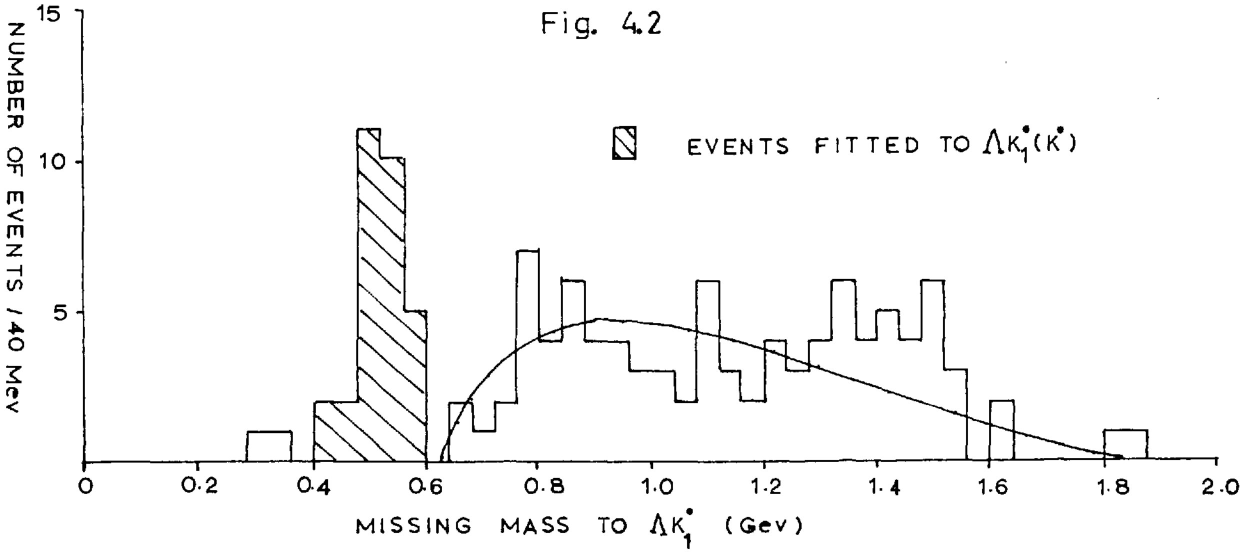

Fig. 4.3

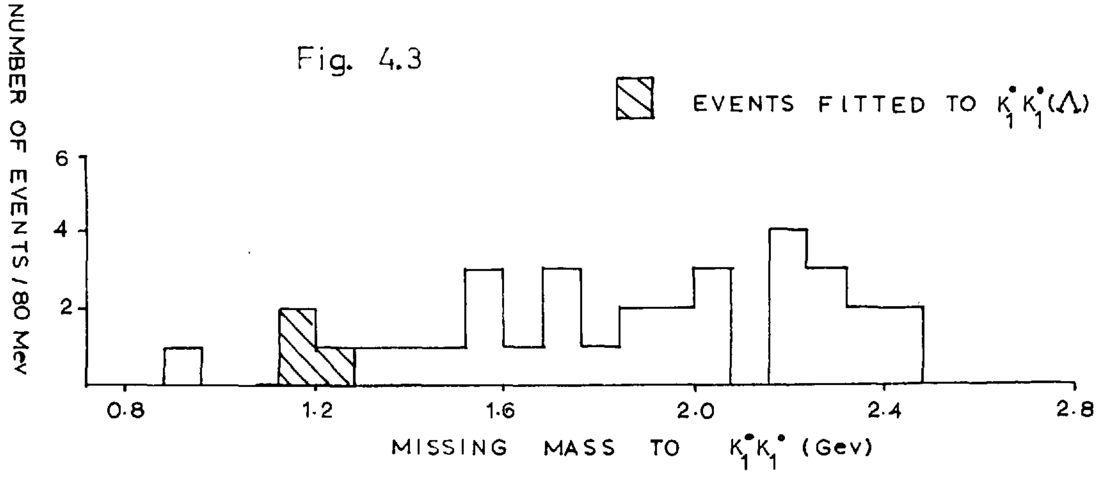

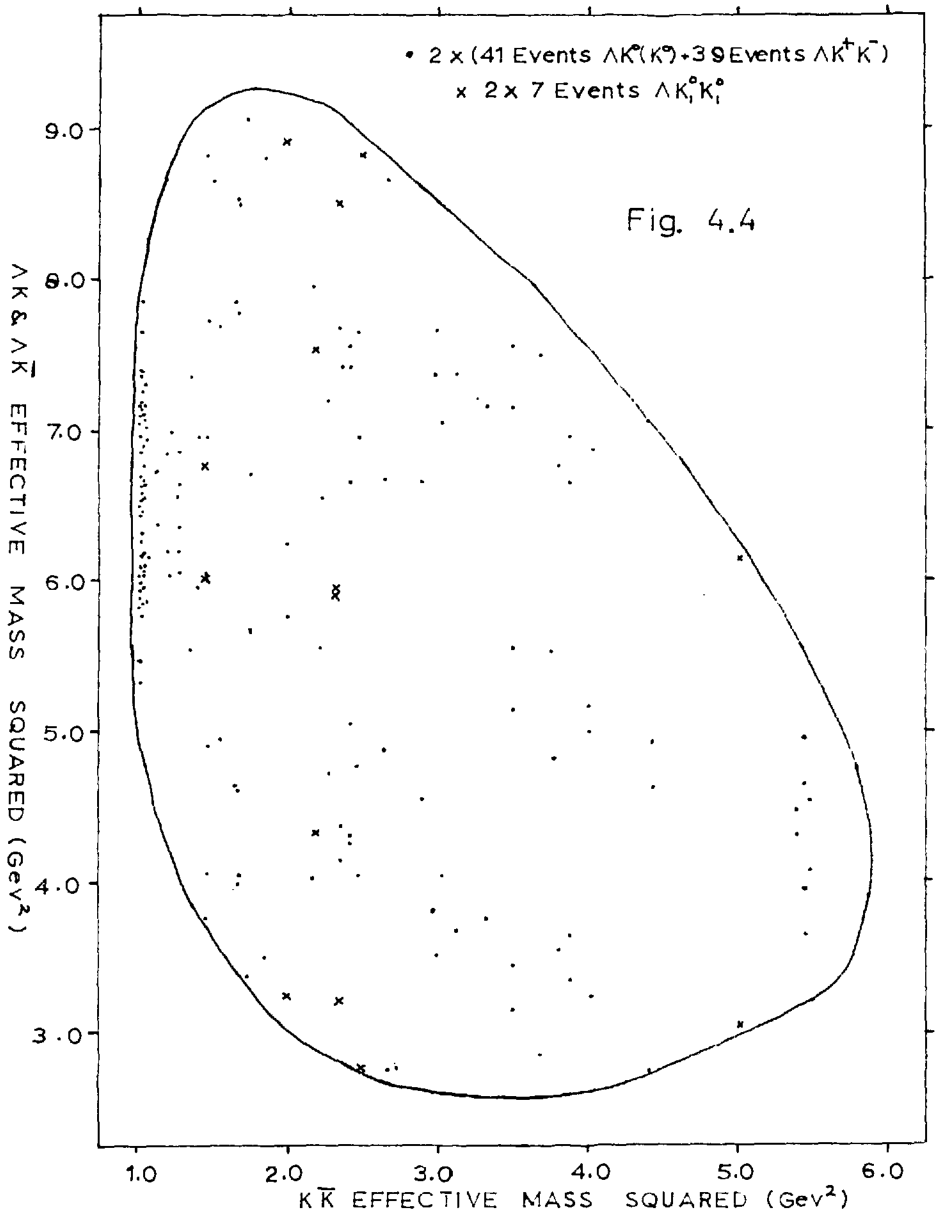

Fig. 4.4

• 2 x (41 Events $\Lambda K^o(\bar{K}^o)$ + 39 Events ΛK^+K^-)
x 2 x 7 Events $\Lambda K_1^oK_1^o$
ΛK & ΛK̄ EFFECTIVE MASS SQUARED (Gev²)
9.0
8.0
7.0
6.0
5.0
4.0
3.0
1.0
2.0
3.0
4.0
5.0
6.0
KK̄ EFFECTIVE MASS SQUARED (Gev²)

Fig. 4.5

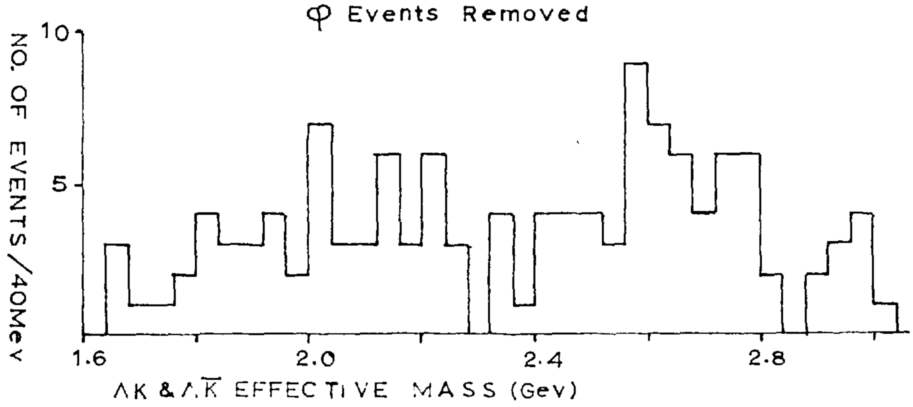

φ Events Removed
NO. OF EVENTS/40MeV
10
5
1.6
2.0
2.4
2.8
ΛK & ΛK̄ EFFECTIVE MASS (Gev)

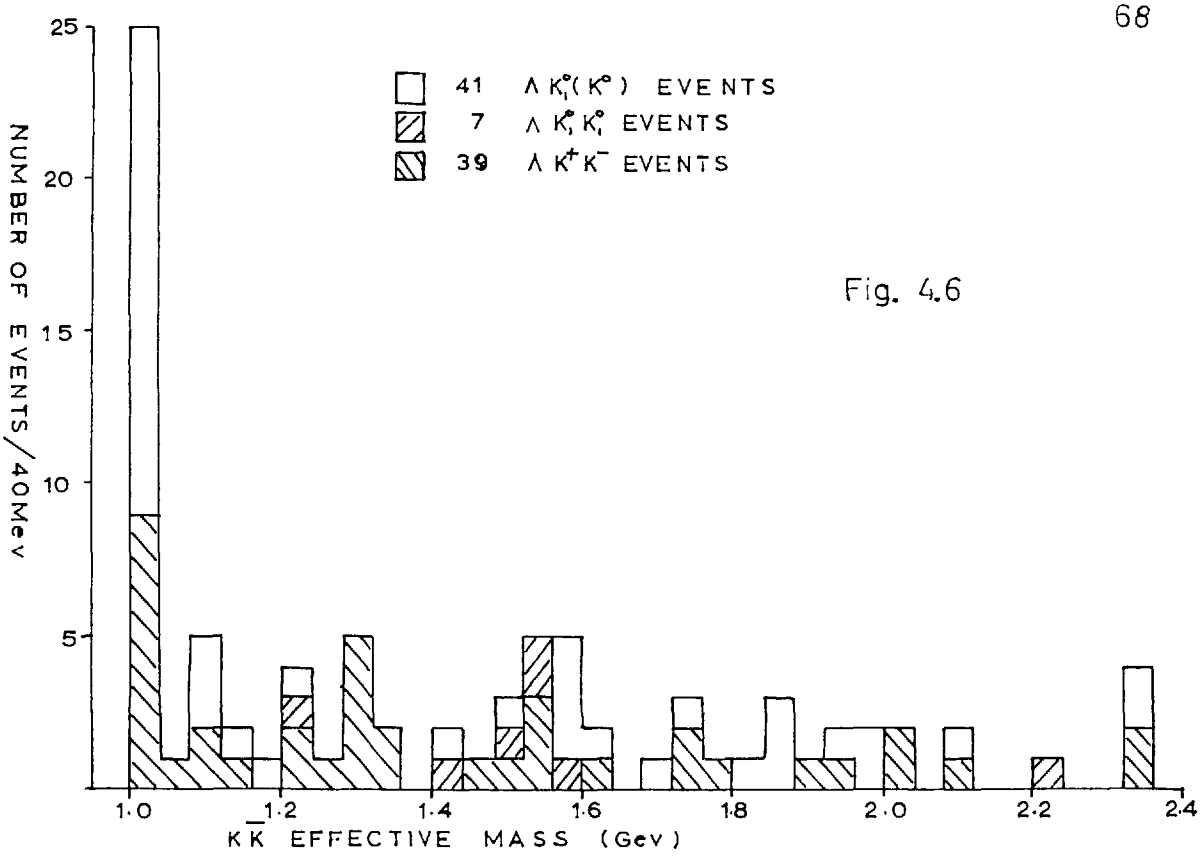

Fig. 4.6

25 $\Lambda\varphi$ EVENTS

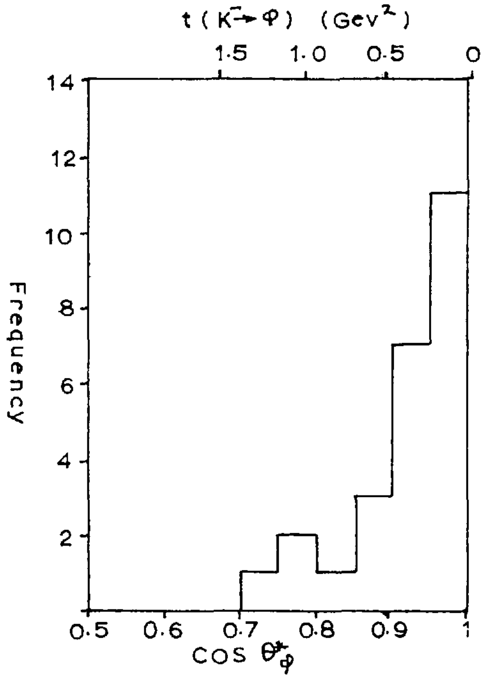

Fig. 4.7

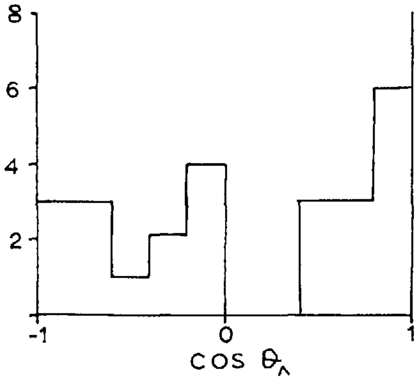

Fig. 4.8

Fig. 4.9

25 Λφ EVENTS

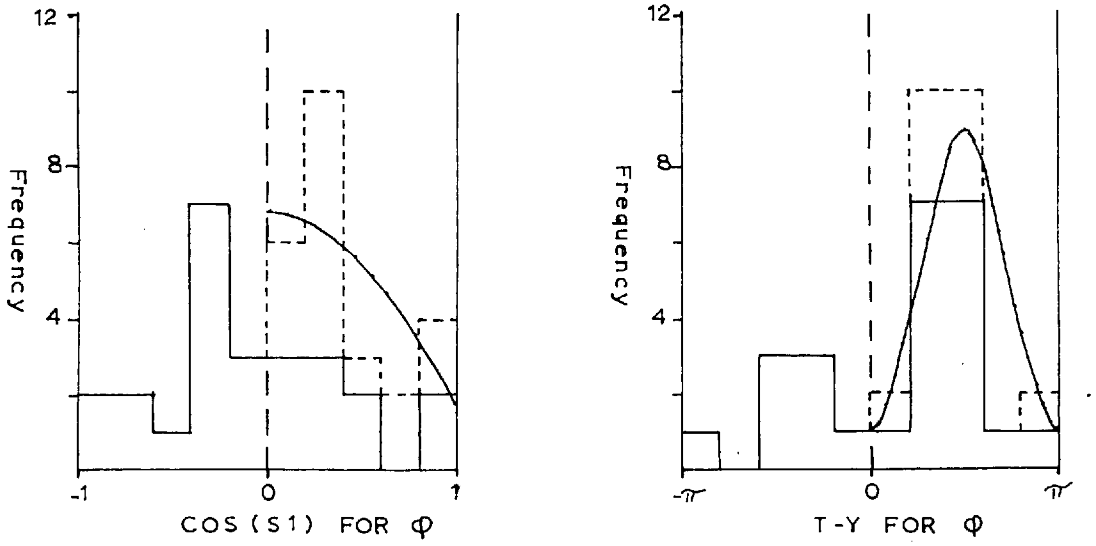

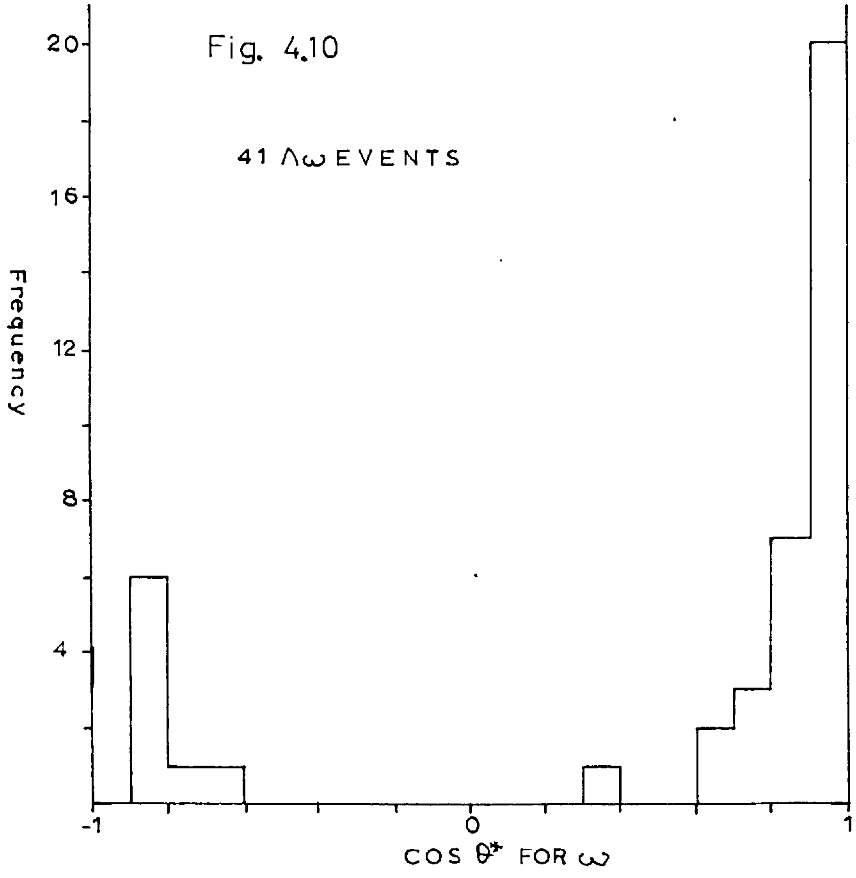
Fig. 4.10

41 Λω EVENTS

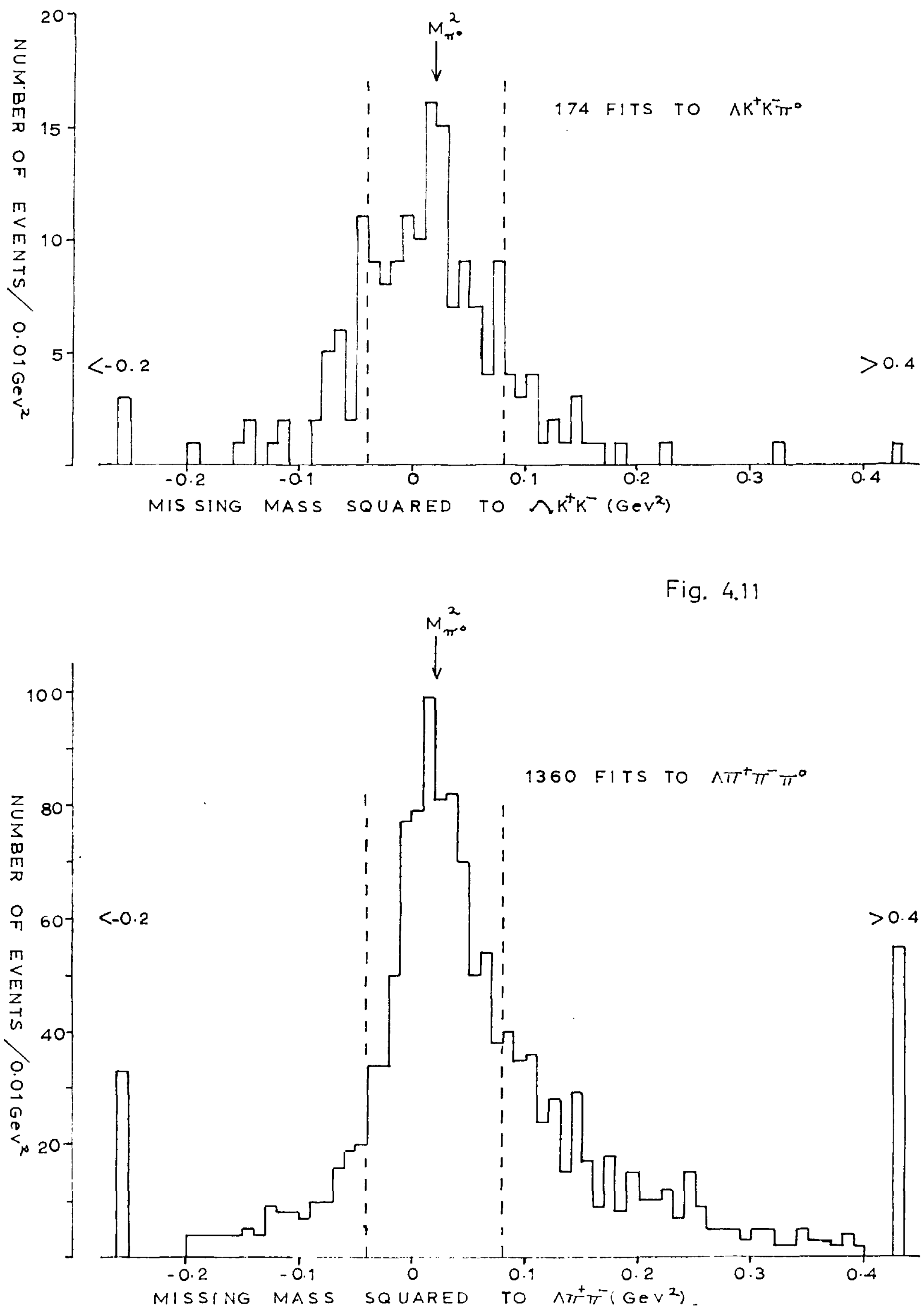
$M^2_{\pi^0}$
174 FITS TO $\Lambda K^+K^-\pi^0$
NUMBER OF EVENTS / 0.01 GeV²
20
15
10
5
<-0.2
>0.4
-0.2
-0.1
0
0.1
0.2
0.3
0.4
MISSING MASS SQUARED TO ΛK^+K^- (GeV²)
$M^2_{\pi^0}$
1360 FITS TO $\Lambda\pi^+\pi^-\pi^0$
NUMBER OF EVENTS / 0.01 GeV²
100
80
60
40
20
<-0.2
>0.4
-0.2
-0.1
0
0.1
0.2
0.3
0.4
MISSING MASS SQUARED TO $\Lambda\pi^+\pi^-$ (GeV²)

Fig. 4.11

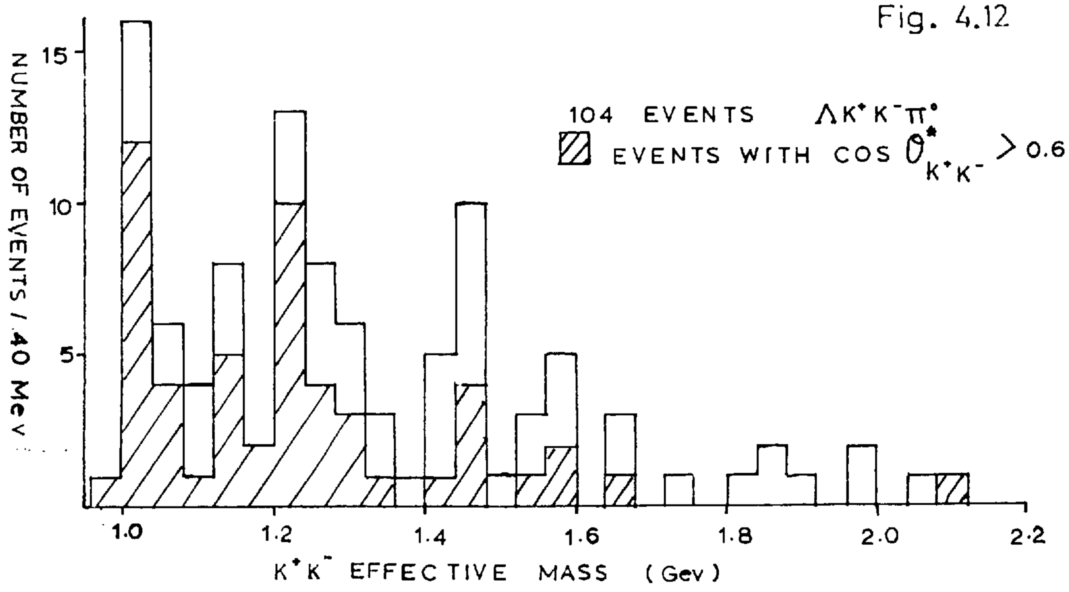

Fig. 4.12

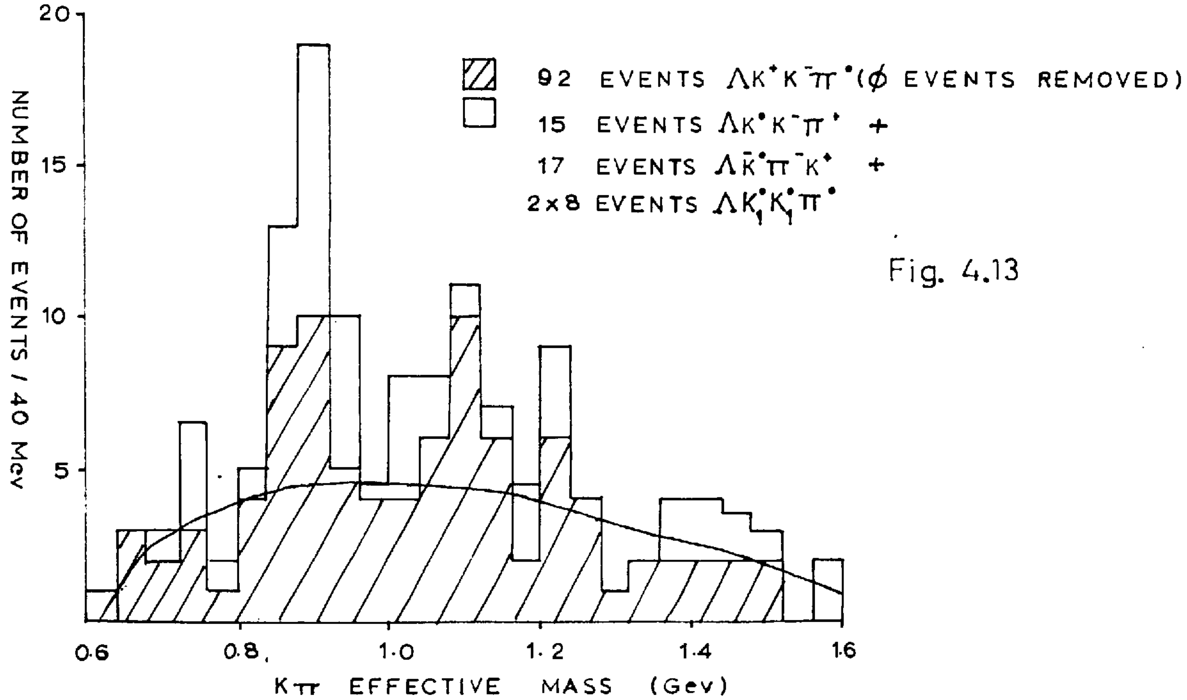

Fig. 4.13

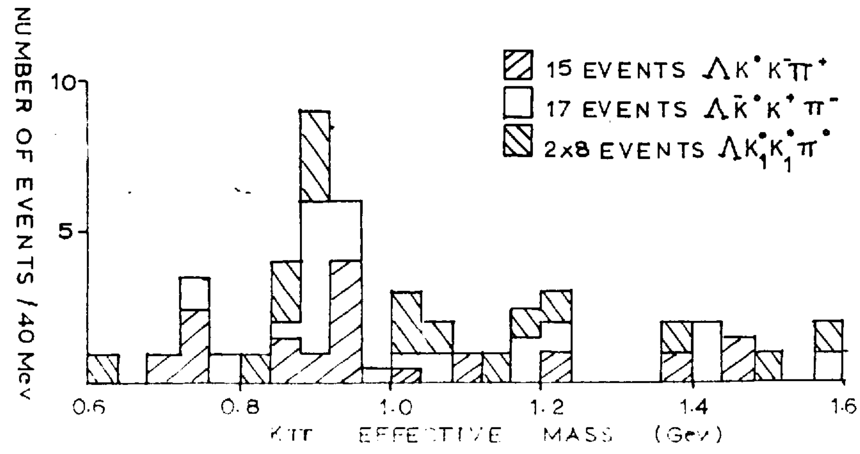

Fig. 4.14

Fig. 4.15

16 EVENTS IN $\Lambda\phi\pi^{\circ}$ FROM $\Lambda K^{+}K^{-}\pi^{\circ}$

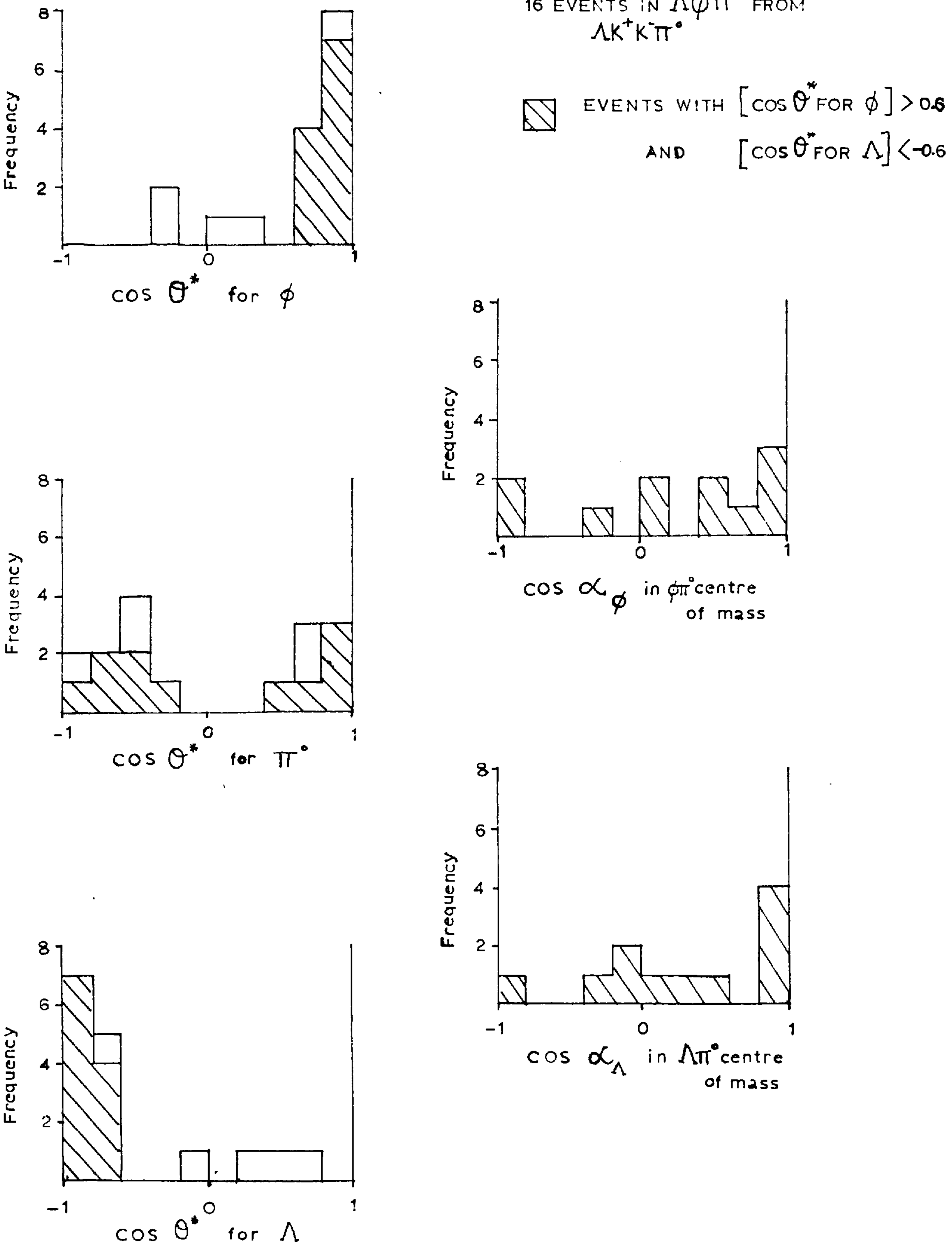

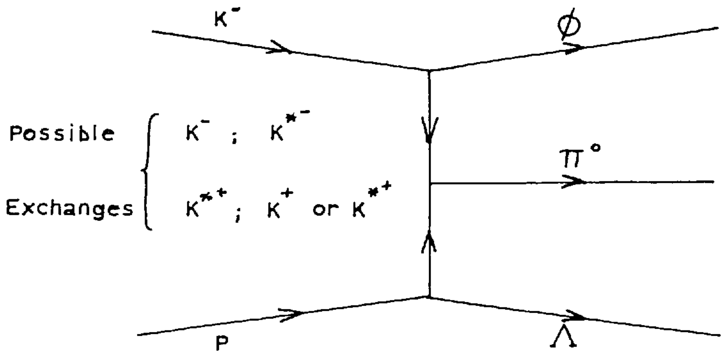

Fig. 4.16

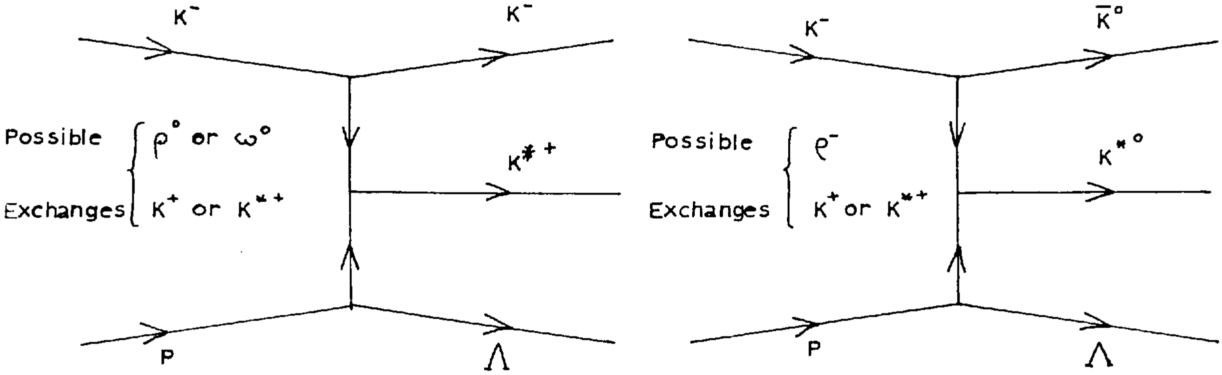

Fig. 4.17

Fig.4.18

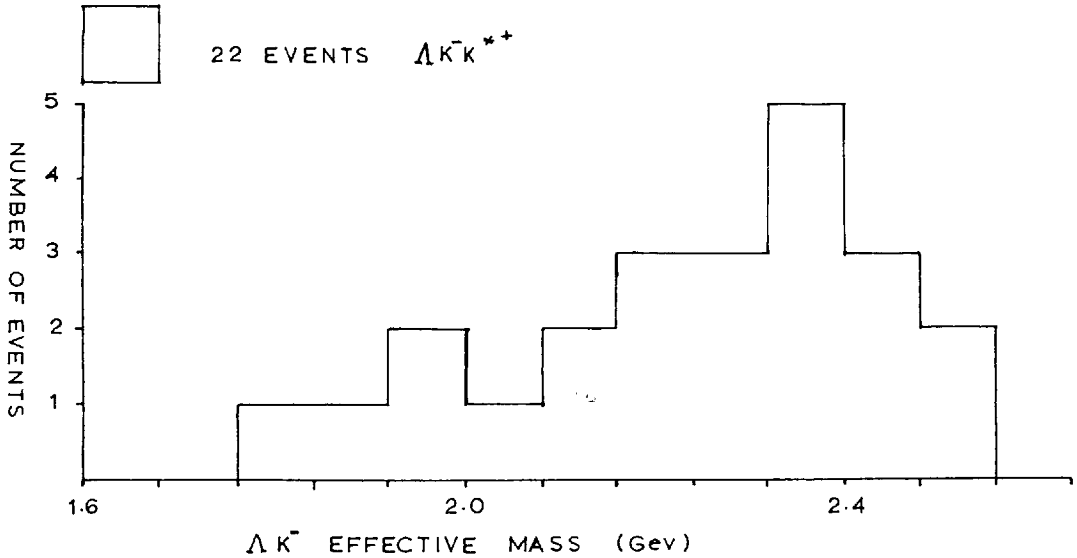

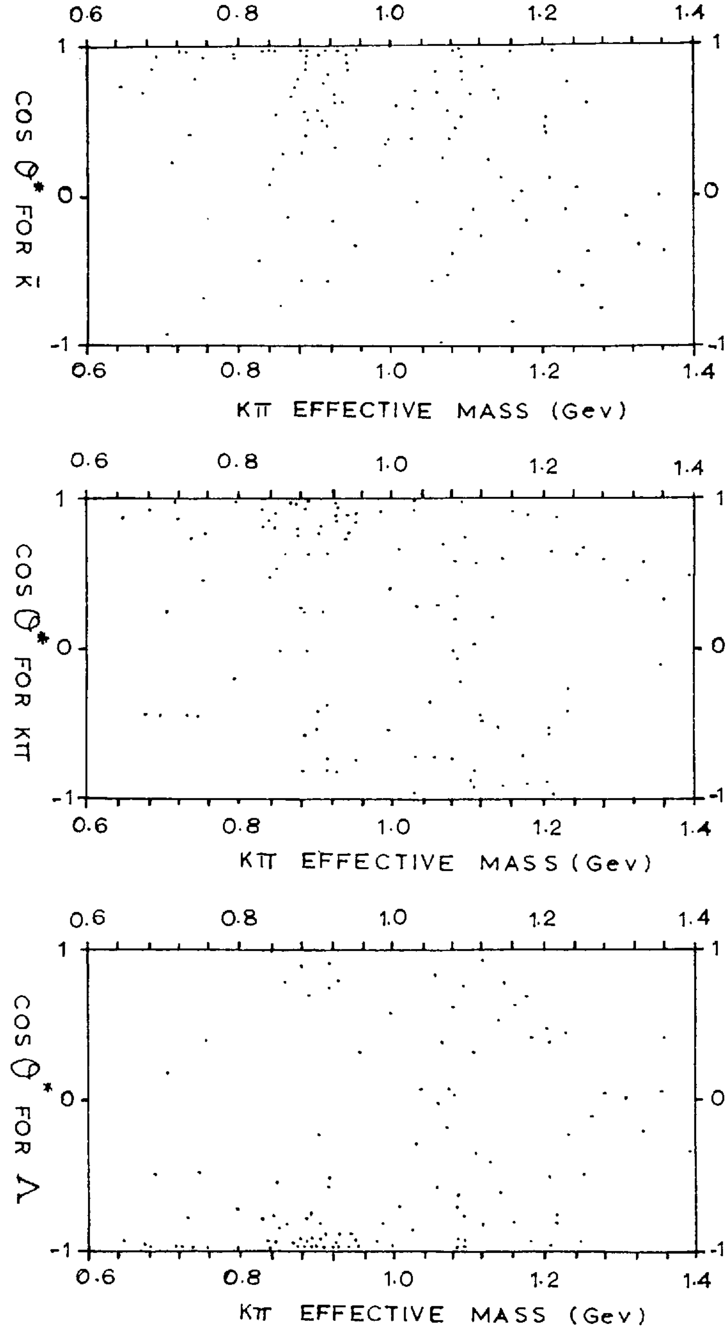

Fig. 4.19

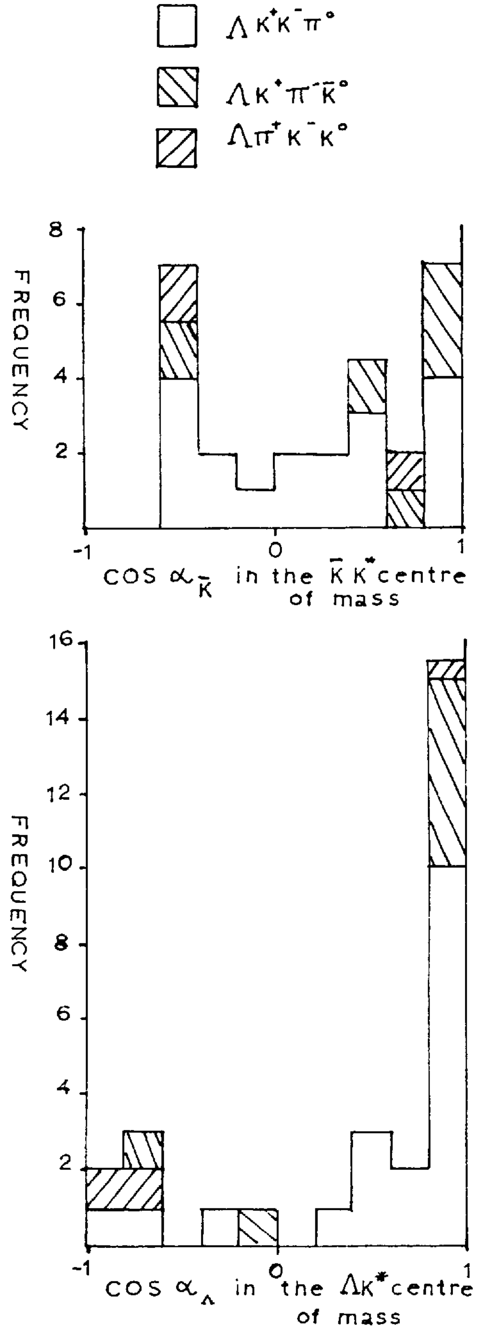

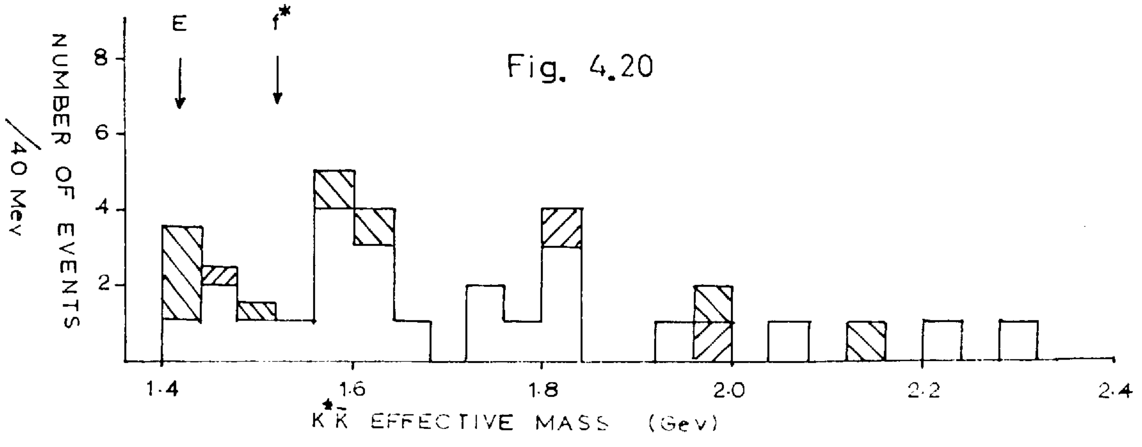

Fig. 4.20

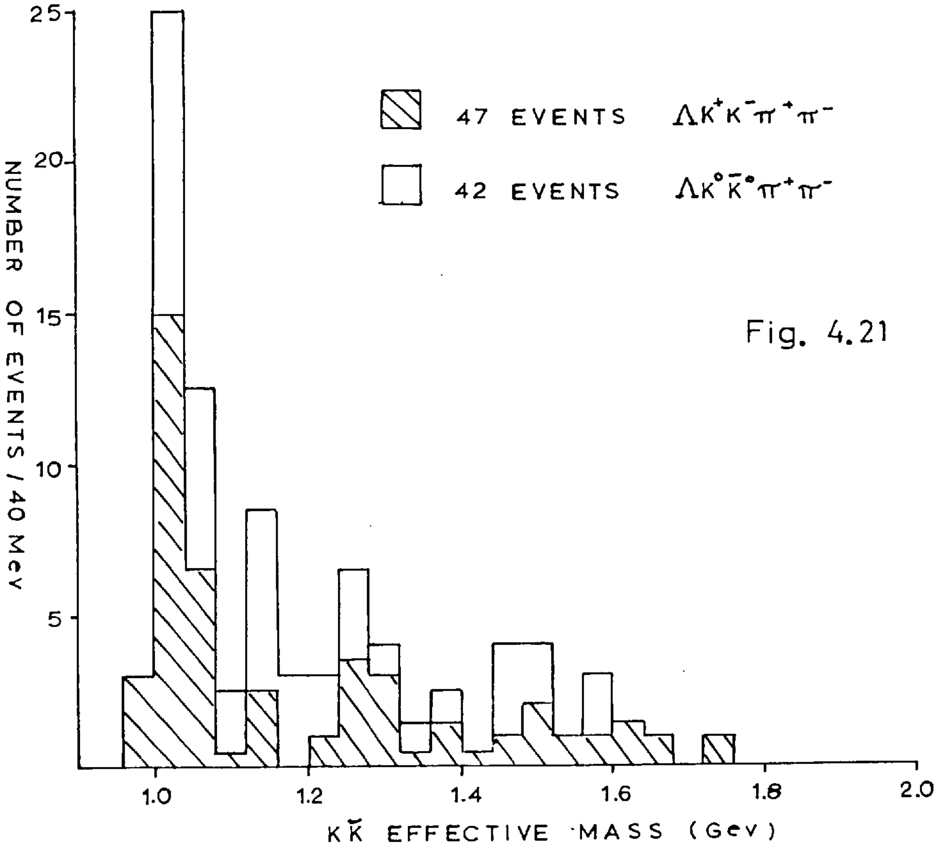

Fig. 4.21

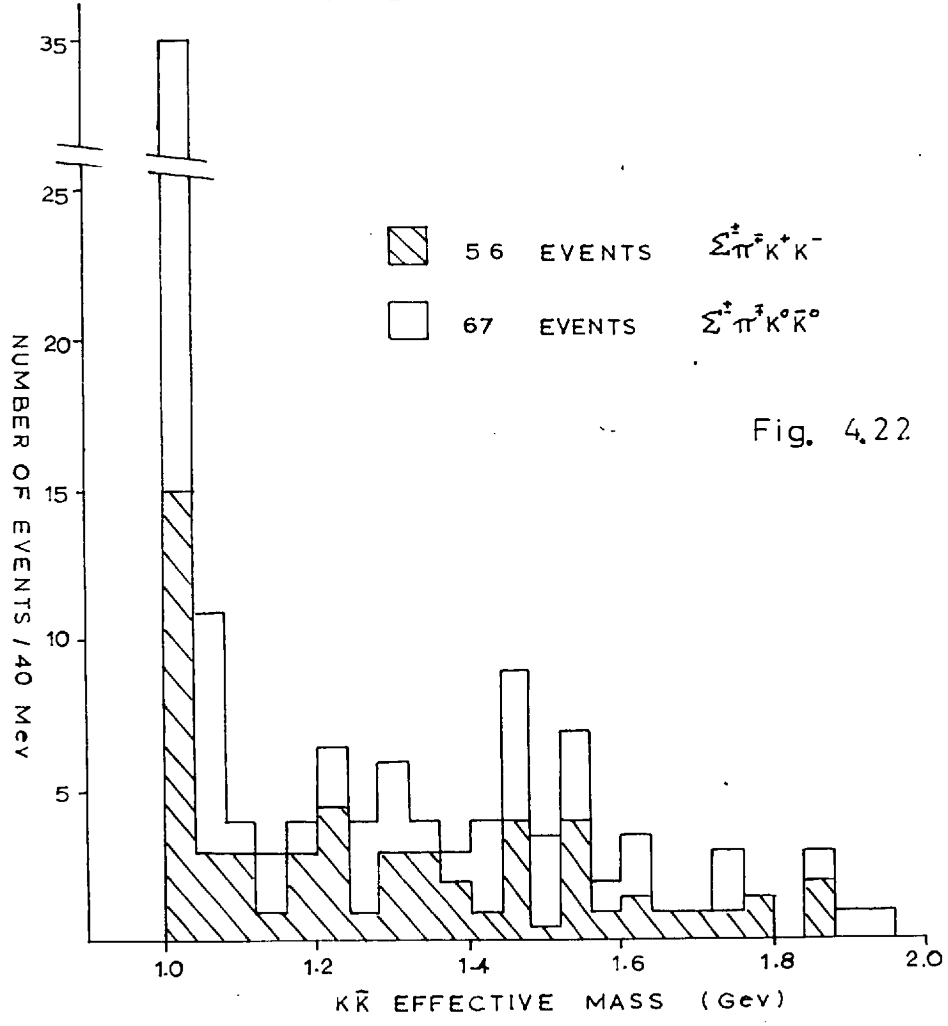

Fig. 4.22

ANGULAR DISTRIBUTIONS FOR 25 EVENTS $\Lambda\phi\pi^+\pi^-$

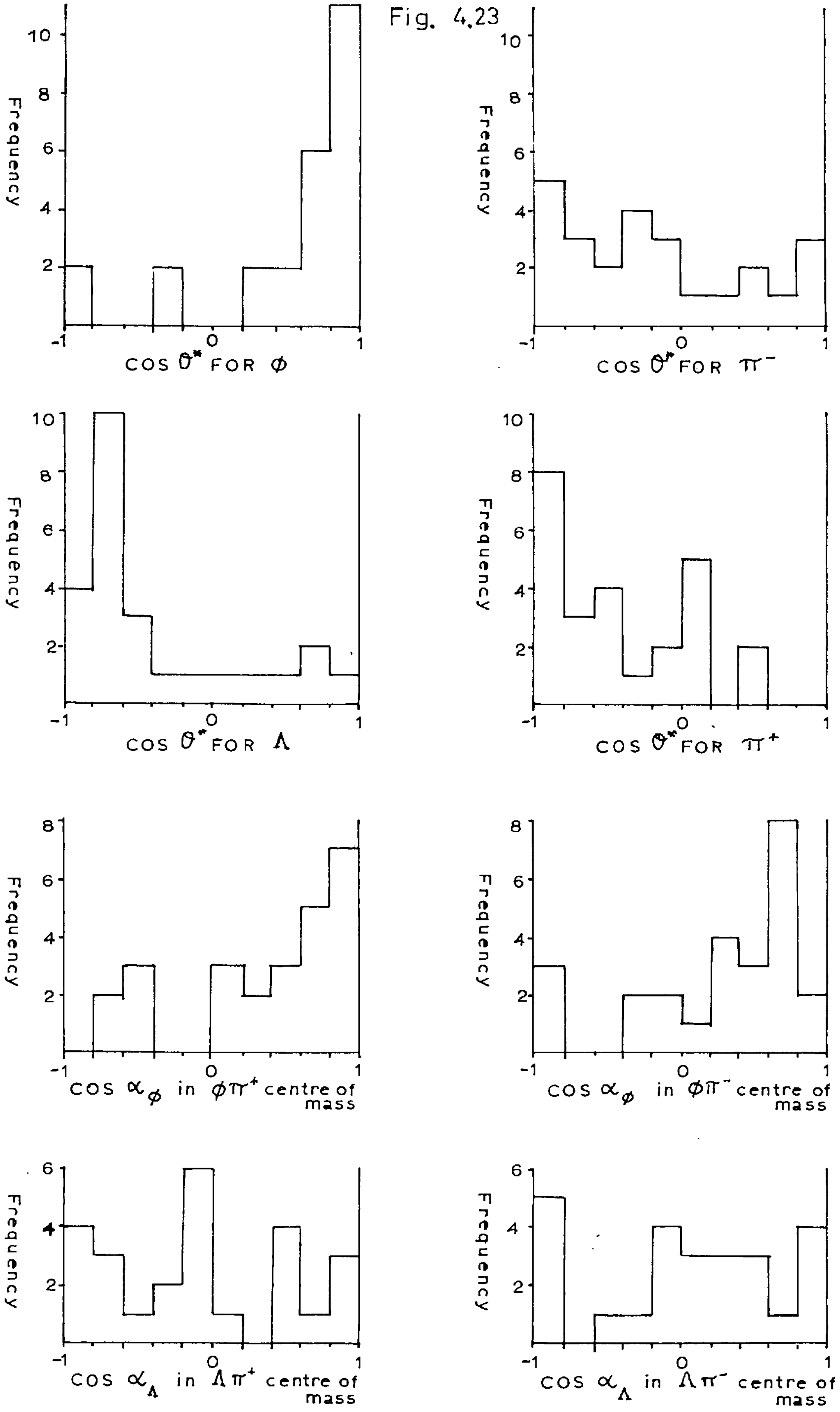

Fig. 4.23

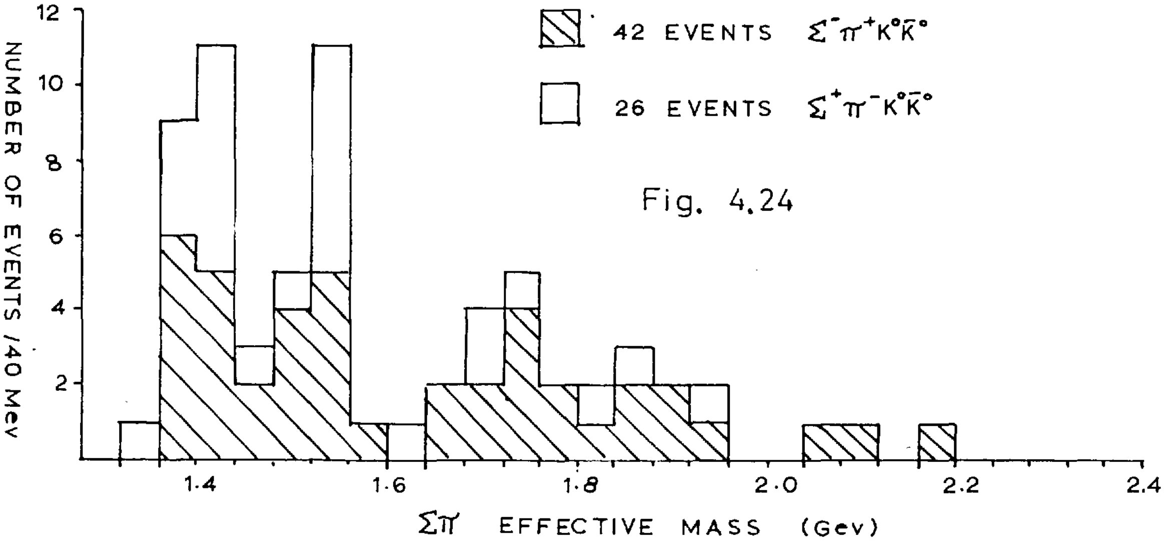

Fig. 4.24

Fig. 4.25

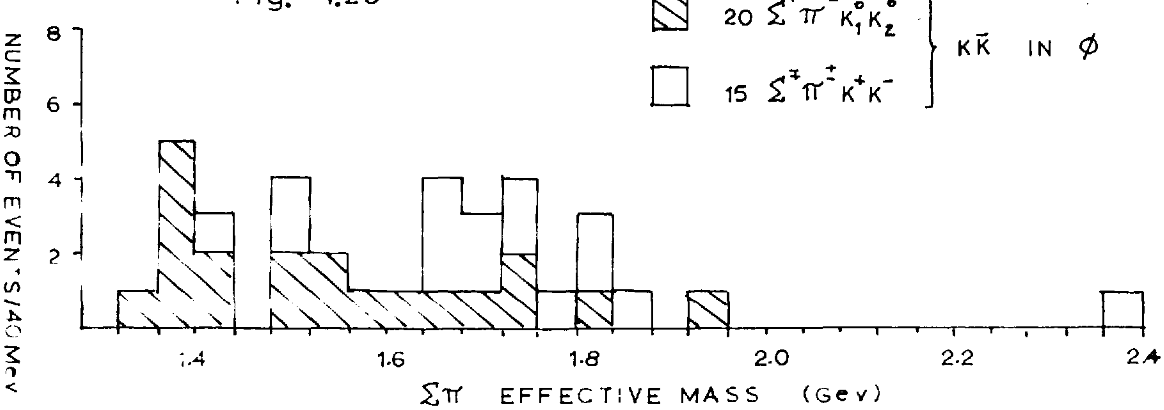

Fig. 4.26

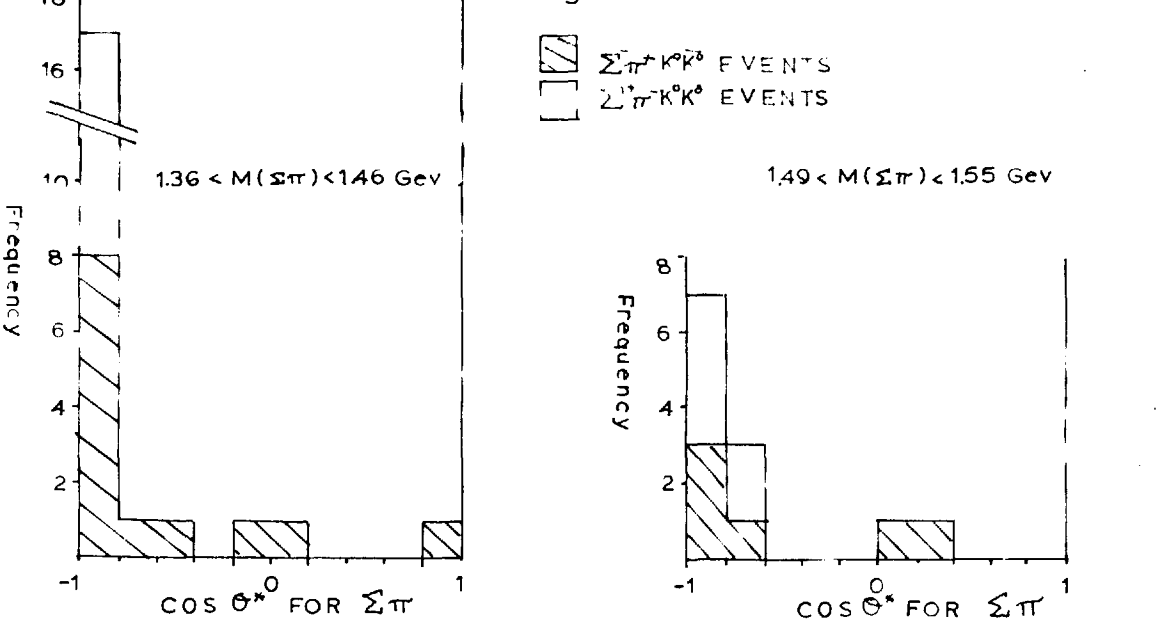

Fig. 4.27 35 EVENTS $\Sigma^{\pm}\pi^{\mp}\phi$

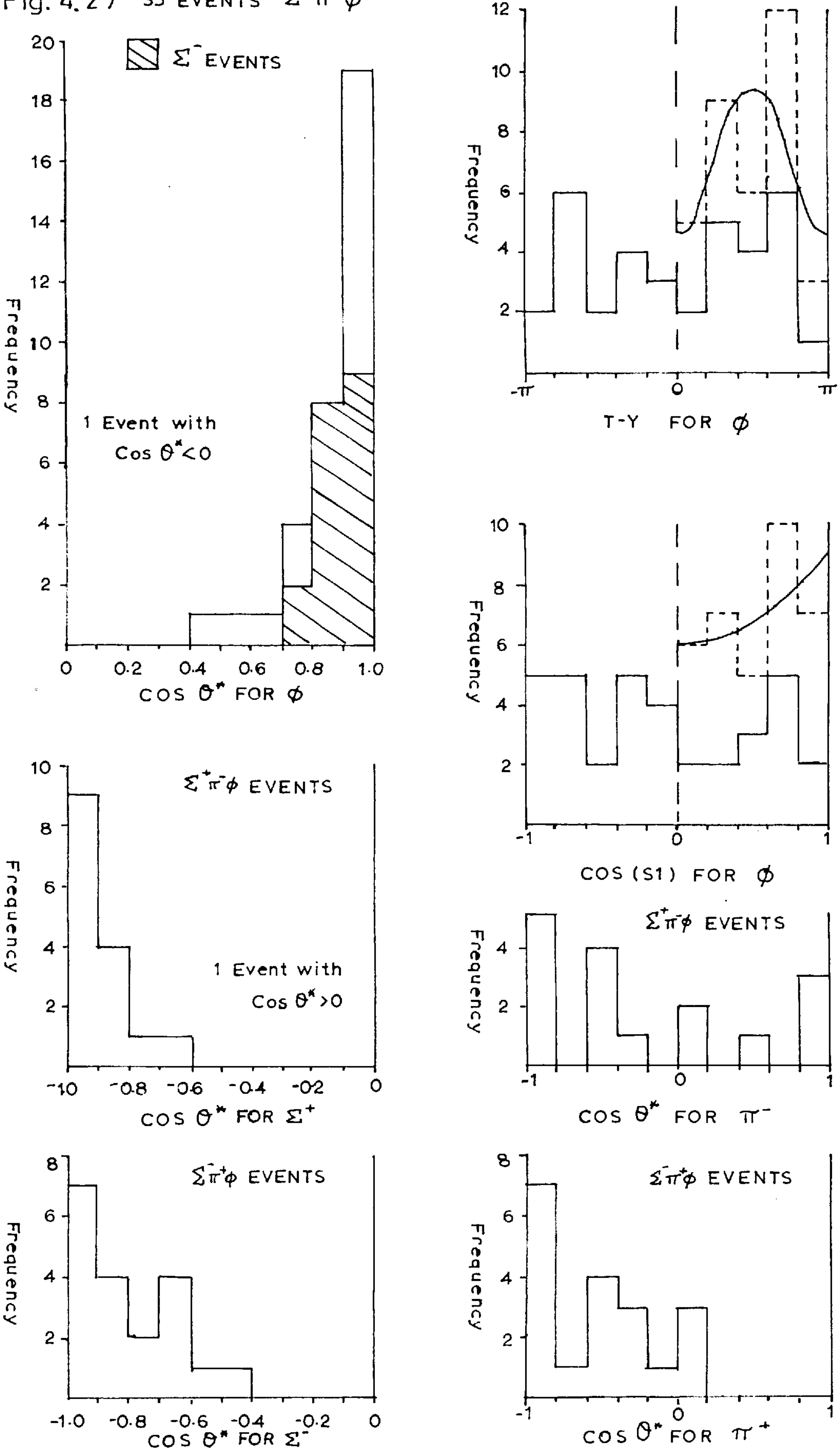

Fig. 4.28 15 $\Sigma^+\pi^-\phi$ EVENTS

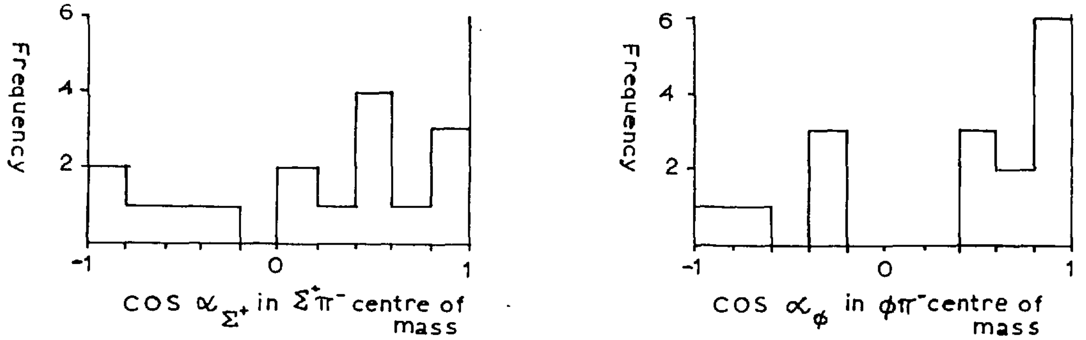

19 $\Sigma^-\pi^+\phi$ EVENTS

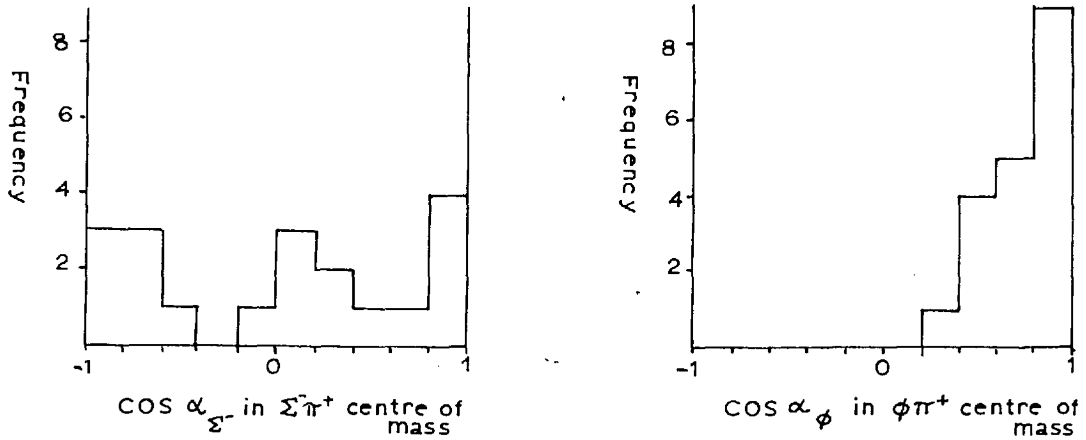

Fig. 4.29 10 $\Sigma^-K^+\bar{K}^0$ EVENTS

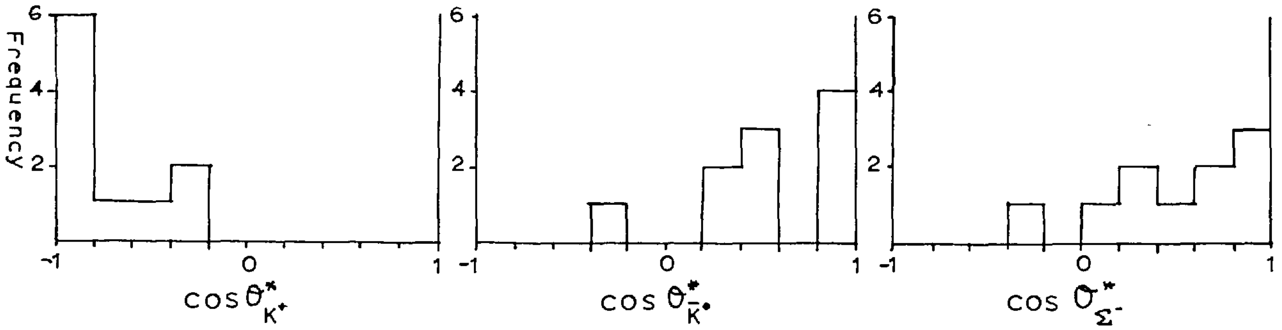

Fig. 4.30 25 $\Lambda\pi^+\pi^-\phi$ EVENTS

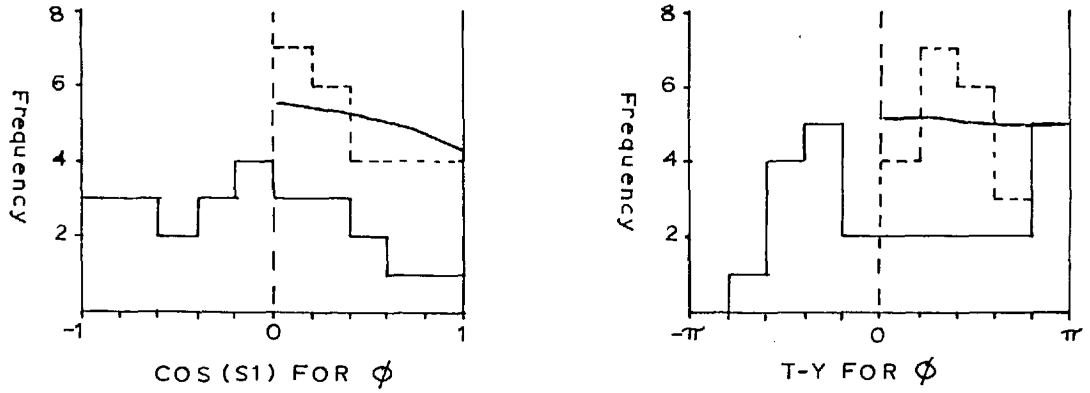

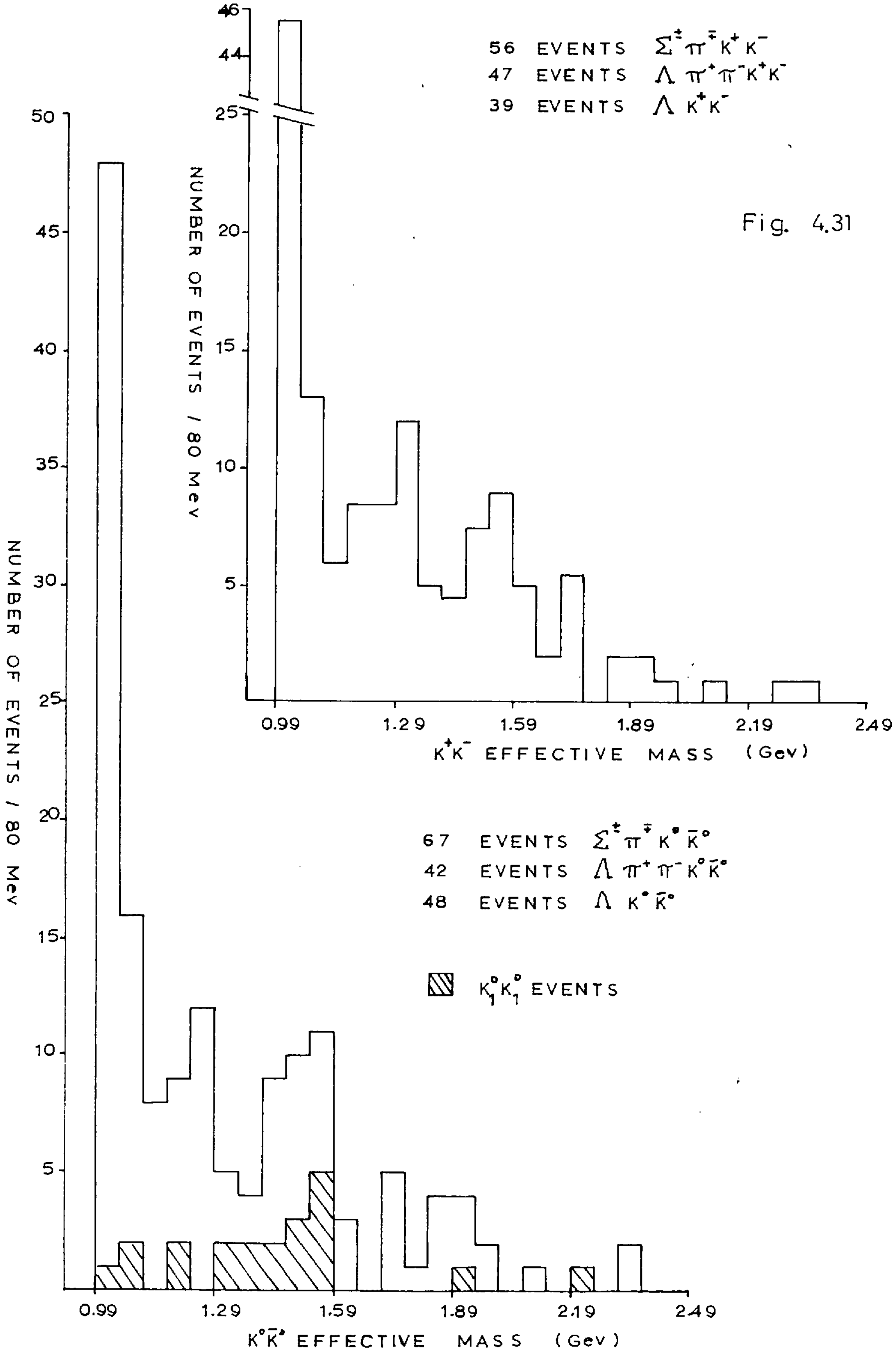
56 EVENTS $\Sigma^{\pm}\pi^{\mp}K^{+}K^{-}$
47 EVENTS $\Lambda\pi^{+}\pi^{-}K^{+}K^{-}$
39 EVENTS $\Lambda K^{+}K^{-}$
NUMBER OF EVENTS / 80 Mev
46
44
25
20
15
10
5
0.99
1.29
1.59
1.89
2.19
2.49
$K^{+}K^{-}$ EFFECTIVE MASS (Gev)
67 EVENTS $\Sigma^{\pm}\pi^{\mp}K^{0}\bar{K}^{0}$
42 EVENTS $\Lambda\pi^{+}\pi^{-}K^{0}\bar{K}^{0}$
48 EVENTS $\Lambda K^{0}\bar{K}^{0}$
▨ $K_1^0K_1^0$ EVENTS
NUMBER OF EVENTS / 80 Mev
50
45
40
35
30
25
20
15
10
5
0.99
1.29
1.59
1.89
2.19
2.49
$K^{0}\bar{K}^{0}$ EFFECTIVE MASS (Gev)

Fig. 4.31

CHAPTER FIVE

NEGATIVE HYPERON PRODUCTION

Some aspects of Ξ^-, Σ^- and $Y^{*-}(1385)$ production are examined here, and, because they occur in the same final states and are of great interest for comparison with the corresponding φ channels, the channels $\Sigma^\pm\pi^\mp\omega$ and $\Lambda\pi^+\pi^-\omega$ are also examined. As before, cross-sections are tabulated at the emd of the chapter in Table 5.

A straightforward qualitative explanation of peripheral positive and neutral hyperon production in K^-p collisions is afforded by the simple one meson exchange model. Thus processes such as

$$K^-p \rightarrow \Lambda\pi^0 \quad \text{and} \quad K^-p \rightarrow Y^{*+}\pi^-$$

may be represented by the diagrams of Fig. 5.1a,b. However, we cannot construct such simple diagrams as these for the production of negative hyperons unless a doubly charged meson exists, and no such meson has yet been discovered. A baryon exchange diagram, though, is easily drawn for a process such as

$$K^-p \rightarrow Y^{*-}\pi^+ \qquad \text{(Fig. 5.2a)}$$

All charge states of hyperons can appear in the final state of a meson exchange interaction if it proceeds through a $Y + n\pi$ $(n \geqslant 1)$ state, which may or may not be resonant, such as that of Fig. 5.2b.

The production of Ξ^- by peripheral interactions with meson exchange is doubly restricted by charge and strangeness, as the exchanged meson would be required to have two units of strangeness as well as of charge. Moreover, a positive strangeness K meson, which can give further information about the nature of the interaction, must also be produced together with the Ξ^-.

In final states of high multiplicity the peripheral picture of interactions is not, on the face of it, valid. However, in final states such as $\Sigma^{\pm}\pi^{\mp}\pi^+\pi^-\pi^0$ the hyperon is strongly peaked backwards, suggesting that even here peripheral interactions play an important role.

5.1 Ξ^- Production

The loss of Ξ^- decaying at small angles when the Λ is seen has been estimated in section 3.6. A histogram of L/P has been made to estimate the losses of short and long lived Ξ^- (Fig. 5.4; L is the length of the Ξ^- track and P its momentum in centimetres and Gev respectively). These corrections have been determined from the histogram of the number of Ξ^- which decay within a certain range of L/P (line A), and they have then been used to draw the cumulative plot from which the Ξ^- lifetime can be estimated (line B). This gives a value of $(1.7 \pm 0.2) \times 10^{-10}$ seconds for the Ξ^- lifetime. A similar process has been applied to the Λ's from the Ξ^- decay (Fig. 5.4) and the two corrections so obtained have been used in calculating the cross-sections for Ξ^- final states.

A considerable fraction of the total Ξ^- production proceeds through channels giving three or more pions in the final state. The low cross-section and the large number of final states populated results in there being insufficient events in any single final state to allow a study of resonance production. Some $\Xi^{*0}(1530)$ is observed in the channels $\Xi^-K^+\pi^+\pi^-$ and $\Xi^-K^+\pi^+\pi^-\pi^0$ (Figs. 5.11 and 5.12), but there is no significant production of this resonance in other final states, or of any other resonance, save possibly some $K^*(890)$, in any of the Ξ^- final states observed. Our attention is therefore directed towards the production angular distributions of the Ξ^- and the K.

In the two body channel Ξ^-K^+ the production angular distribution of the Ξ^- (Fig. 5.5) is peaked sharply forwards. This may be taken as an indication of a hyperon exchange mechanism, the forward hyperon peak corresponding to the forward meson peak in a meson exchange reaction. Assuming the differential cross-section is given by exp (-Au), where u is the 4-momentum transfer from the incoming K to the outgoing Ξ^- we obtain

$$A = 2.4 \pm 1 \text{ Gev}^{-2} \quad \text{(neglecting the backward event.)}$$

Kinematically fitted Ξ^- events containing one or more pions have been examined by plotting the Ξ^- production angle against the K production angle (Figs. 5.6 and 5.7). The philosophy behind this is as follows. If we attempt to explain Ξ^- production by simple Feynman diagrams there are four basic particle exchange types (t- and u-channel) that we can draw (Fig. 5.3a - d), and one s-channel diagram (Fig. 5.3e). The contributions from pions have been ignored except where they form a necessary external line, and the states π, K, N, Y and Ξ are meant to represent only the B and S quantum numbers of the particles involved. Furthermore, there is no reason for restricting the internal lines to resonant states. Now, if we assume that the characteristic of the one meson exchange diagram (i.e. that a particle produced at the upper vertex is peaked forward, while one produced at the lower vertex is peaked backwards) applies to all these diagrams, then their main contributions to the Ξ v K production angle plots should occur in the regions indicated in Fig. 5.9. The diagram of Fig. 5.3e would be expected to contribute to the whole of the plot, though not necessarily uniformly as the distribution would depend upon the amplitudes of the partial waves involved. Higher order diagrams will only tend to destroy any peaking, so there should be no serious danger of misinterpretation if any strong peaking is observed.

Comparing these simple ideas with the experimental data (Figs. 5.6, 5.7), we see that in all final states there is a clustering of the events in which the Ξ^- is produced forward and the K is produced backwards, suggesting that hyperon exchange (Fig. 5.3a) is occurring. There is also a slight clustering of events in the region corresponding to a meson exchange interaction (Fig. 5.3b) in $\Xi K\pi\pi\pi$ and possibly in $\Xi K\pi\pi$. A plot of the Ξ production angle against its scattering angle (here α_{Ξ} is the direction of the Ξ with respect to the incoming proton, Fig. 5.10) for $\Xi^- K^+\pi^+\pi^-$ and $\Xi^- K^+\pi^+\pi^-\pi^0$ makes this clearer. This, therefore, appears to be evidence for the existence of a meson of strangeness 2, or possibly for a process in which two mesons of strangeness 1 are exchanged. However, it should be remembered that some processes which produce forward peaking of the hyperon can also produce a small backward peak so that the above interpretation is not necessarily valid.

The production angular distribution for all (i.e. including those events which were not kinematically fittable at the production vertex) Ξ^- with the Λ from its decay seen shows a substantial forward peak as well as a large isotropic component and a small backward peak (Fig. 5.8). This data is dominated by final states with three or more pions, further substantiating the early remarks concerning the importance of peripheral-like production in high multiplicity events. In general, the K is not identifiable in events which are not kinematically fittable at production, so no two dimensional plot can be made.

5.2 Σ^{-} Production

At an early stage in the experiment it was decided not to measure events with the topology 210 as it was expected that very few of them would give successful kinematic fits. The data on $\Sigma^{\pm}$ production is thus restricted to the rare channels and to the four and five body final states from events with topology 410.

Cuts of 3 standard deviations and at ± 0.16 Gev^2 were applied to the missing mass squared to select the five body final states $\Sigma^{\pm}\pi^{\mp}\pi^{+}\pi^{-}\pi^{0}$. A comparison of weighted and unweighted histograms for $\Sigma^{\pm}\pi^{\mp}\pi^{+}\pi^{-}$ and $\Sigma^{\pm}\pi^{\mp}\pi^{+}\pi^{-}\pi^{0}$ showed that the weighting was not changing their shape significantly, so only unweighted plots are shown. The explanation of this is that the empirical weighting factor roughly counteracts the effect of the exponential factor correcting for the loss of short decaying tracks. The exponential term dominates, and for Σ^{+} events with a minimum length cut-off of 0.6 cm. the weight at 300 Mev is about 2.8, while at 600 Mev it is about 1.8, decreases to a minimum of 1.46 at 1.4 Gev and then rises again at higher momenta. Moreover, there are very few events with the momentum of the Σ^{+} less than 400 Mev. The variation in weight for Σ^- events is even less because the Σ^- lifetime is longer than that of the Σ^+.

Only those events in which the Σ^+ decays to $n + \pi^+$ have been used.

$\Sigma^\pm\pi^\mp\pi^+\pi^-$ Final States

The neutral $\Sigma\pi$ effective mass distribution (Fig. 5.13) shows evidence for $Y_0^*(1405)$ and $Y_0^*(1520)$ production and a small peak at about 1800 Mev. In the region of the Y_0^*'s (taken as 1.36 to 1.46 and 1.49 to 1.55 Gev) the Σ production angular distributions (Fig. 5.14) are peaked sharply backwards. Outside these regions the Σ's are produced nearly isotropically, though there is still a backward peak (Fig. 5.15). Both Σ^+ and Σ^- have very similar angular distributions even in non-resonant events where they might have been very different as they are in $\Sigma^\mp K^\pm K^0$, the Σ^- being all forward (Fig. 4.29) and the one Σ^+ going backwards.

A two dimensional plot (not shown) of $\Sigma^\pm\pi^\mp$ effective mass against production angle suggested that the peak around 1800 Mev is probably a mixture of the Y_0^*'s at 1660, 1765 and 1815 Mev, though the number of events is too small to make the situation clear. The number of events in this peak is sufficient to account for the backward peak in Fig. 5.15. Thus it appears that Σ's are produced essentially isotropically when they are not resonant with pions.

$\Sigma^\pm\pi^\mp\pi^+\pi^-\pi^0$ Final States

$Y_0^*(1405)$ and $Y_0^*(1520)$ are both present in the neutral $\Sigma\pi$ effective mass distribution for these final states (Fig. 5.16). No other hyperon resonance is observed in this mass combination, and in particular

$Y_1^{*o}(1660)$ is not produced - an upper limit of 12 events corresponding to a cross-section $< 7\,\mu b$. In these final states, in contrast to the previous ones, both Σ^+ and Σ^- are peaked strongly backwards in the non-Y_o^* events (Fig. 5.17). The backward peaking in the Y_o^* regions is not significantly greater than in the rest of the events (Fig. 5.18). There is, however, no evidence for strong Y^* formation in other mass combinations.

The $\pi^+\pi^-\pi^o$ effective mass spectrum shows evidence for ω production (Fig. 5.19) no significant proportion of which is associated with the Y_o^*'s (Fig. 5.20). The $\Sigma^{\pm}$ and ω production angular distributions (Fig. 5.21) indicate that the process has a peripheral nature and they also show a small backward peak for the ω. Thus these channels ($\Sigma\pi\omega$) account for some of the backward peaking of the Σ's that do not form Y_o^*'s. The ω decay distributions (Fig. 5.21) give spin density matrix elements (calculated after background subtraction)

$$\rho_{11} = 0.62 \pm 0.11 \; ; \qquad \rho_{1\,-1} = 0.24 \pm 0.20 \; ; \quad \mathrm{Re}\,\rho_{10} = 0.08 \pm 0.10 .$$

Unfortunately, the $\omega\pi$ scattering angle is not available owing to limitations of the statistics program.

5.3 $Y_1^{*-}(1385)$ Production

$Y_1^{*-}(1385)$ production in $\Lambda\pi^+\pi^-$ and $\Lambda\pi^+\pi^-\pi^o$ is consistent with zero$^{(31)}$ so our attention is confined to $\Lambda\pi^+\pi^-\pi^+\pi^-$ and $\Lambda\pi^+\pi^-\pi^+\pi^-\pi^o$ where there are peaks at the $Y_1^*(1385)$ mass in both $\Lambda\pi^+$ and $\Lambda\pi^-$ effective mass distributions (Figs. 5.22 and 5.24). It is interesting to note that a $Y_1^{*-}(1385)$ is also observed in the kinematically unfittable channels $\Lambda\pi^+\pi^-$ + several π^o's. Cuts of three standard deviations and at − 0.5 to 0.08 Gev^2 were applied to the missing mass squared when selecting $\Lambda\pi^+\pi^-\pi^+\pi^-\pi^0$ events.

The $Y_1^{*-}(1385)$ peak in $\Lambda\pi^+\pi^-\pi^+\pi^-$ is only about two standard deviation above phase space, in contrast to the $Y_1^{*+}(1385)$ which is more than four standard deviations above phase space (Fig. 5.22). The production angular distributions of $\Lambda\pi^+$ and $\Lambda\pi^-$ for the Y_1^* regions and for background regions have been subtracted to give production angular distributions of the Y_1^*'s. (The Y_1^* region has been taken as 1.34 to 1.43 Gev, about twice the natural width, and the background regions have been taken as 1.275 to 1.32 and 1.45 to 1.495 Gev, leaving gaps of about one half the resonance width to avoid having too much of the resonance tail in the background.)

The process of background subtraction is dangerous for two reasons:-

(a) It is difficult to be sure that the correct amount of background has been subtracted, especially in this case where the phase space is changing rapidly.

(b) The errors on the background subtracted plot are large - they are in fact given by the square root of the sum of the resonance region and background contributions to any bin.

In spite of this, there seems to be a real difference between the Y_1^{*+} and Y_1^{*-} production angular distributions (Fig. 5.23). As expected, the Y_1^{*+} has a strong backward peak, but surprisingly, appears to have a small forward peak as well. This forward peak could, however, be the result of insufficient background subtraction. The Y_1^{*-} is also peaked backwards and has no significant forward peak.

There is no other hyperon resonance produced in this final state.

Turning to the final state $\Lambda\pi^+\pi^-\pi^+\pi^-\pi^0$, we see that both $Y_1^{*+}(1385)$ and $Y_1^{*-}(1385)$ are strongly produced (Fig. 5.24). The effective mass distributions of $\Lambda\pi^+\pi^-$ when either $\Lambda\pi^+$ or $\Lambda\pi^-$ lies in the $Y_1^*(1385)$ region show a peak at about 1650 Mev (Fig. 5.25). The corresponding $\Lambda\pi^+\pi^-$ background subtracted histogram (obtained by taking either the $\Lambda\pi^+$ or $\Lambda\pi^-$ in a background region as defined previously) indicate that the majority, if not all, of the $Y_1^{*-}(1385)$ is associated with the $\Lambda\pi^+\pi^-$ peak at 1650 Mev. This is not so for the $Y_1^{*+}(1385)$. The production angular distributions of the Y_1^*'s are almost flat; in other words, they do not show peripheral characteristics (Fig. 5.26). Likewise, the production angular distributions of the $Y_1^{*\pm}\pi^{\mp}$ in the region 1.6 to 1.725 Gev do not have a peripheral character (Fig. 5.27). As we would normally expect a neutral hyperon resonance to be produced in a peripheral interaction, or at least to show some peripheral characteristics, the reason for this $Y_1^*\pi$ peak is rather obscure. In any case, a resonance decaying to $Y_1^*(1385)\pi$ should also decay to $\Sigma^{\pm}\pi^{\mp}$ and there is no evidence for a corresponding peak in $\Sigma^{\pm}\pi^{\mp}\pi^+\pi^-\pi^0$ as was pointed out in section 5.2. The decay angular distributions of the peak are flat, so give little additional information.

An alternative possibility is that the peak is produced by some kinematic effect. A plot of $\Lambda\pi^+$ against $\Lambda\pi^-$ effective mass for events in the region of the peak (1.6 to 1.725 Gev) shows that the two Y_1^* bands overlap and that the majority of the Y_1^* events come from the overlap region (Fig. 5.28); but such an effect would occur anyway if a resonance of mass 1650 Mev decayed to $Y_1^*(1385)\pi$, because of the restricted phase space for the decay. We must therefore leave the interpretation of this peak open.

The $\pi^+\pi^-\pi^0$ effective mass spectrum shows strong ω production (Fig. 5.29), little of which is associated with the Y_1^{*+} (Fig. 5.30), none with the Y_1^{*-} and none with the 1650 peak. The production and decay angular distributions of the ω are essentially flat, and give the following spin density matrix elements:

$\rho_{11} = 0.32 \pm 0.04$; $\rho_{1\,-1} = -0.09 \pm 0.07$; Re $\rho_{10} = -0.06 \pm 0.06$

(calculated from the background subtracted plots).

TABLE 5

Final State	Observed Number of Events	Correction Factor	Cross-Section (μb)
Ξ^-K^+	6	2.82	1.9 ± 0.8
$\Xi^-K^+\pi^0$	10	2.57	2.9 ± 0.9
$\Xi^-\pi^+K^0$	17	2.29	4.3 ± 1.1
$\Xi^-K^+\pi^+\pi^-$	21	2.82	7 ± 2
$\Xi^-\pi^+K^0\pi^0$	24	5.14	14 ± 3
$\Xi^-K^+\pi^+\pi^-\pi^0$	39	2.57	11 ± 2
$\Xi^-\pi^+\pi^-\pi^+K^0$	22	2.29	6 ± 1.2
$\Xi^-K^+\pi^+\pi^-\pi^+\pi^-$	6	2.82	4.5 ± 1.9
$\Xi^-\pi^+\pi^-\pi^+K^0\pi^0$	8	5.14	4.6 ± 1.9
$\Xi^-K^+\pi^-\pi^+\pi^-\pi^+\pi^0$	3	2.57	2.1 ± 1.2
$\Xi^-\pi^+\pi^-\pi^+\pi^-\pi^+K^0$	1	2.29	0.6 ± 0.6
1) Total Ξ^-	238	2.67	87 ± 9
$\Sigma^-\pi^+\pi^-\pi^+$	121	1.58	51 ± 6
$\Sigma^+\pi^-\pi^+\pi^-$	95	3.56	90 ± 12
2) $Y_0^*(1405)\pi^+\pi^-$	14	2.20	8.2 ± 4.2
2) $Y_0^*(1520)\pi^+\pi^-$	19	2.20	11 ± 4
$\Sigma^-\pi^+\pi^-\pi^+\pi^0$	296	1.54	122 ± 13
$\Sigma^+\pi^-\pi^+\pi^-\pi^0$	190	3.51	178 ± 20
2) $Y_0^*(1405)\pi^+\pi^-\pi^0$	36	2.16	21 ± 6
2) $Y_0^*(1520)\pi^+\pi^-\pi^0$	26	2.16	15 ± 5

continued over ...

TABLE 5 (continued)

Final State	Observed Number of Events	Correction Factor	Cross-Section (μb)
$\Sigma^-\pi^+\omega$	28	1.54	12 ± 4
$\Sigma^+\pi^-\omega$	25	3.51	23 ± 8
$\Lambda\pi^+\pi^-\pi^+\pi^-$	160	1.98	65 ± 8
$Y^{*+}(1385)\pi^+\pi^-\pi^-$	40	1.98	16 ± 4
$Y^{*-}(1385)\pi^+\pi^+\pi^-$	12	1.98	5 ± 2.5
$\Lambda\pi^+\pi^-\pi^+\pi^-\pi^\circ$	802	1.95	320 ± 30
$Y^{*+}(1385)\pi^+\pi^-\pi^-\pi^\circ$	108	1.95	43 ± 9
$Y^{*-}(1385)\pi^+\pi^-\pi^+\pi^\circ$	70	1.95	28 ± 6
$(Y^{*\pm}(1385)\pi^\mp)(1650)\pi^+\pi^-\pi^\circ$	80	1.95	32 ± 7
$\Lambda\pi^+\pi^-\omega$	160	1.95	64 ± 11

Footnotes:

1) From events with Ξ^- decays in which the Λ is seen.

2) $\Sigma^\pm\pi^\mp$ decay modes only of Y^*_0's.

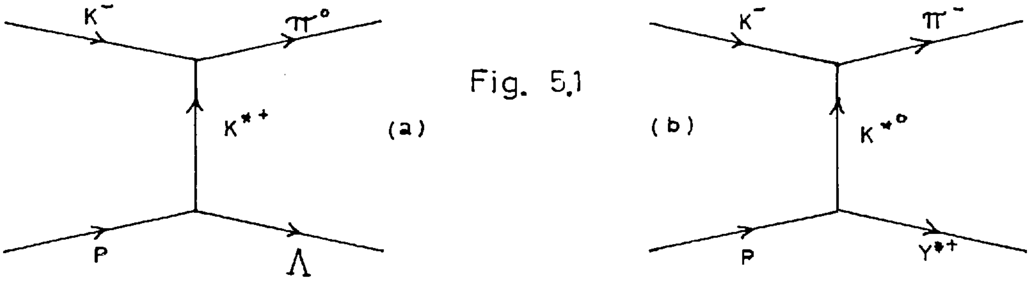

Fig. 5.1

(a) (b)

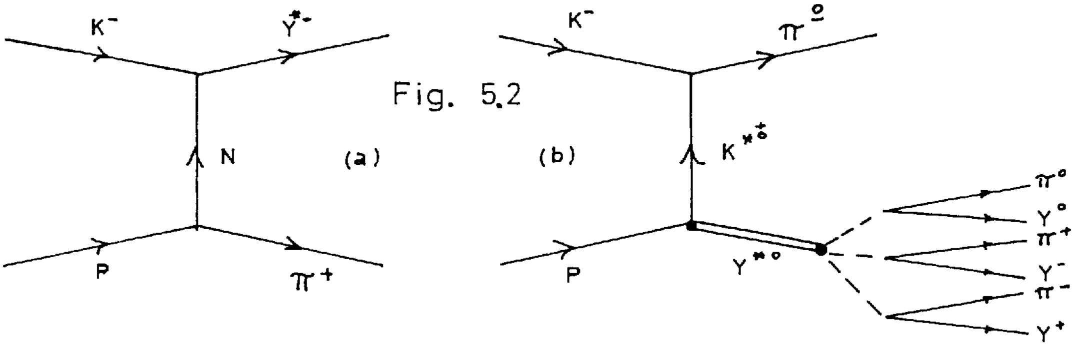

Fig. 5.2

(a) (b)

Fig. 5.3

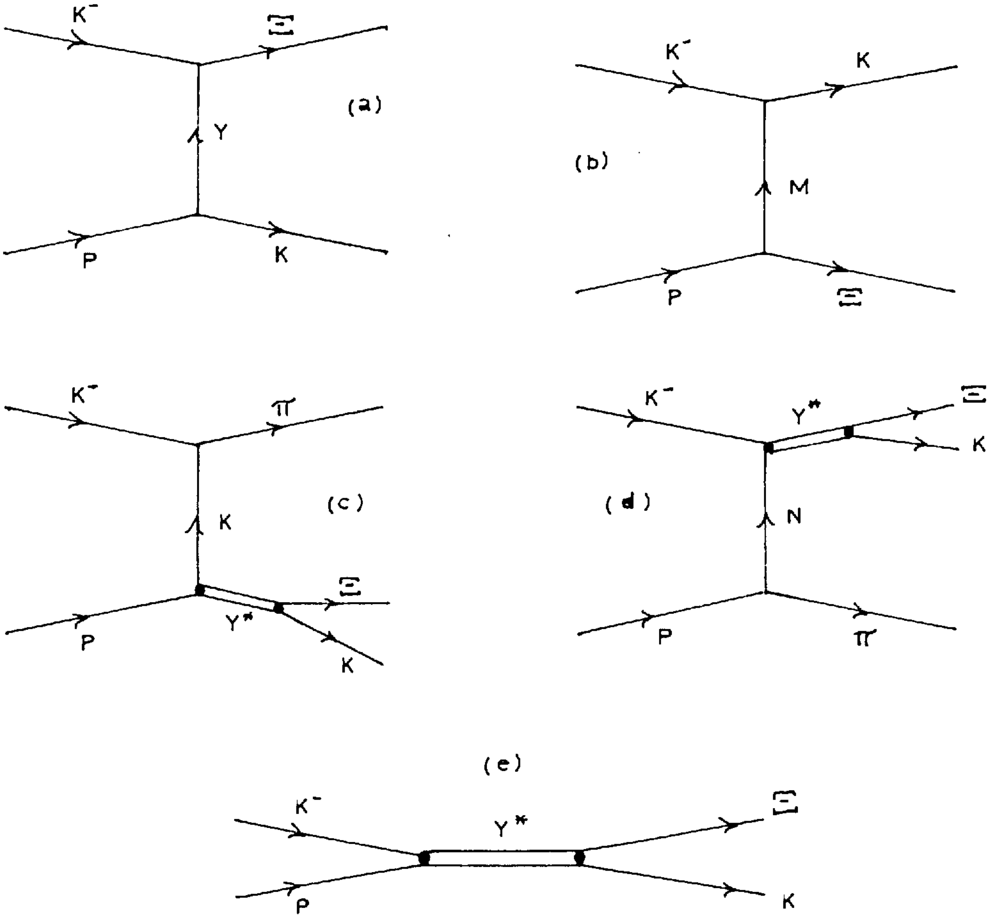

(a) (b) (c) (d) (e)

Fig. 5.4

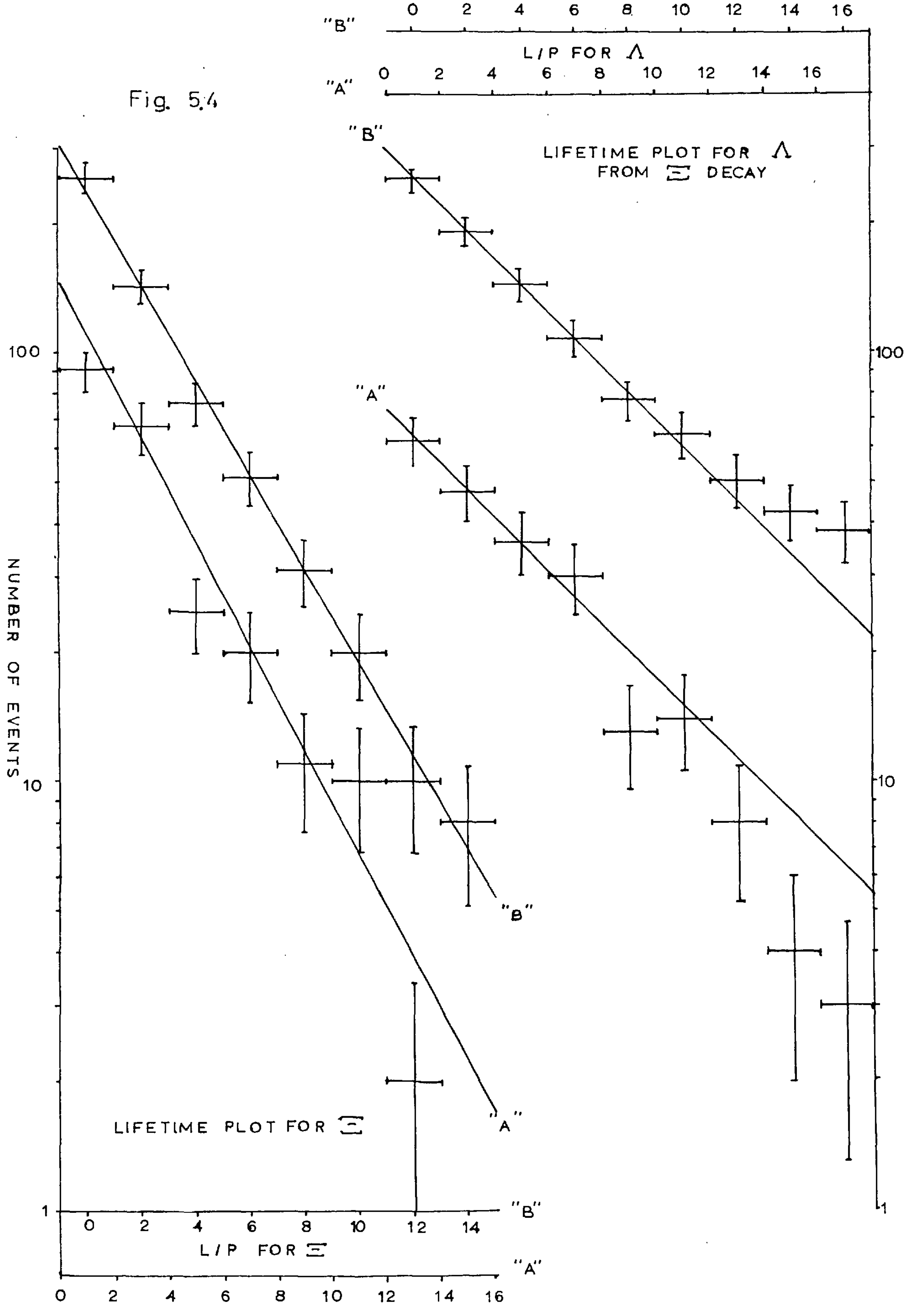
"B"
0 2 4 6 8 10 12 14 16
L/P FOR Λ
"A"
0 2 4 6 8 10 12 14 16
LIFETIME PLOT FOR Λ FROM Ξ DECAY
"B"
"A"
NUMBER OF EVENTS
100
10
1
"B"
"A"
LIFETIME PLOT FOR Ξ
"B"
0 2 4 6 8 10 12 14
L/P FOR Ξ
"A"
0 2 4 6 8 10 12 14 16

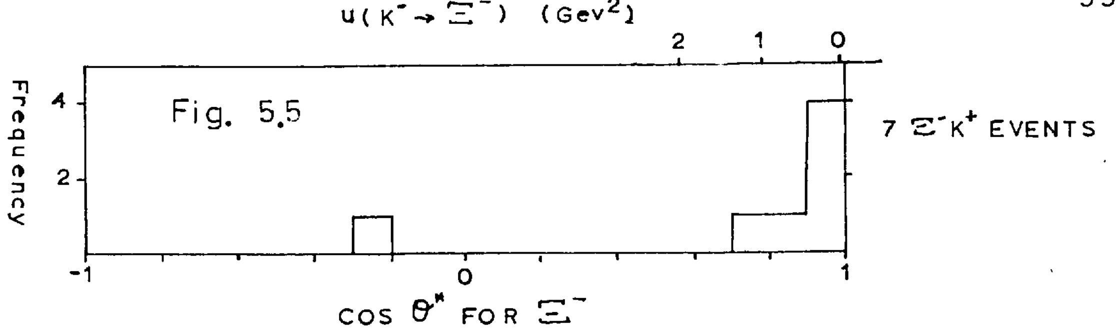
Fig. 5.5
u(K⁻ → Ξ⁻) (Gev²)
2
1
0
Frequency
4
2
7 Ξ⁻K⁺ EVENTS
-1
0
1
cos θ* FOR Ξ⁻

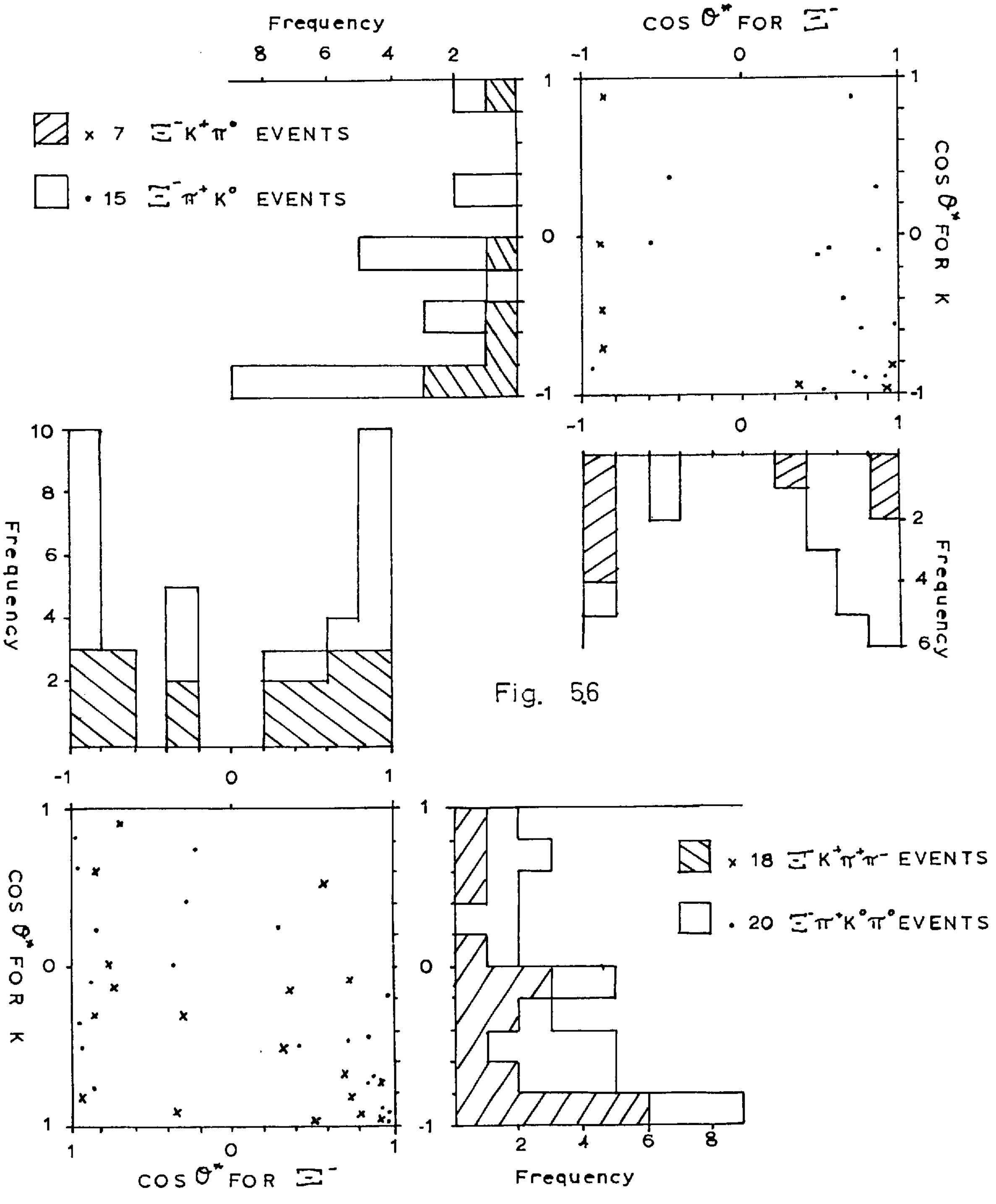
Fig. 5.6
Frequency
8
6
4
2
cos θ* FOR Ξ⁻
-1
0
1
× 7 Ξ⁻K⁺π⁰ EVENTS
• 15 Ξ⁻π⁺K⁰ EVENTS
cos θ* FOR K
Frequency
10
8
6
4
2
× 18 Ξ⁻K⁺π⁺π⁻ EVENTS
• 20 Ξ⁻π⁺K⁰π⁰ EVENTS
cos θ* FOR K
cos θ* FOR Ξ⁻
Frequency

Fig. 5.7

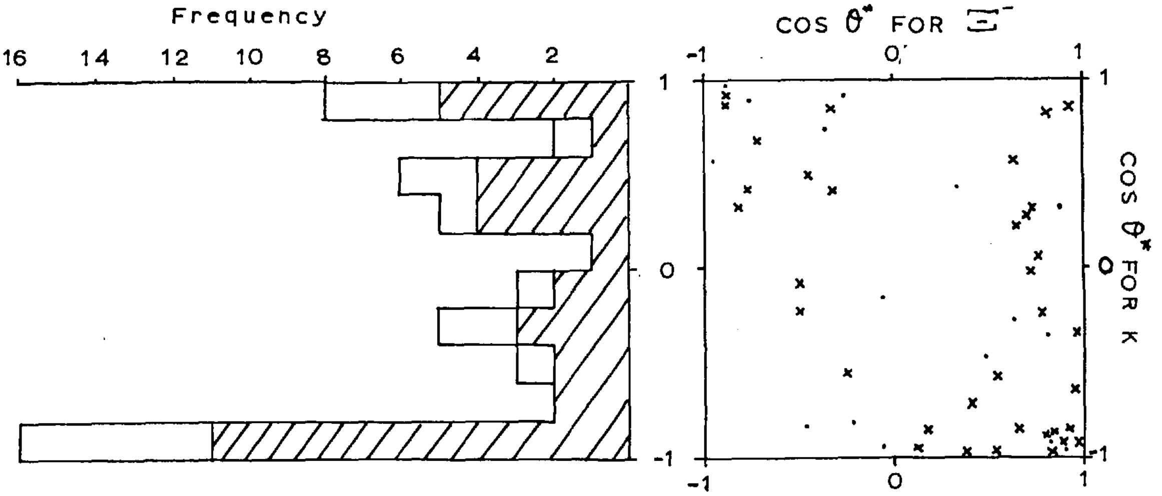

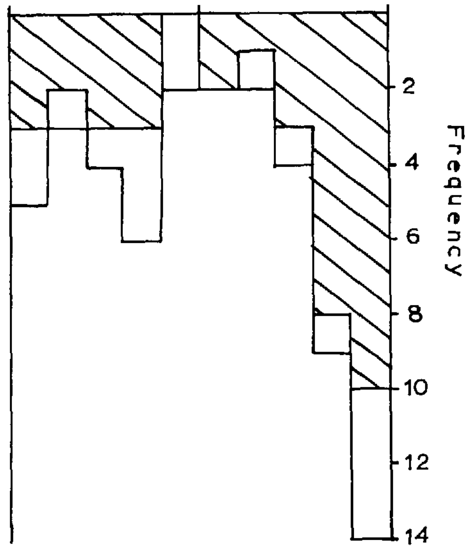

× ▧ 35 Ξ⁻K⁺π⁺π⁻π⁰ EVENTS

. ☐ 16 Ξ⁻π⁺π⁺π⁻ K⁰ EVENTS

☐ 411 TOPOLOGY EVENTS

Fig. 5.8

▨ 211 TOPOLOGY EVENTS

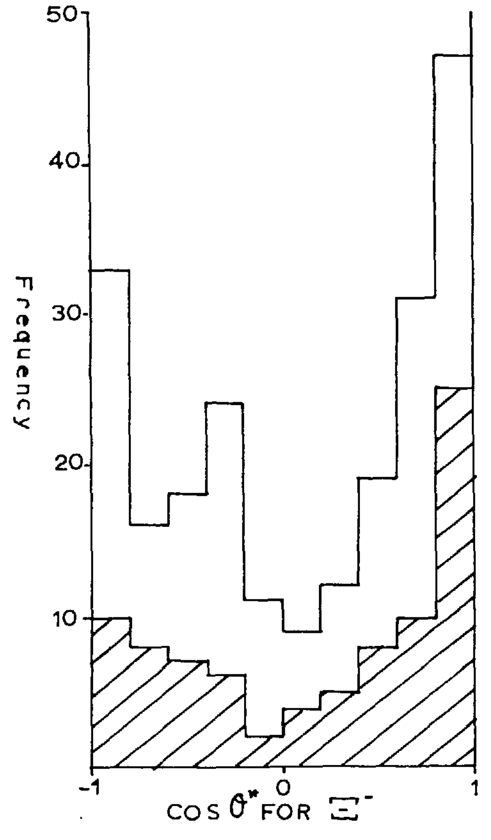

Fig. 5.9

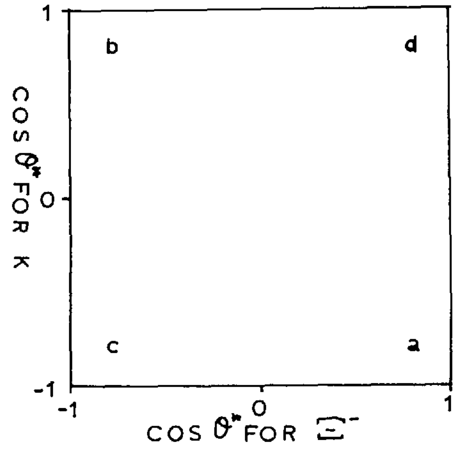

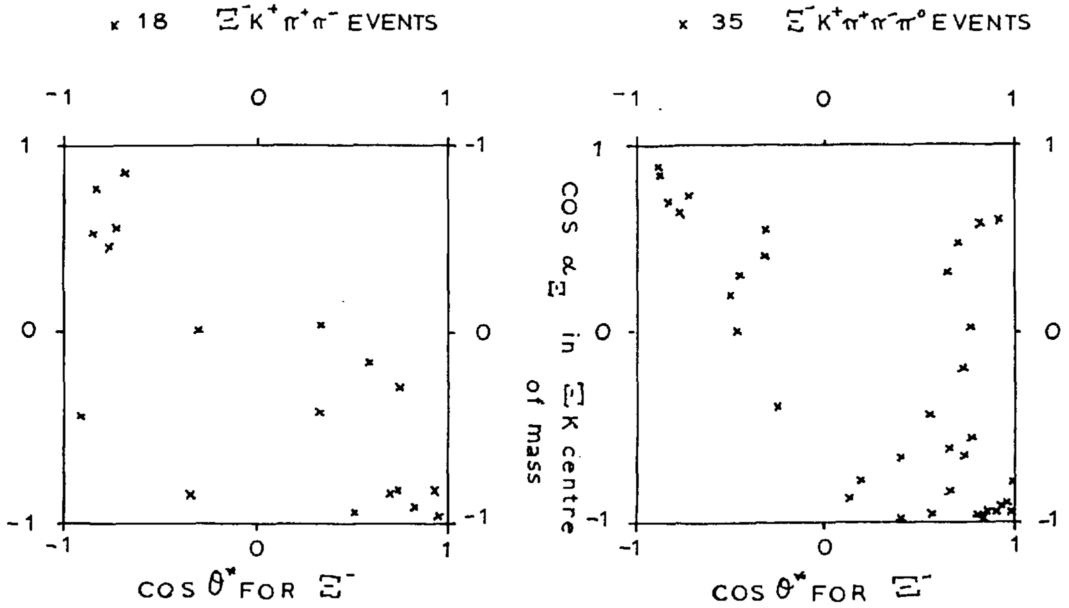

Fig. 5.10

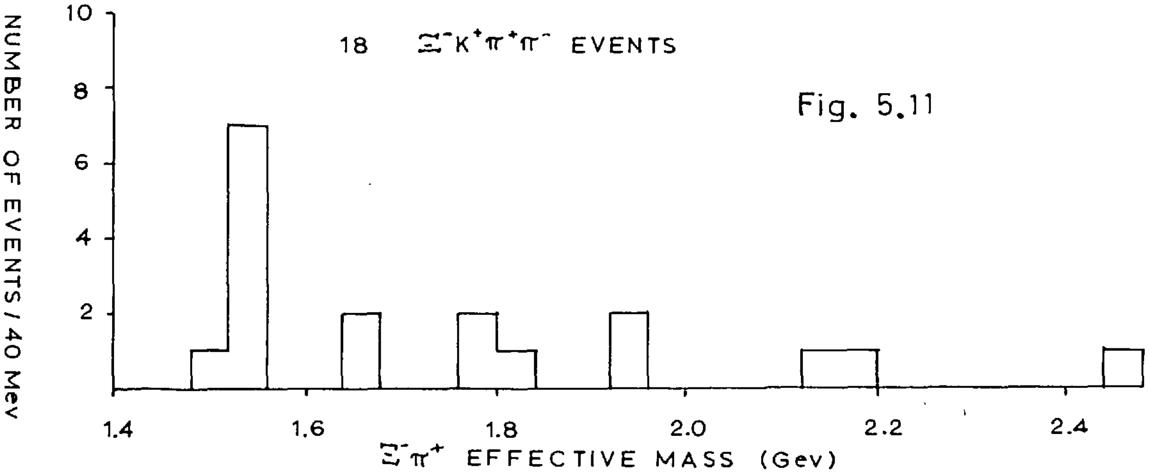

Fig. 5.11

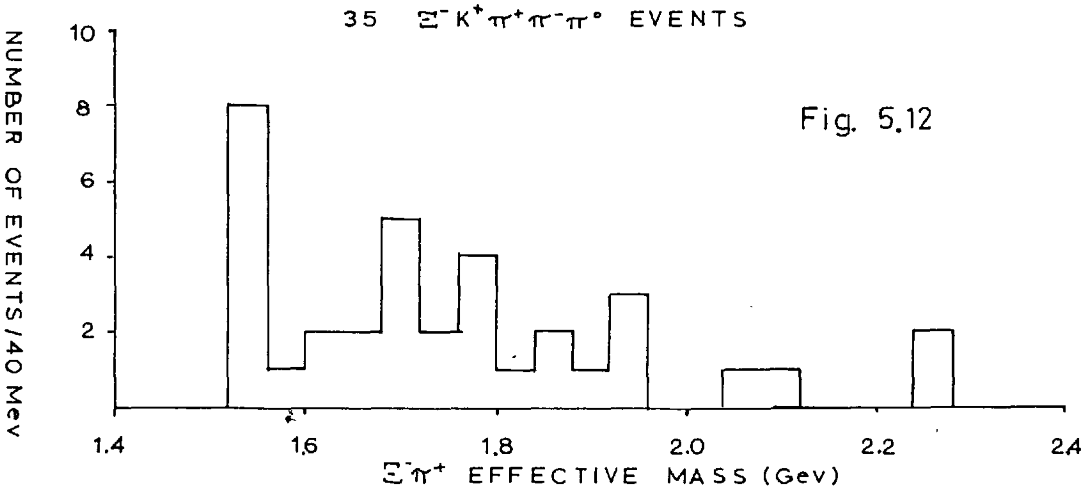

Fig. 5.12

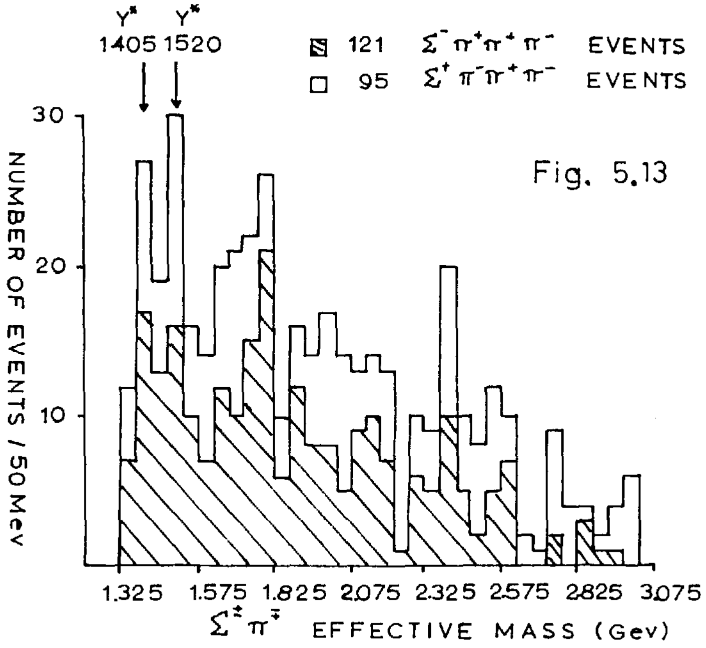

Fig. 5.13

Fig. 5.14

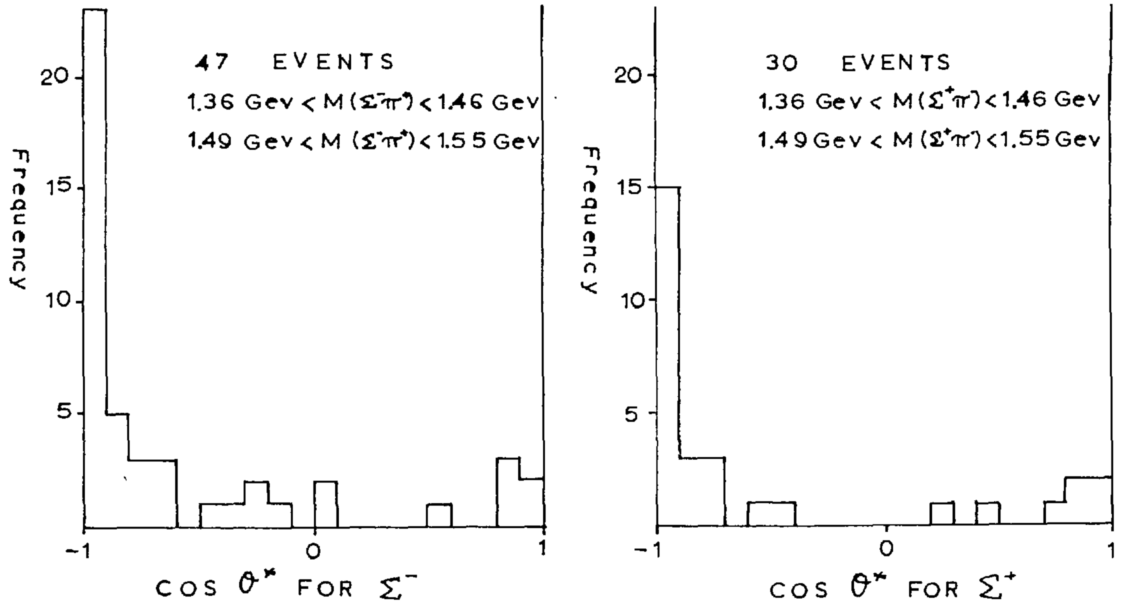

Fig. 5.15

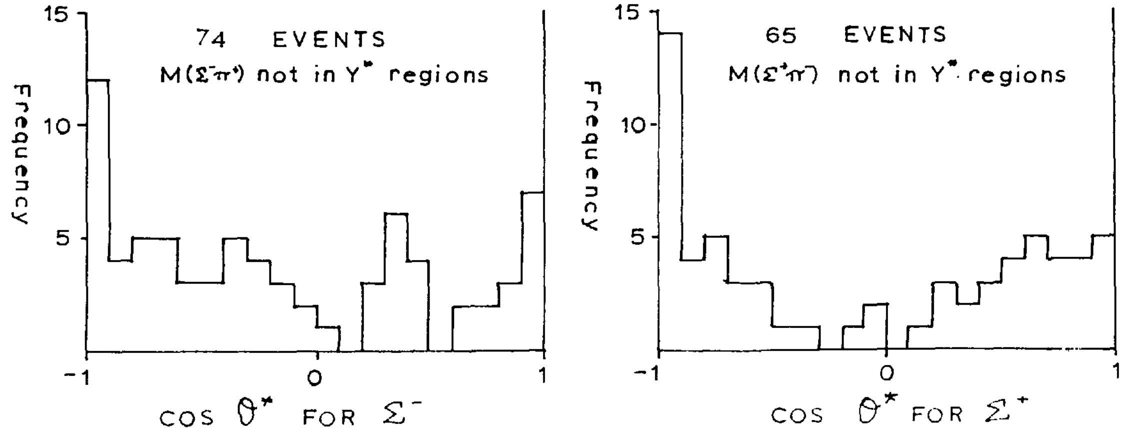

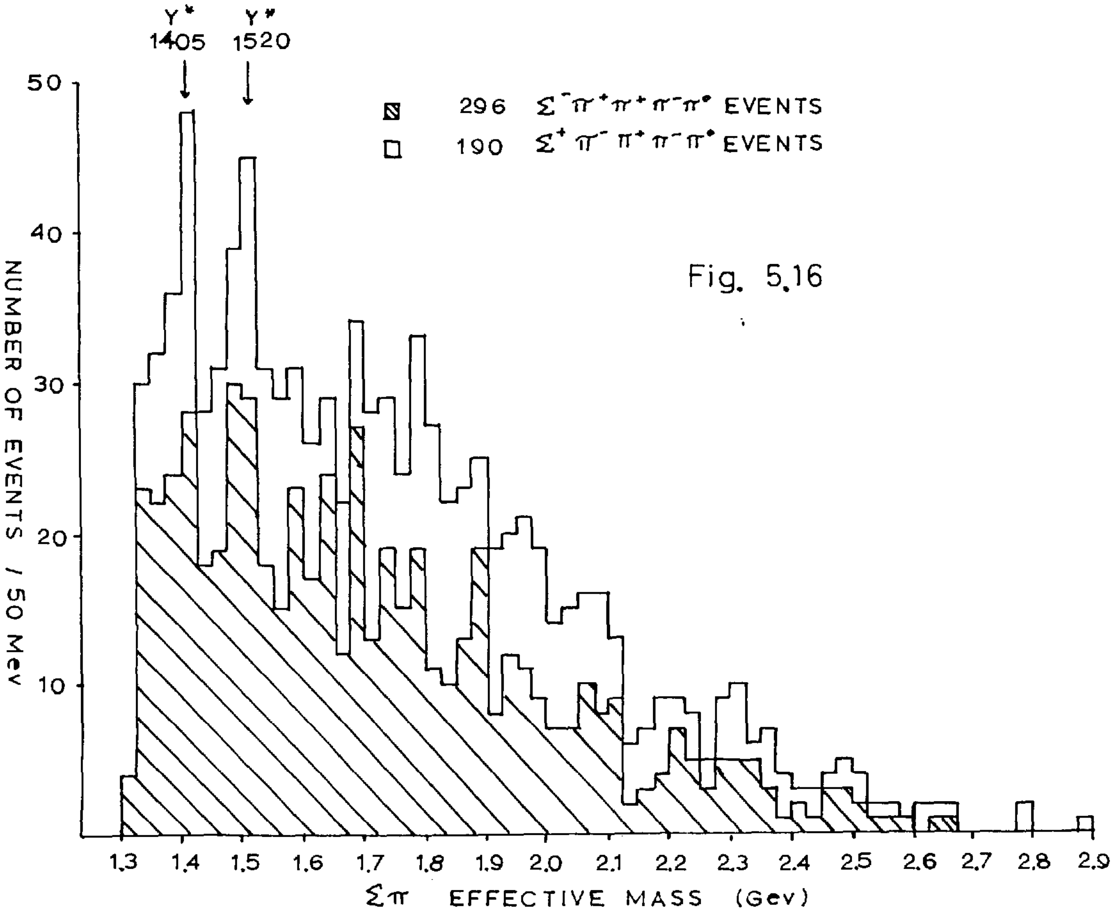

Fig. 5.16

Fig. 5.17

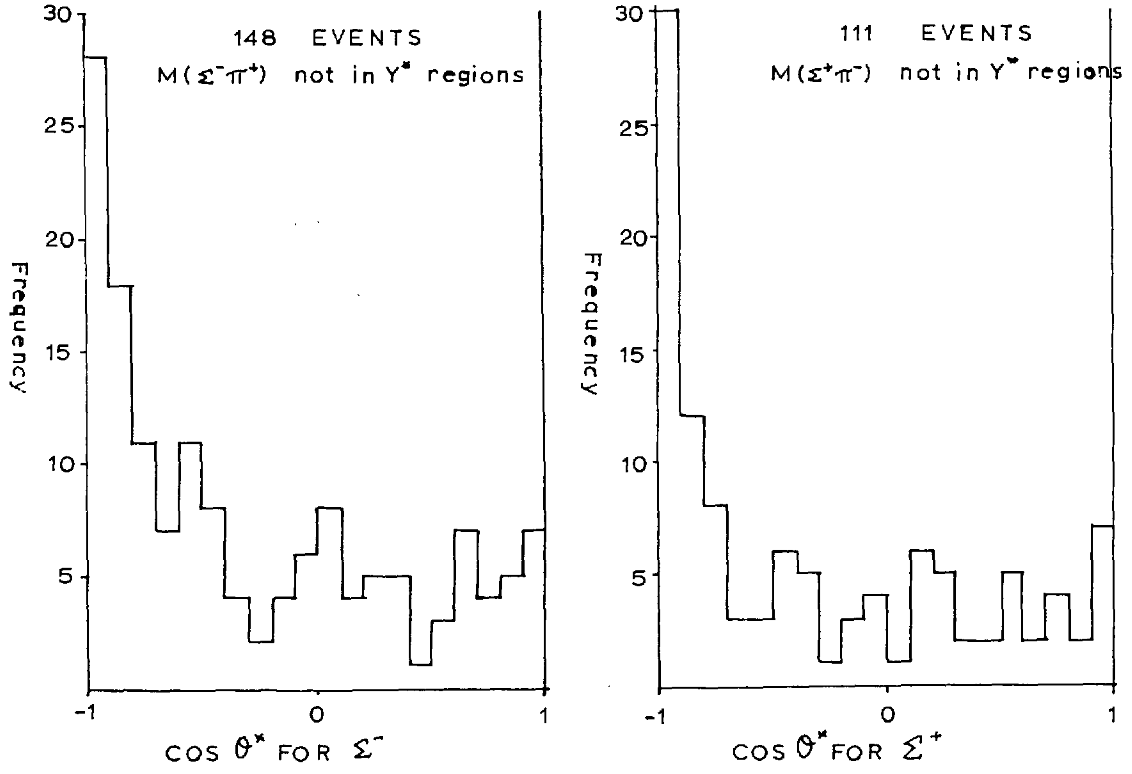

Fig. 5.18

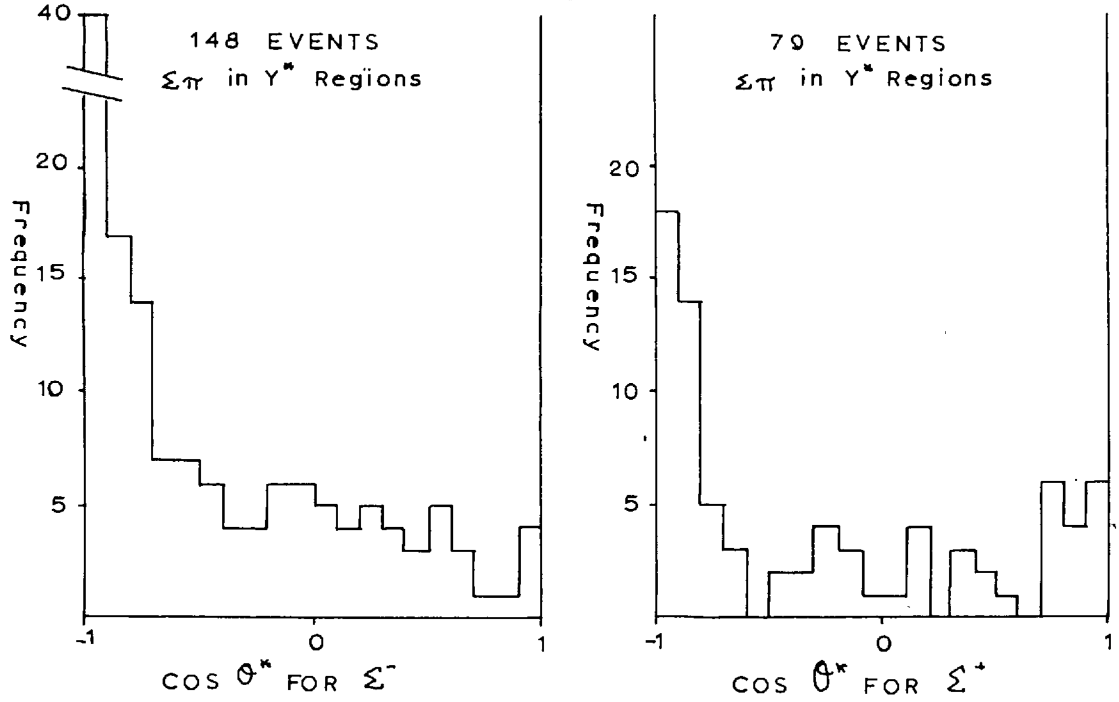

Fig. 5.19

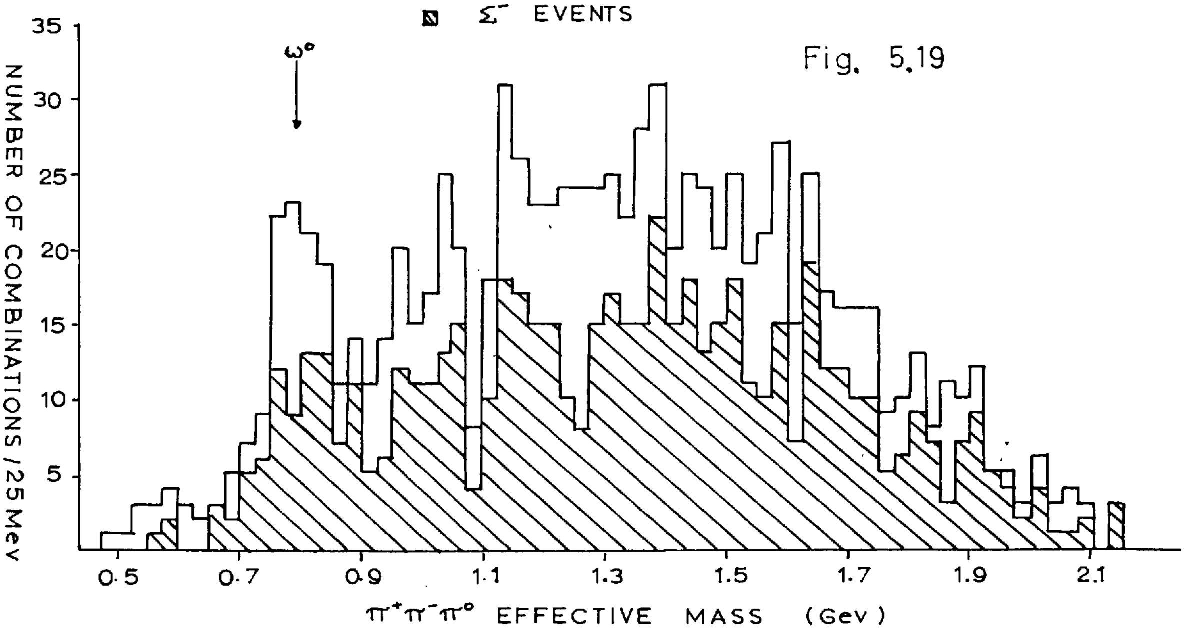

Fig. 5.20

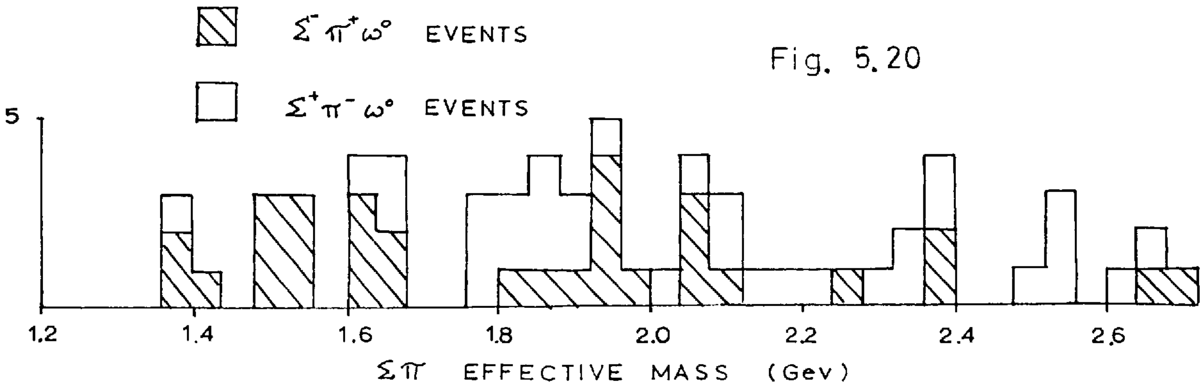

Fig. 5.21

ANGULAR DISTRIBUTIONS FOR $\Sigma\pi'\omega$ EVENTS

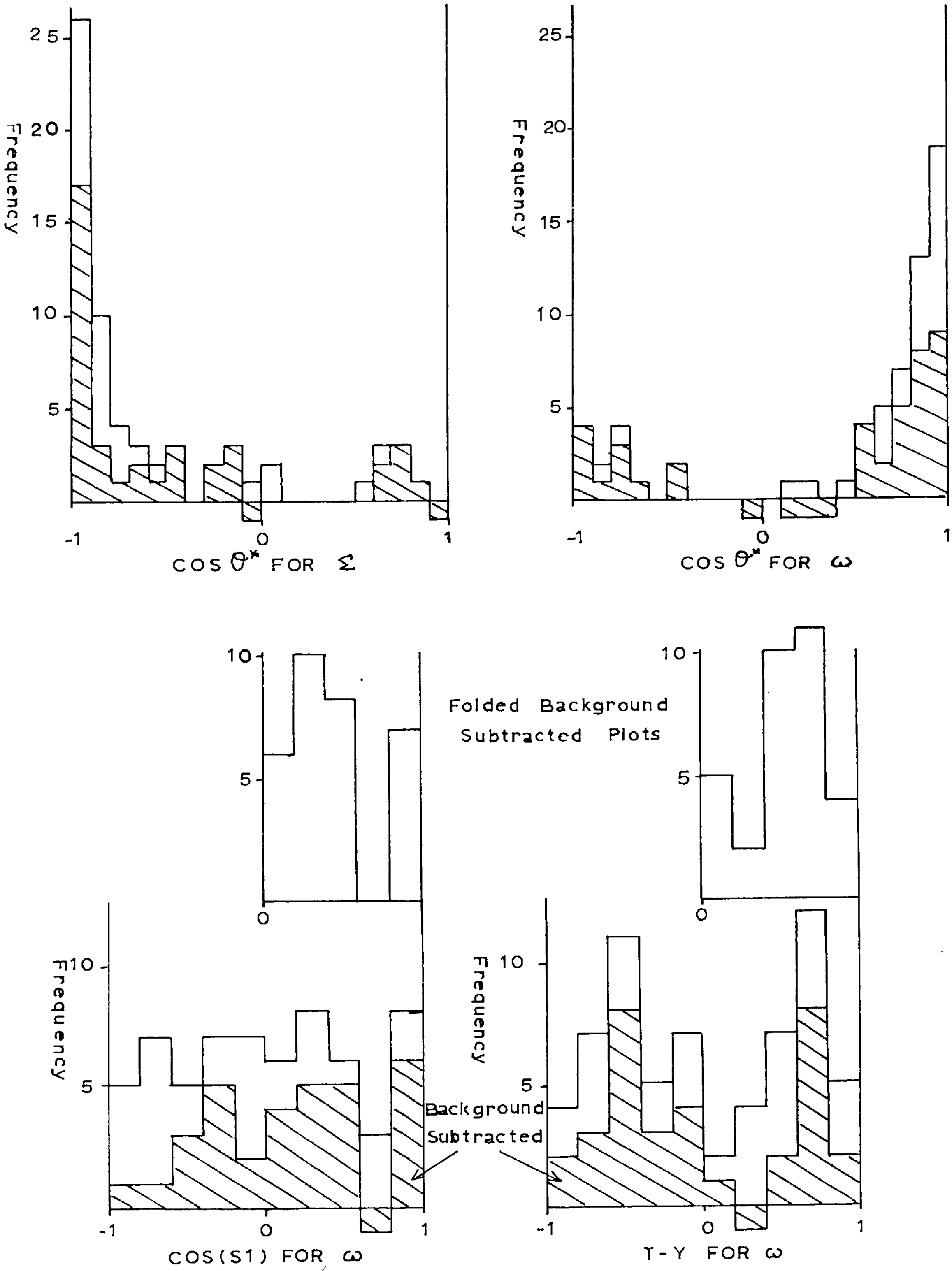

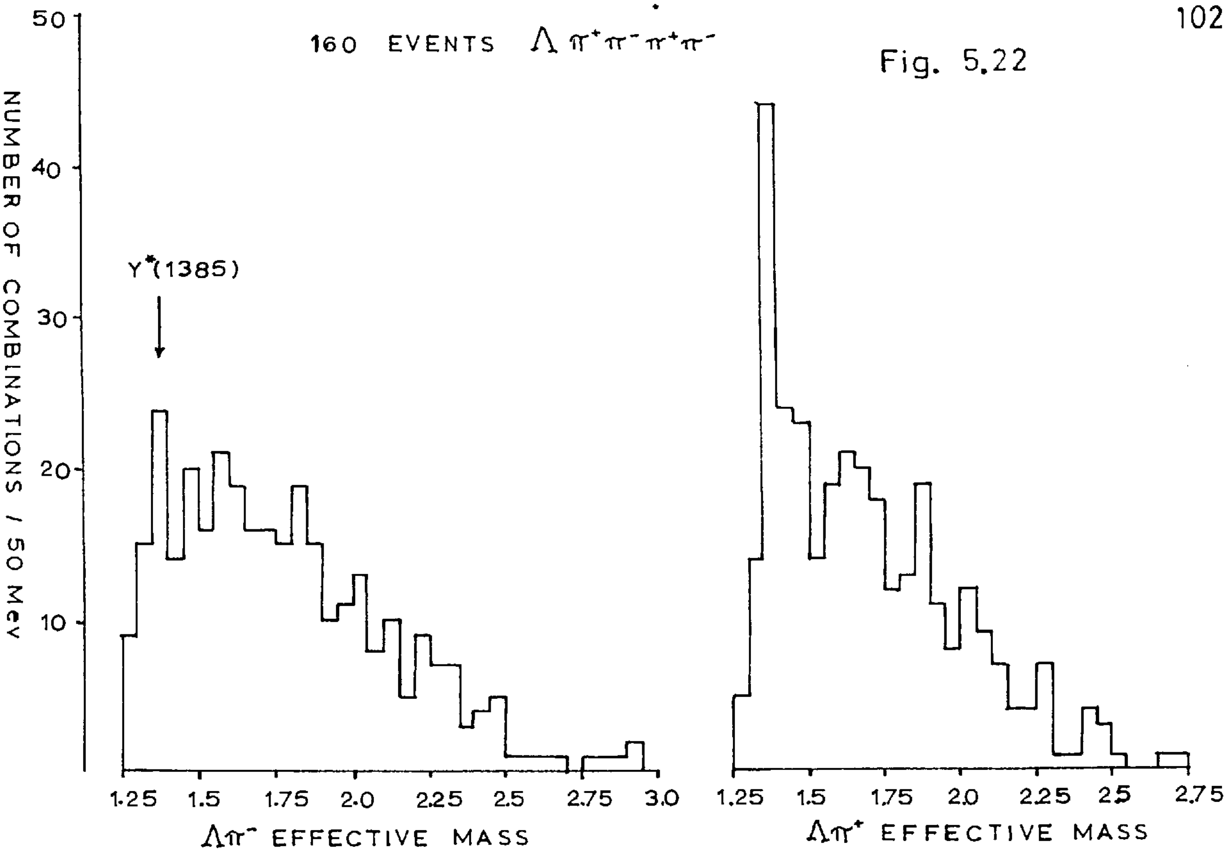

Fig. 5.22

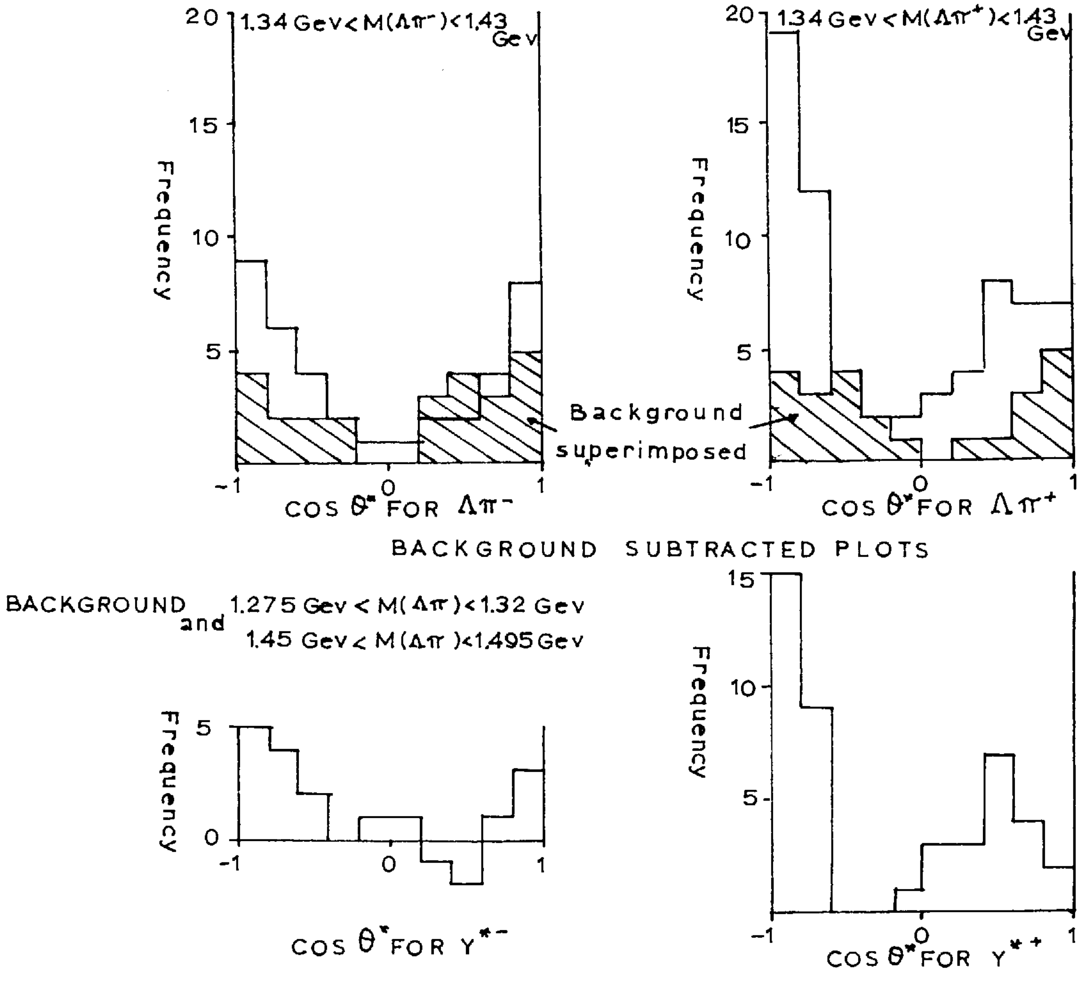

Fig. 5.23

802 EVENTS $\Lambda\pi^+\pi^-\pi^+\pi^-\pi^0$

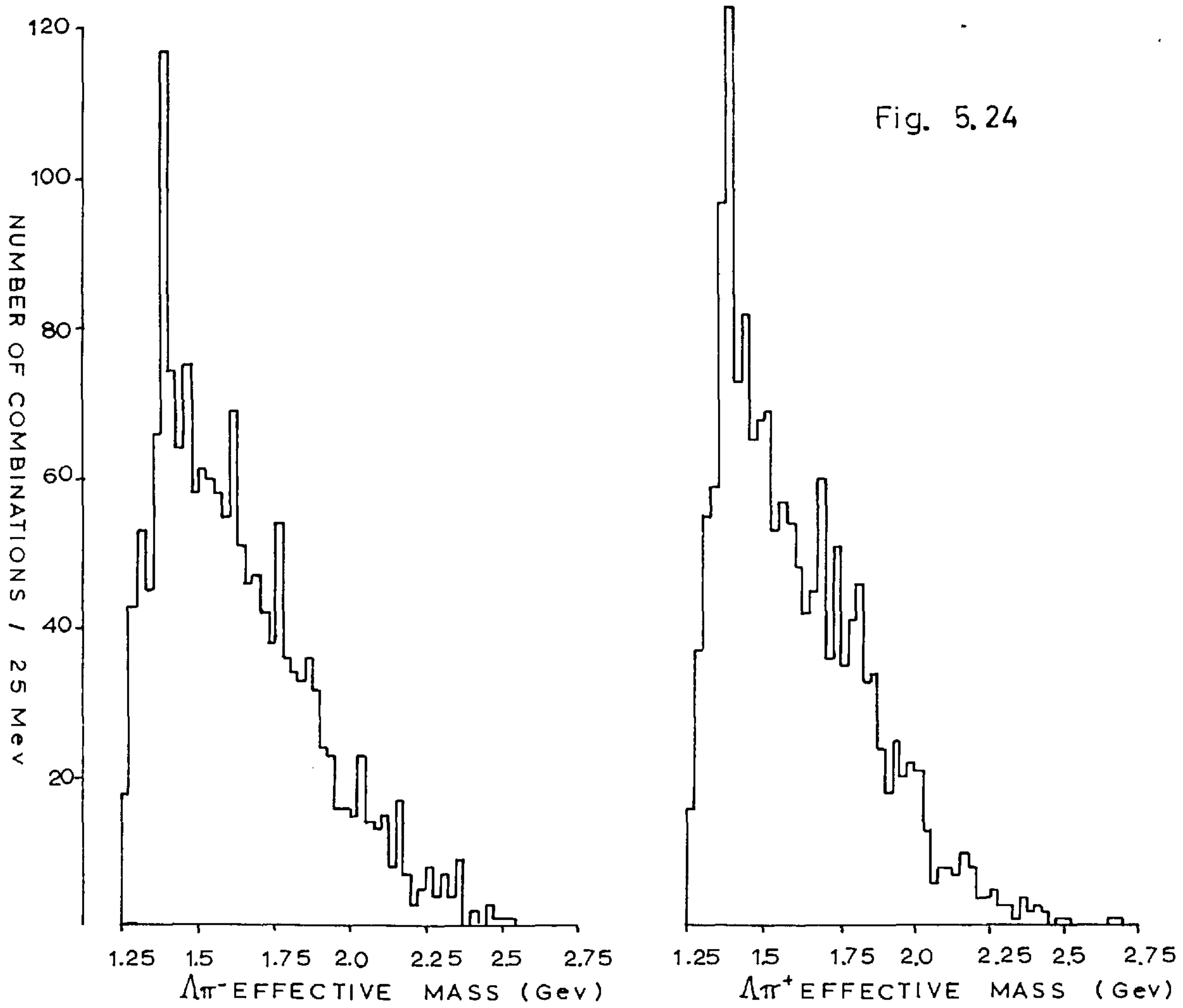

Fig. 5.24

Fig. 5.25

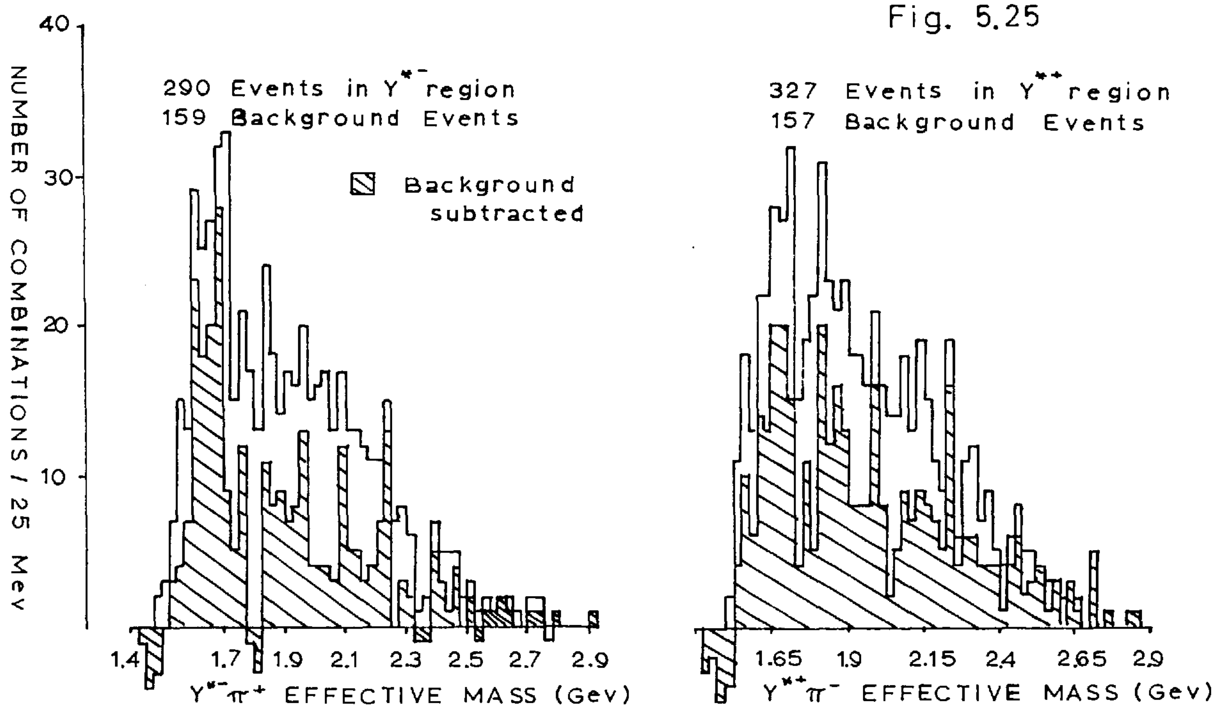

Fig. 5.26

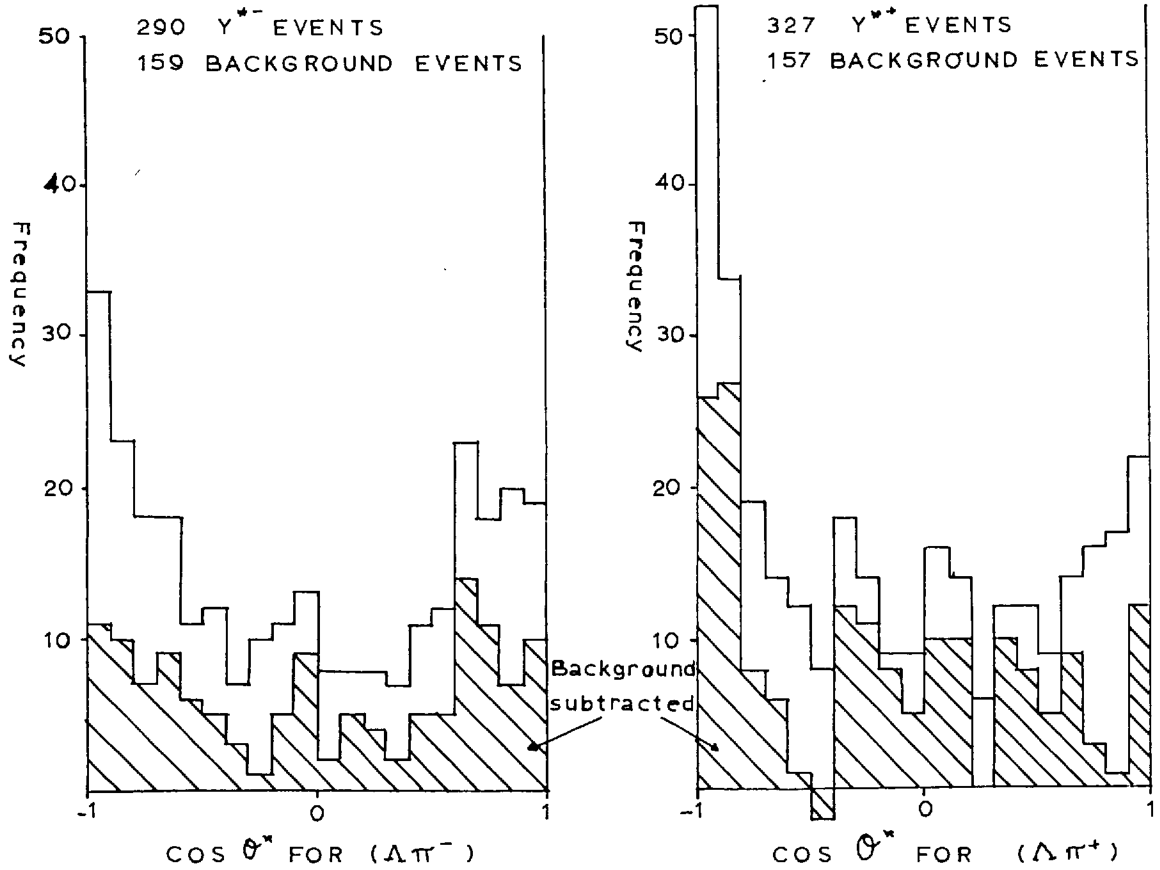

Fig. 5.27

1.6 Gev < M($\Lambda\pi^+\pi^-$) < 1.725 Gev

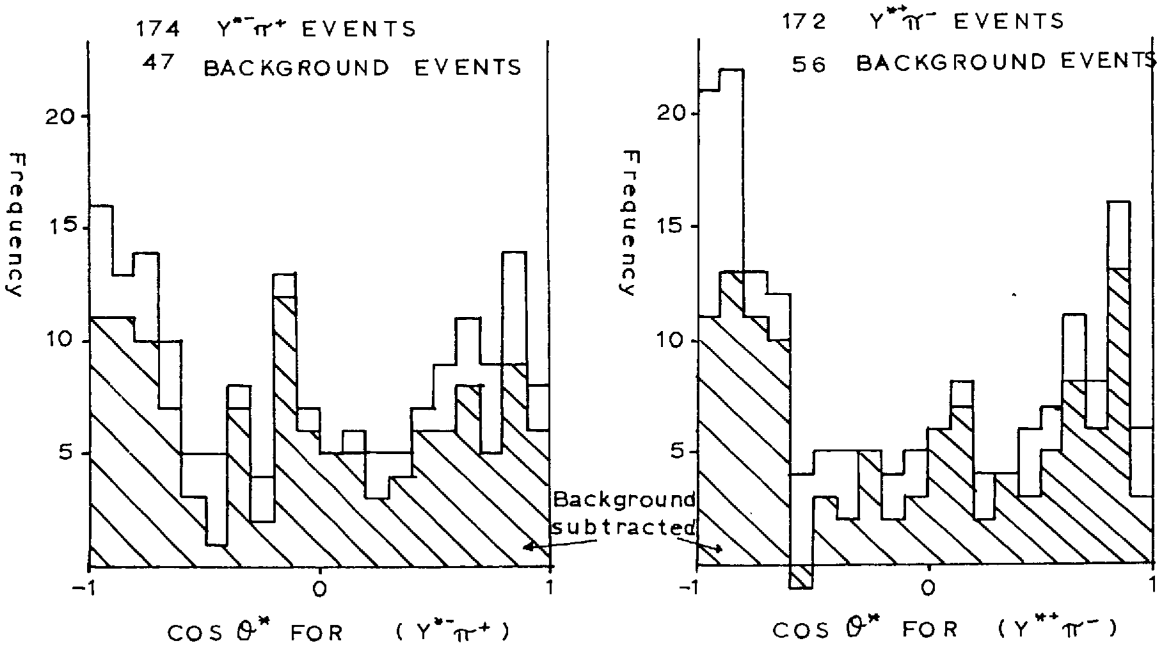

Fig. 5.28

253 EVENTS WITH $1.6 < M(\Lambda\pi^+\pi^-) < 1.725$

FROM $\Lambda\pi^+\pi^-\pi^+\pi^-\pi^0$

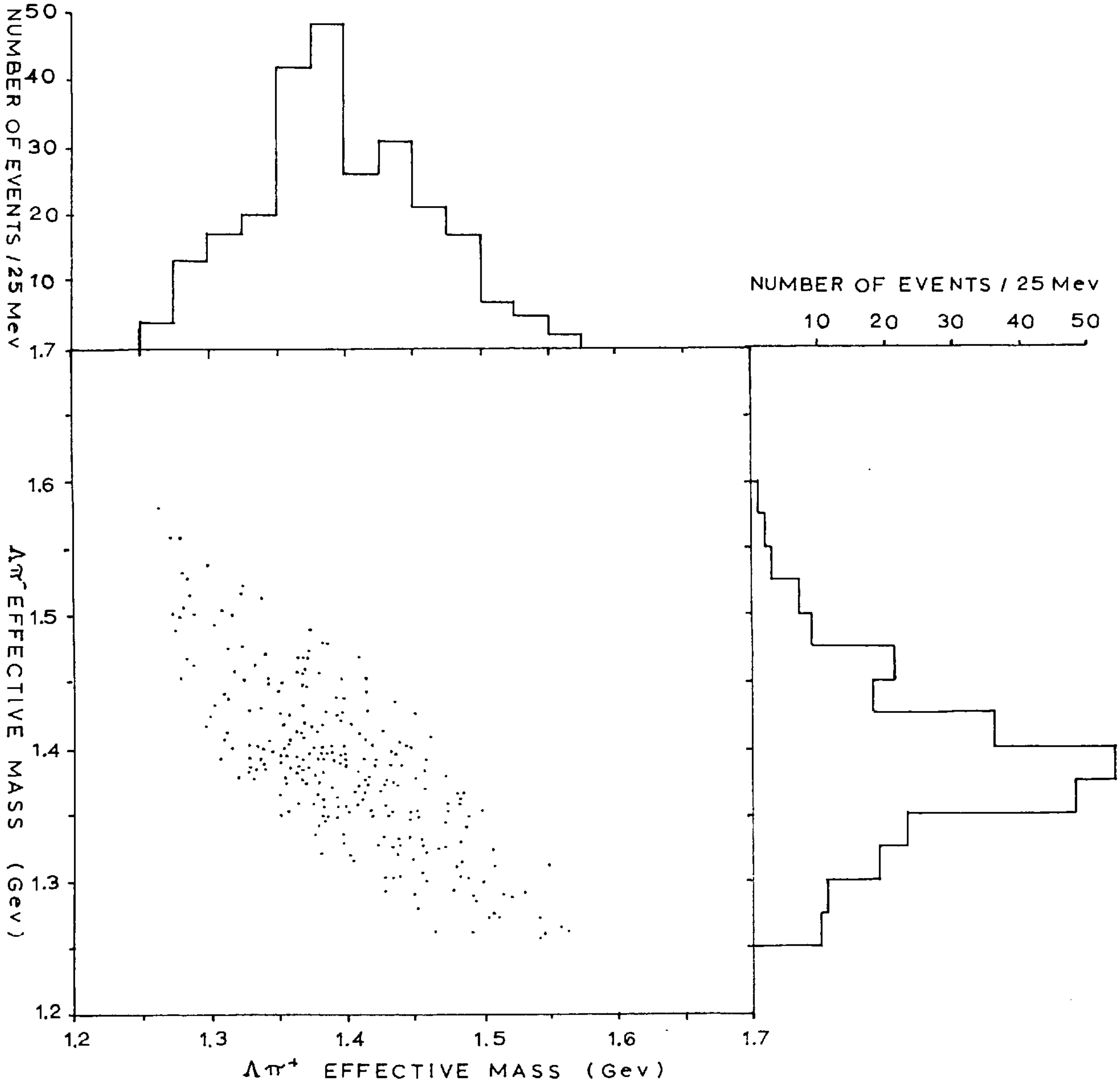

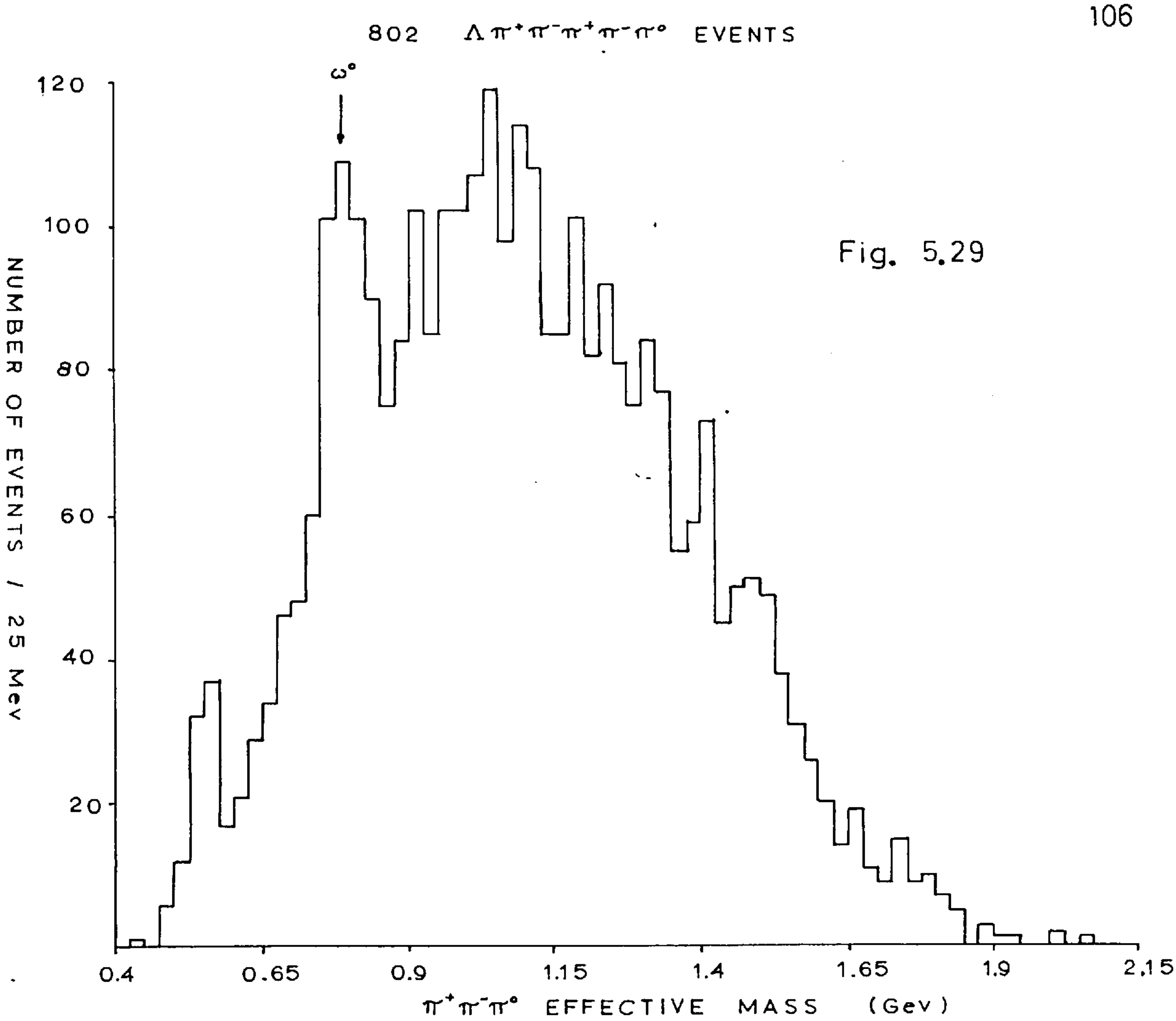

Fig. 5.29

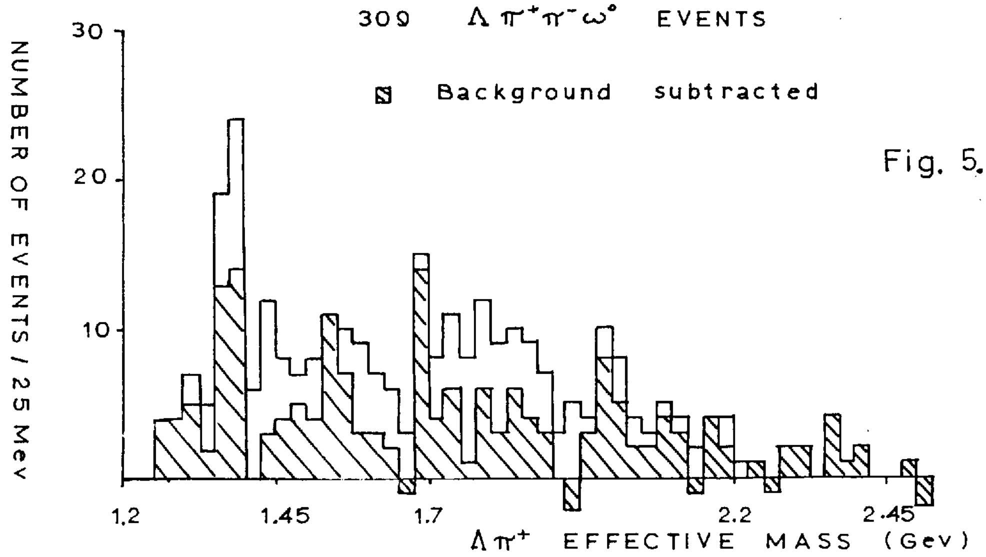

Fig. 5.30

309 $\Lambda\pi^+\pi^-\omega$ EVENTS; 171 after background subtraction

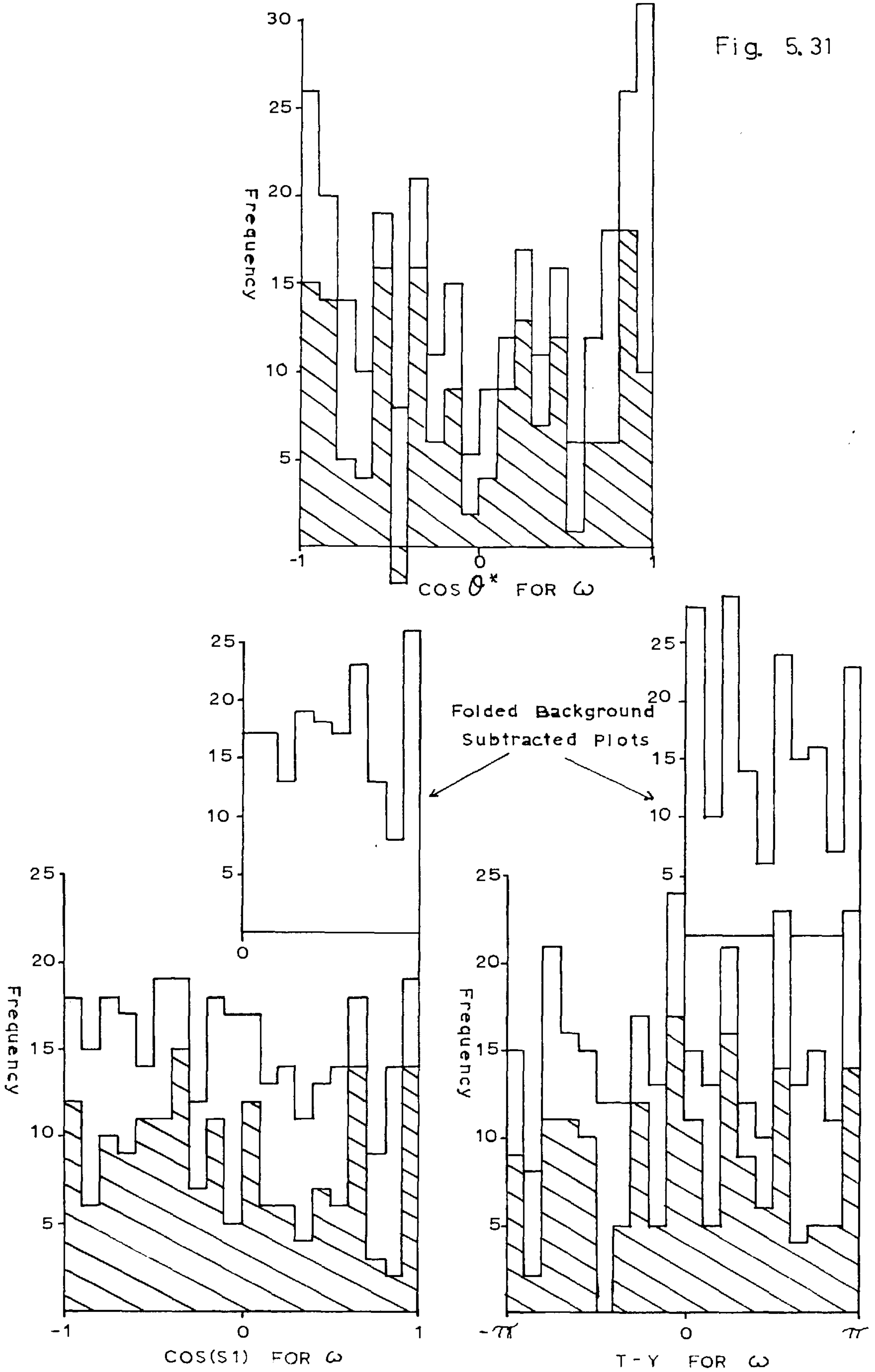

Fig. 5.31

CHAPTER SIX

DISCUSSION

Some of the data obtained in this experiment has been examined in the previous two chapters, and it is the purpose of this one to place the results obtained in their context with other experiments (at lower energies) and with present theoretical ideas.

At the moment, detailed theoretical analysis of production mechanisms has been essentially restricted to two body channels. The methods used have nearly all been based on the peripheral model modified by a variety of procedures to make it give a better and more quantitative description of the experimental data. The three basic difficulties with the model are, first, that it does not predict differential cross-sections that fall as quickly as experimental ones with increasing t. Secondly, that it violates unitarity - it gives cross-sections several orders of magnitude too large - and thirdly, that when the exchange of a particle with spin j is considered, the Born amplitude diverges as s^j. To overcome this last difficulty the Regge pole model(32) was formulated; j is replaced by the Regge "trajectory", $\alpha(t)$, with $\alpha(-m^2) = j$, m being the mass of the exchanged particle, and the real part of α decreases as t increases. The factor s^j is then replaced by $s^{\alpha(t)}$, which increases more slowly than s^j for all physical values of t. The functions $\alpha(t)$ are usually taken as straight lines, though there is no 'a priori' reason for doing so. There is, however, ample experimental evidence to indicate that, provided one believes in the Regge model, the $\alpha(t)$ are straight lines. (See for example the trajectories associated with the N^*'s(33) and the Regge pole model analysis of π^-p charge exchange scattering$^{(34)}$.)

A generalised extension of the peripheral model to many-body channels has been made by Amati et al.$^{(35)}$, and Joseph and Pilkuhn have performed specific calculations for some three body channels in πp interactions with some success$^{(26)}$. No similar calculations have been made for the three body channels elucidated in chapter four, so further remarks about them can only be of a rather general nature.

One of the most successful branches of theoretical high energy physics is the unitary symmetry classification of particles and resonances (witness its prediction of the existence of the Ω^-). The groups SU(3), SU(6) and its relativistic extensions have been used, not only to classify the particles according to their quantum numbers, but also to relate their masses and many of their coupling constants and to derive relations between cross-sections and between decay rates (see for example Reference 36). We shall use SU(3) to explain some of the properties of the φ meson (or rather we shall show that SU(3) is consistent with the observed behaviour of the φ).

6.1 The Production Properties of the φ Meson

The quantum numbers of the φ meson are now well established$^{(37)}$ as $IJ^{PG} = 01^{--}$, which are the same as those of the ω. Its production and decay properties are, however, significantly different from those of the ω and these differences may be ascribed to the different ways in which the φ and ω couple to other particles. Thus the behaviour of the φ can in several instances be explained by assuming that its coupling to non-strange mesons and baryons is small i.e. the coupling constants $G_{\varphi N\bar{N}}$ and $G_{\varphi\rho\pi}$ etc. $\rightarrow 0$. That this is so can be shown to be consistent with the representation of the φ in unitary symmetry.

Under SU(3) either the φ or the ω should be the isosinglet member of a vector meson octet and the other a unitary singlet. Unfortunately, neither particle has the mass expected for the isosinglet member of an octet. The Gell-Mann - Okubo mass formula(38) relating the masses of the members of an octet predicts that the isosinglet octet vector meson should have a mass $\sim$930 Mev. As the mass formula is in remarkable agreement with the masses of the pseudoscalar meson and baryon octets there appears no reason why it should not also work for the vector mesons. Sakurai therefore suggested(39) that the φ and ω might be mixed by the medium strong symmetry breaking interactions because they have the same quantum numbers. As a result of this mixing, the physical particles will not have the masses expected from the theory without mixing.

The physical states φ and ω can be expressed in terms of the pure SU(3) states ω_1 the unitary singlet, and ω_8 the octet member, by

$$\omega = \omega_1 \cos\theta + \omega_8 \sin\theta$$

$$\varphi = -\omega_1 \sin\theta + \omega_8 \cos\theta$$

where θ is the mixing angle. Using the physical particle masses and the Gell-Mann - Okubo prediction for the mass of ω_8, the angle θ is calculated by diagonalising the mass matrix(40). The result is $\theta \simeq 38^\circ$. The SU(3) representation of the vector mesons can now be rewritten in terms of the physical particles ω and φ rather than ω_1 and ω_8.

The vector meson octet is usually represented by(40)

$$(V_8)_i^{\ j} = \begin{pmatrix} \omega_8/\sqrt{6} + \rho^\circ/\sqrt{2} & \rho^+ & K^{*+} \\ \rho^- & \omega_8/\sqrt{6} - \rho^\circ/\sqrt{2} & K^{*\circ} \\ K^{*-} & \bar{K}^{*\circ} & -2\omega_8/\sqrt{6} \end{pmatrix}$$

The octet and singlet can be combined to form a nonet(41)

$$(V_9)_i^{\ j} = (V_8)_i^{\ j} + (1/\sqrt{3})\delta_i^{\ j}(\omega_1)$$

If we now choose the mixing angle such that $\sin\theta = 1/\sqrt{3}$, corresponding to $\theta \sim 35.5^\circ$ and to a φ mass of about 1000 Mev, then the diagonal terms of V_9 take a particularly simple form. Using this approximation to θ the nonet becomes

$$(V_9)_i^{\ j} = \begin{pmatrix} (\omega + \rho^\circ)/\sqrt{2} & \rho^+ & K^{*+} \\ \rho^- & (\omega - \rho^\circ)/\sqrt{2} & K^{*\circ} \\ K^{*-} & \bar{K}^{*\circ} & -\varphi \end{pmatrix}$$

The pseudoscalar octet ($K\ \bar{K}\ \pi\ \eta$) and unitary singlet $\eta'(960)$ can be combined in a similar manner, though in this case the mixing angle between η and η' is small (about 10°). The pseudoscalar nonet is then (assuming zero mixing angle)

$$(P_9)_i^{\ j} = \begin{pmatrix} \eta/\sqrt{6} + \eta'/\sqrt{3} + \pi^\circ/\sqrt{2} & \pi^+ & K^+ \\ \pi^- & \eta/\sqrt{6} + \eta'/\sqrt{3} - \pi^\circ/\sqrt{2} & K^\circ \\ K^- & \bar{K}^\circ & \eta'/\sqrt{3} - 2\eta/\sqrt{6} \end{pmatrix}$$

Now meson – meson coupling constants are derived from terms such as

$$(V_9)_i{}^j(V_9)_j{}^k(P_9)_k{}^i \quad \text{and} \quad (V_9)_i{}^j(V_9)_j{}^k(V_9)_k{}^i \ .$$

Since the φ is represented by $(V_9)_3{}^3$ it is clear that it can only couple with the strange mesons and never with the π and ρ. In other words, the approximation $\sin\theta = 1/\sqrt{3}$ gives coupling constants $G_{\varphi mm'} = 0$, where m and m' are non-strange mesons. No such restrictions occur for the ω.

We now consider the representation of the baryons. The usual octet representation which is analogous to the meson octets is

$$(B_8)_i{}^j = \begin{pmatrix} \Lambda/\sqrt{6} + \Sigma^\circ/\sqrt{2} & \Sigma^+ & p \\ \Sigma^- & \Lambda/\sqrt{6} - \Sigma^\circ/\sqrt{2} & n \\ \Xi^- & \Xi^\circ & -2\Lambda/\sqrt{6} \end{pmatrix}$$

For our purpose, we take instead the representation obtained by combining three quarks$^{(42, 43)}$ (actually the meson octet can be derived by taking the product of two quarks, so in some ways this representation of the baryons is more consistent with that of the mesons) which is related to $(B_8)_i{}^j$ by

$$B_{ij,k} = \varepsilon_{ijl}(B_8)_k{}^l$$

and the decuplet is D_{ijk} (with the four $N^*(1238)$ states being represented by D_{111}, $D_{112} + D_{121} + D_{211}$, $D_{221} + D_{212} + D_{122}$ and D_{222} $^{(43)}$). We note that the non-strange baryons are not represented by terms containing an index 3.

The coupling of the baryons to the vector meson octet is derived from terms such as

$$\bar{B}^{ij,k}(V_9)_i{}^l D_{jkl} + \bar{D}^{ijk}(V_9)_k{}^l B_{li,j} \ .$$

Now, because the φ is the $(V_9)_3^3$ term and the non-strange baryons do not occur in terms with index 3, the φ can not couple to them, so $G_{\varphi N\bar{N}} = 0$.

Of course, a proper calculation using the correct mixing angle will give coupling constants that are not identically zero, but they are about a factor of a hundred down compared to those of the ω(44).

The most direct evidence for the correctness of the above theory is the strong suppression of $\varphi \to \rho\pi$(41, 45). If we therefore accept that $G_{\varphi\pi\pi} \to 0$ we can make some specific observations concerning the φ production described in chapter four.

In the channels $\Lambda\varphi\pi^0$, $\Sigma^\pm\pi^\mp\varphi$, $\Lambda\pi^+\pi^-\varphi$ it was shown that the φ is in all cases strongly peaked forward and that, within the statistical limitations of the data, the scattering angle of the φ in the $\varphi\pi$ centre of mass is also peaked forward. This peaking is most striking in the combined data for the production and scattering angles (Fig. 6.1). We now offer an explanation of this based on the diagram of Fig. 4.16 with appropriate changes to accomodate the other channels. Besides this diagram there are two other possible cases (neglecting baryon exchange, which is discussed below), one in which the pion is produced at the top vertex with the φ, and the other in which it is produced at the lower vertex, possibly resonantly with the hyperon. We assert that the first of these does not occur because the φ does not couple to pions. The φ is then always produced in a peripheral like manner at a separate vertex by K or K^* exchange, and the other particles, a hyperon and pion(s) may be produced at the same vertex or by a multiperipheral process like that in Fig. 4.16. Also it is clear that there can not be a $\varphi\pi$ or $\varphi\rho$

resonance. Of course, all these observations are first approximations in that the relevant coupling constants are not exactly zero.

It is instructive to look at the corresponding ω channels where the above remarks do not apply. The combined production angular distribution of the ω is not nearly so peaked forward as that of the φ (Fig. 6.2; only $\Sigma^{\pm}\pi^{\mp}\omega$ and $\Lambda\pi^{+}\pi^{-}\omega$ can be shown as $\Lambda\omega\pi^{0}$ can not be fitted, there being two π^{0}s in the final state). In addition there appears to be a significant backward peak, which is also present in $\Lambda\omega$ (Fig. 4.10) but absent in $\Lambda\varphi$. The backward ω peak in $\Lambda\omega$ is attributed to baryon exchange$^{(46)}$ and its absence in the φ channel is expected if the coupling to nucleons is small (so we can neglect baryon exchange in φ channels). The ratio, R, of backward φ production to backward ω production has been calculated by a number of authors using the particle mixing model (for example, Reference 47). They obtain values of R of the order of 0.01 depending upon the precise assumptions made. We can set an experimental limit of $R < 0.1$.

Bronzan and Low$^{(48)}$ put forward an alternative explanation for the different behaviour of the φ and ω when they postulated the existence of a new quantum number, A, which is conserved by strong interactions. They assigned $A(\varphi) = 1$, $A(\omega) = -1$, $A(\pi) = -1$, $A(K) = -1$ and $A(K^{*}) = 1$ so that the decay $\varphi \rightarrow \rho\pi$ was forbidden by A conservation. A further consequence of this rule is that φ production by K^{*} exchange and ω production by K exchange is forbidden. If, however, the explanation for the suppression of $\varphi \rightarrow \rho\pi$ is as has been suggested here, there should be little difference between φ and ω production in $\Lambda\varphi$ and $\Lambda\omega$ but, distinct differences can be expected in channels with π's because the ω can couple to them while the φ can not (the A quantum number would not prevent $\varphi\pi$ coupling).

The production parameters of $\Lambda\varphi$ and $\Lambda\omega$ (forward ω only) are shown in the table below.

Channel	σ_{Total} (μb)	A	ρ_{11}	$\rho_{1\,-1}$	$\mathrm{Re}\rho_{10}$	αP_{Λ}
$\Lambda\varphi$	13 ± 3	2.7 ± .5	.45 ± .07	.39 ± .13	-.07 ± .08	.28 ± .26
$\Lambda\omega$	13 ± 3	1.2 ± .2	.47 ± .1	.02 ± .13	-.02 ± .06	.5 ± .25

(The $\Lambda\omega$ data are taken from Reference 31 and we have used the branching ratios $\varphi \rightarrow K\bar{K}/\mathrm{All}\ \varphi = 0.88$ and $\omega \rightarrow \pi^+\pi^-\pi^0/\mathrm{All}\ \omega = 0.9$.)

The only significant difference between these is the value of ρ_{1-1}, and this may occur because absorption in the final state is different. Both channels appear to go mainly by K^* exchange, thus violating A conservation in the case of the φ.

We have already seen that ω and φ production angular distributions in the channels $\Sigma^{\pm}\pi^{\mp}(\omega \text{ or } \varphi)$ and $\Lambda\pi^+\pi^-(\omega \text{ or } \varphi)$ are very different, which is not expected on the basis of A conservation alone. The spin density matrix elements for the φ and ω in these channels are given in the table below, but no further conclusions can be drawn from them.

Thus we can conclude that the data on φ production in this experiment supports the SU(3) predictions regarding the φ coupling constants, but is in disagreement with selection rules based on A conservation.

Channel	ρ_{11}	$\rho_{1\,-1}$	$\mathrm{Re}\rho_{10}$
$\Sigma^{\pm}\pi^{\mp}\varphi$	.43 ± .12	.17 ± .09	−.04 ± .08
$\Sigma^{\pm}\pi^{\mp}\omega$	.62 ± .11	.24 ± .20	.08 ± .10
$\Lambda\pi^{+}\pi^{-}\varphi$	.36 ± .07	−.01 ± .1	−.02 ± .08
$\Lambda\pi^{+}\pi^{-}\omega$	.32 ± .04	−.09 ± .07	−.06 ± .06

It is interesting to examine the way in which the production parameters of the channel $\Lambda\varphi$ vary with energy. The production angular distributions for the φ at 3, 3.5, 4.1 and 5.5 Gev(49) are shown in Fig. 6.3, and the spin density matrix elements, cross-sections and the slopes of the t distributions are given in the table below and in Fig. 6.5. (The values of the slopes of the t distributions have been calculated from the histogrammed data. It was not possible to do this for the 5.5 Gev data because the histogram bins are larger than the mean value of t.)

Beam Momentum (Gev)	$\sigma_{\varphi\to K\bar{K}}$ (μb)	$\underline{A}$	ρ_{11}	$\rho_{1\,-1}$
3	37 ± 6	1.9 ± .3	.36 ± .07	.15 ± .12
3.5	38 ± 7	2.2 ± .3	.31 ± .05	.07 ± .09
4.1	40 ± 11	2.2 ± .5	.2 ± .1	$.2\,^{+.1}_{-.14}$
5.5	20 ± 6	–	$.45\,^{+.05}_{-.15}$	.23 ± .23

We notice that the distributions are approximately exponential in t and that the width of the peak shrinks with increasing energy. The first observation suggests that the 'Optical Model'(24) may be a reasonable description of the process and the second that the Regge pole exchange model(32) can be applied. These two approaches, though quite different in origin, are not incompatible, and it is interesting and possibly instructive to combine them. The differential cross-section can be written in terms of the two models as

$$\left(\frac{d\sigma}{dt}\right)_{\text{Optical}} = G(s)e^{\gamma(s)t} \quad \text{and} \quad \left(\frac{d\sigma}{dt}\right)_{\text{Regge}} = F(t)s^{2\alpha(t)-2}$$

These two equations are attempts to explain the same physical situation so thay must be equal. Equating them is the same as forcing the Regge description of the t distribution to be pure exponential. If we assume that $\alpha(t) = \alpha_o + \alpha_1 t$, then we obtain

$$\frac{d\sigma}{dt} = F_o s^{2\alpha_o - 2} e^{(2\alpha_1 \ln s + k)t}$$

where F_o and k are constants. Now, if we plot the slopes of the t distributions against ln(s) we should obtain a straight line whose slope is that of the Regge trajectory contributing to this channel (Fig. 6.6). This slope is only meaningful if either there is only one trajectory contributing, or if the contributing trajectories all have the same slope. The data appears to be in extremely good agreement with this simple analysis, the line on the plot being that expected if we take the usual value of the slope of a trajectory as 1 Gev^{-2}. Further, if we extrapolate dσ/dt to t = 0 then

$$\ln\left(\left.\frac{d\sigma}{dt}\right|_{t=0}\right) = \ln F_o + (2\alpha_o - 2)\ln s$$

so we can plot $\ln(d\sigma/dt|_{t=0})$ against $\ln(s)$ and hope to obtain a straight line. However, the variation of cross-section with energy is such that this will not occur (Fig. 6.5). In defence of the theory it must be pointed out that the experimental values do not lie on a smooth curve as they might be expected to on the grounds of experience with other channels (such as $\Lambda\omega$). There are two possible reasons for this. First, that the experimental values might be bad, and second that there is an s-channel resonance, which seems unlikely though not impossible. Of course the theory itself is rather crude because it contains only an 'effective trajectory' where two are probably occurring. Moreover, the ratio of the two trajectories' contributions to the cross-section is not necessarily constant with change of energy, so that α_0 will not be constant. Although not directly relevant, it is worth remarking by way of circumstantial evidence for the theory that Morrison(50) has plotted $\ln(\sigma)$ against $\ln(p \text{ incident})$ for many two body processes, but not including $\Lambda\varphi$, and found that the experimental points lie on straight lines. Morrison himself observes that the slope of such lines should be approximately $2\alpha(0) - 2$ as small values of t yield most of the cross-section.

There are two obvious disadvantages to this semi-phenomenological approach to testing the Regge description of two body processes. The first is that the t distribution is not truly exponential, as for example the vector exchange contribution must fall to zero in the forward direction. The second is that several Regge trajectories may be expected to contribute to the process. In this case the trajectories corresponding to the K and $K^*(890)$ are probably dominant, and any contribution from higher trajectories (e.g. $K^*(1400)$) can be neglected. α_o will vary with energy because the K and K^* trajectories have different intercepts at $t = 0$, but its value should lie between the intercepts for the two trajectories i.e. between -.24 and 0.20. Examination of the variation of spin density matrix elements with energy (Fig. 6.5) indicates that the proportion of vector exchange is increasing with energy. Hence the exponent of the energy variation of the cross-section should increase with energy towards a maximum of -1.6. Further, more accurate data at several energies would be invaluable.

One last point, even if the above was found to be an accurate description of the data, it does not give much information about the real nature of the physical processes concerned, but the establishing of a systematic trend is a useful first step.

6.2 The Double Peripheral Model

We have seen in chapter four that the idea of the double (or multi-) peripheral model can be useful as a means of examining the data. Its validity as a specific production mechanism for the channels $\Lambda\varphi\pi^o$, $\Sigma^\pm\pi^\mp\varphi$, $\Lambda\bar{K}K^*$ and $\Sigma^-K^+\bar{K}^o$ is however limited. In the case of the φ channels we showed that the φ must be produced at a separate vertex but the pion and hyperon may come from the same vertex, either resonantly or non-resonantly. However, if we combine the hyperon - pion scattering angles the forward peaking of the hyperon is clear (Fig. 6.7). It would therefore seem that the double peripheral mechanism does contribute to these channels.

The $\Lambda\bar{K}K^*$ channel is somewhat different. Here the Λ is clearly peripheral but the peripheral nature of the $\bar{K}K^*$ system is not established. It is interesting to compare the present $\bar{K}K^*$ mass spectrum with that of a recent paper on a 5 Gev K^-p experiment(29) (Fig. 6.4). The peaks at 1.45 Gev and 1.58 Gev occur in both. The 1.45 Gev peak could be interpreted as the E meson, but the second peak does not correspond to any known resonance. It would be worth examining this with greater statistical accuracy.

6.3 Negative Hyperons

In the channels $\Sigma^-K^+\bar{K}^0$ and Ξ^-K^+ there appears to be clear evidence for hyperon exchange. The Ξ^-K^+ result has been observed in other experiments (e.g. at 3.5 Gev and at 2.24 Gev(51,25)) and has been interpreted as being dominated by $Y_1^*(1385)$ exchange(55). In this experiment there is one Ξ^- produced in the backward hemisphere, and in a 3.5 Gev experiment(51) there is a backward peak. This backward peak has not been explained by hyperon exchange.

The peripheral nature of the production process is evident even in the high multiplicity Ξ^- events. It was shown that the mechanism was such that the Ξ^- and K tended to be produced in opposite directions, suggesting a hyperon exchange process when the Ξ^- goes forward and a double-strange meson exchange when the Ξ^- goes backwards. The backward Ξ^- observed in these channels may be compared to the backward peak observed in Ξ^-K^+ at 3.5 Gev.

Evidence for a strangeness 2 meson was presented at the 1965 Dubna conference(52). A three standard deviation peak at ~ 1.3 Gev was observed in the KK mass spectrum produced by 3 and 3.5 Gev K^+ mesons. Since then, a further experiment and compilation of world data(53) has shown that there is no significant peak in the KK mass spectrum up to about 2 Gev. In view of the behaviour of the Ξ^- it would be useful if more data on the KK mass spectrum were available at higher energies.

The $Y_1^{*\pm}(1385)\pi^{\pm}$ Enhancement at 1650 Mev

It is impossible to say whether this is a resonance or kinematic effect from the present data alone. The flat production and decay angular distributions give no definite information about the spin and parity of the enhancement.

In a recent paper(54) an enhancement at 1680 Mev in the $\Lambda\pi^+$ effective mass in the final state $\Lambda\pi^+\pi^-$ produced by 5.5 Gev K^- is claimed as a resonance. A $Y_1^{*+}(1385)\pi^\circ$ peak, presumed to be another decay mode of the same object, is also seen in the final state $\Lambda\pi^+\pi^-\pi^\circ$. A similar $\Lambda\pi^+$ peak is also observed in $\Lambda\pi^+\pi^-$ in the data for this experiment(31). The present 1650 peak is only observed in the neutral state, no positive counterpart being seen, so it is not clear that there is any relation between the peaks. In any case, none of the data is adequate to permit a determination of the quantum numbers of the state, and until that is done it is not possible to say with certainty that such peaks correspond to resonances or to ascertain that they are different production and decay modes of the same object.

Fig. 6.1

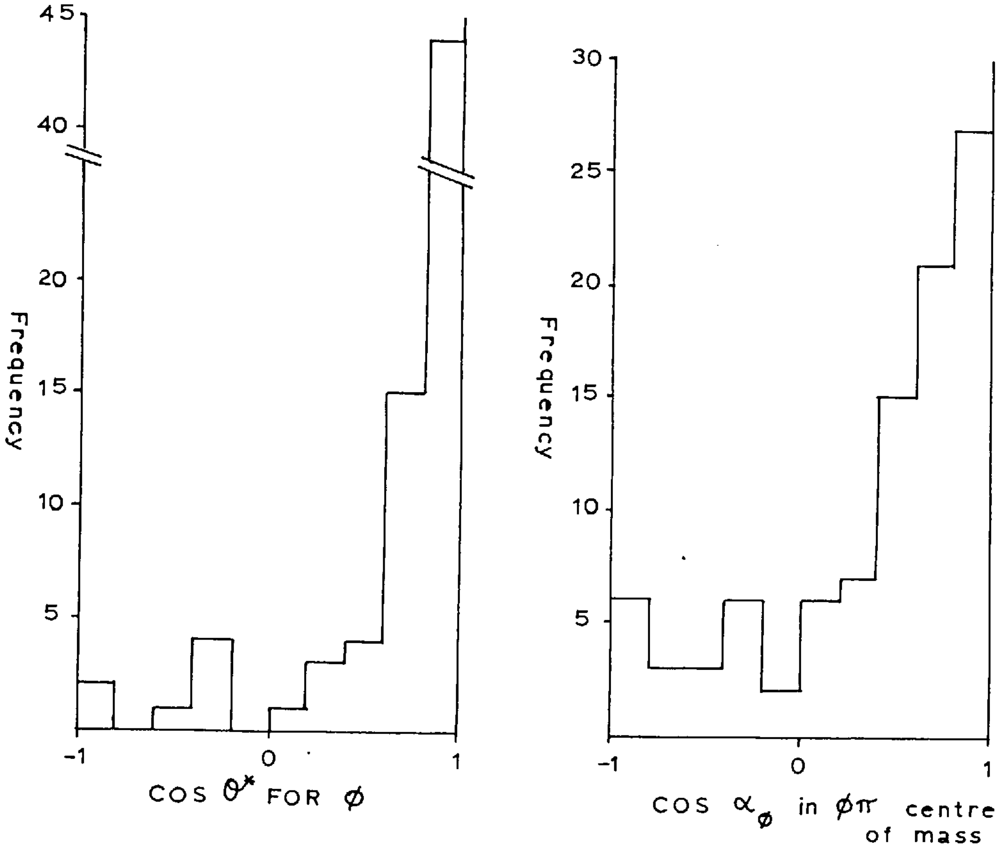
45
40
20
15
10
5
Frequency
-1
0
1
cos θ* FOR φ
30
25
20
15
10
5
Frequency
-1
0
1
cos α_φ in φπ centre of mass

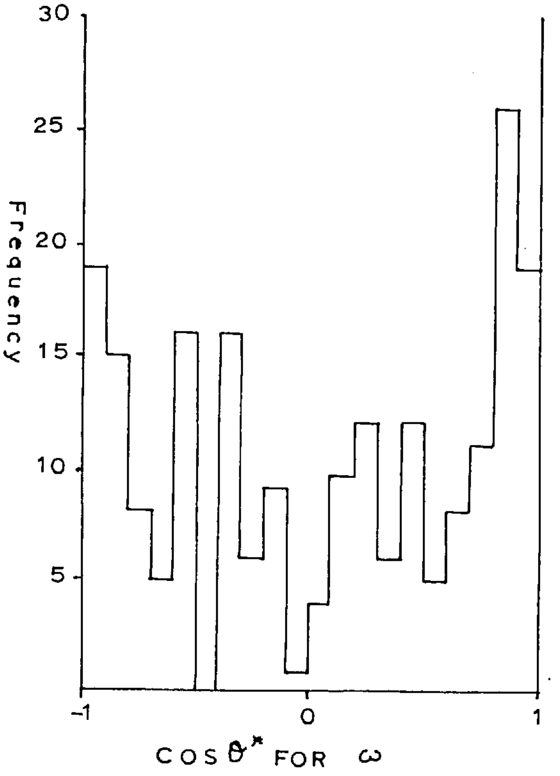
30
25
20
15
10
5
Frequency
-1
0
1
cos θ* FOR ω

Fig. 6.2

Fig. 6.3

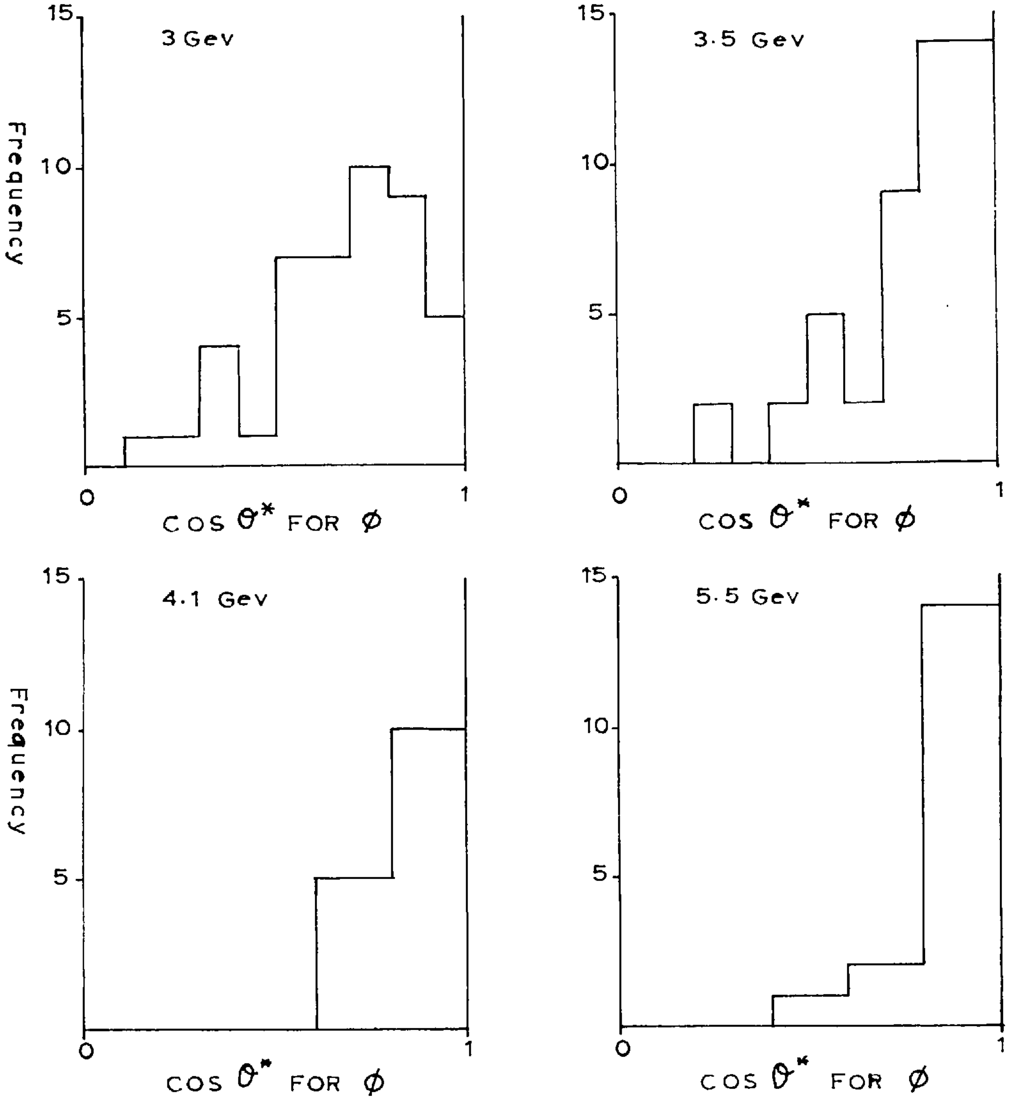
3 Gev
3.5 Gev
4.1 Gev
5.5 Gev
Frequency
15
10
5
0
1
cos θ^* FOR ϕ

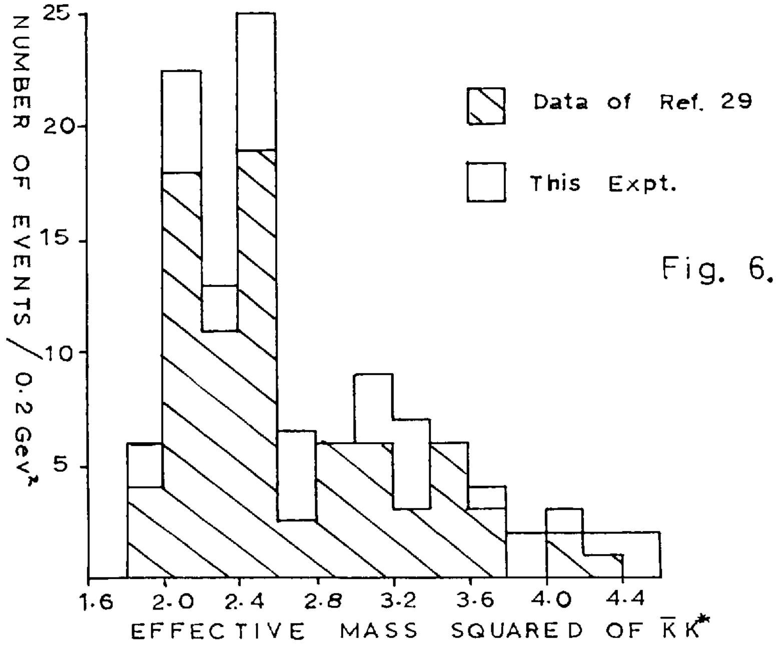
Data of Ref. 29
This Expt.
NUMBER OF EVENTS / 0.2 Gev^2
25
20
15
10
5
1.6
2.0
2.4
2.8
3.2
3.6
4.0
4.4
EFFECTIVE MASS SQUARED OF $\overline{K}K^*$

Fig. 6.4

Fig. 6.5

$K^-p \rightarrow \Lambda\phi$

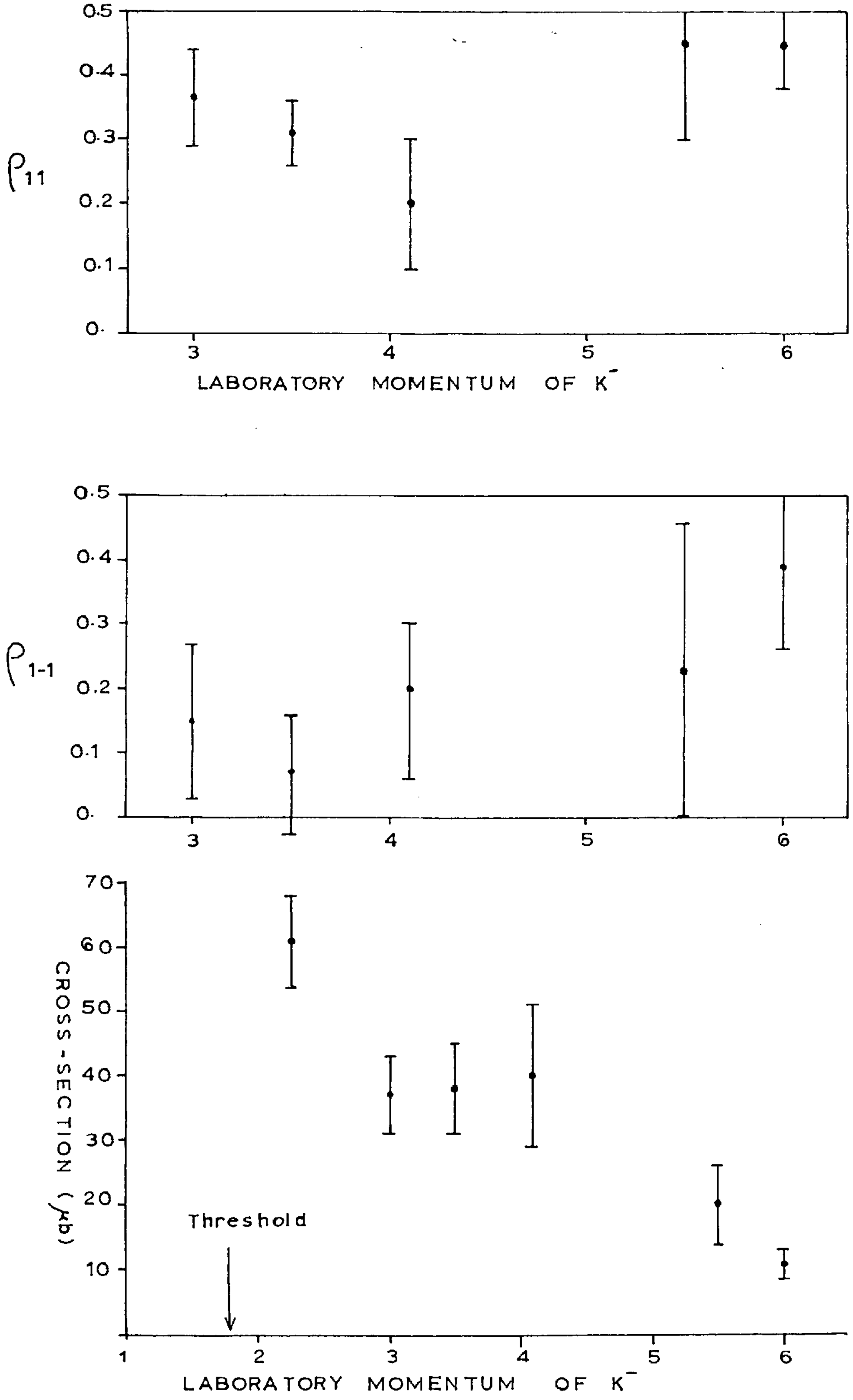

Fig. 6.6

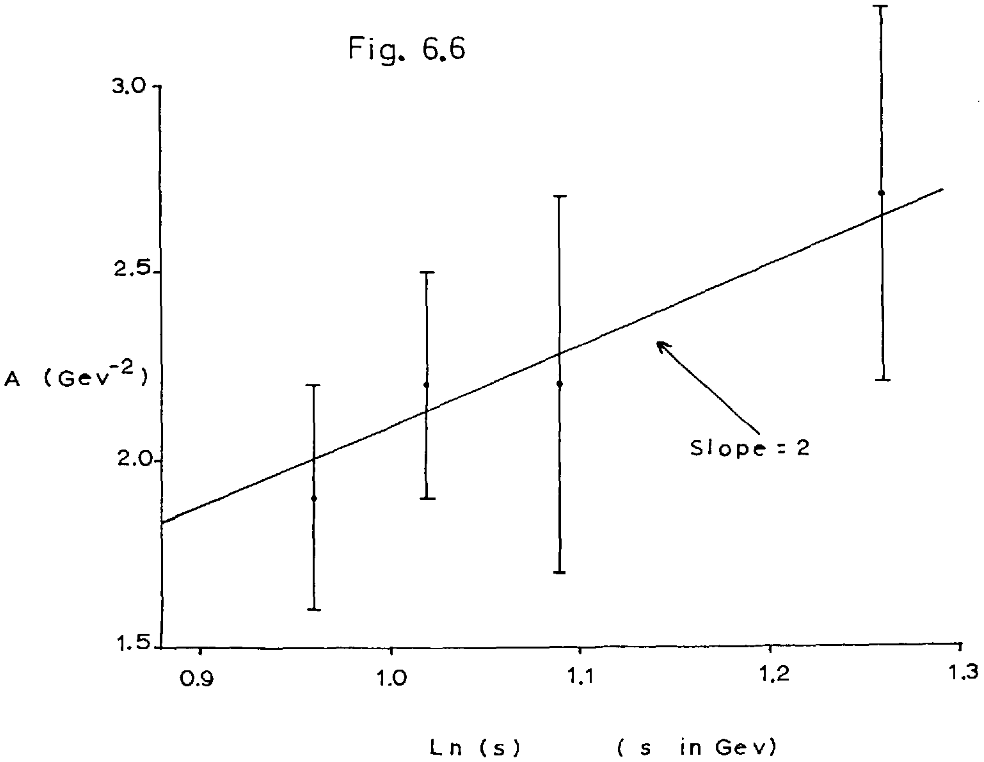

Fig. 6.7 COMBINED Yπ SCATTERING ANGLE FOR $\Lambda\phi\pi$, $\Sigma^{\pm}\pi^{\mp}\phi$

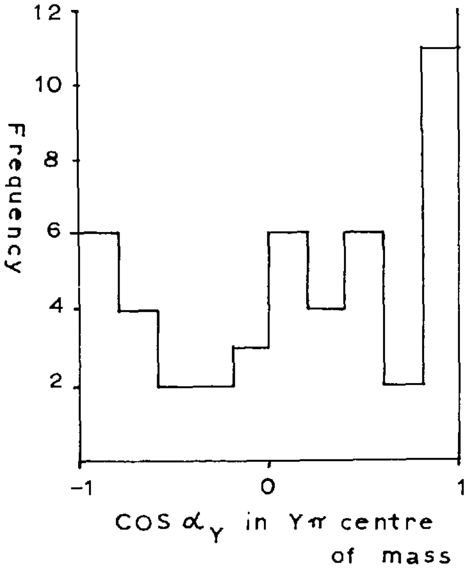

ACKNOWLEDGEMENTS

I wish to express my gratitude to Professor C. C. Butler for the opportunity of working in the Imperial College bubble chamber group, and to the Science Research Council for their financial support while I was a research student.

I further wish to thank my supervisor, Dr. S. J. Goldsack, and my colleagues Kenneth Paler and Pratip Chaudhuri for many stimulating discussions and general encouragement; also Drs. A. Eskreys and M. Saeed, who have now left the group, and my colleagues in the collaborating groups.

Thanks are also due to Mrs. S. Hulbert and Miss A. Tomlin for the book-keeping, to Mr. E. Kerr for assistamce with the computing, to Dr. D. B. Miller for his work on the measuring machines and associated equipment and to the rest of the technical staff who assisted us.

The staff of the Imperial College Computer Unit are thanked for their services and for allowing me to operate the computer myself when necessary.

Finally, I wish to thank my wife for her general encouragement and assistance in the final preparation of this work.

REFERENCES

The following abbreviations are used: N.C. for Nuovo Cimento, P.R. for Physical Review, P.R.L. for Physical Review Letters and P.L. for Physics Letters.

1. V. E. Barnes et al. P.R.L. 12, 204, 1964.
2. D. C. Colley et al. P.L. 19, 152, 1965.
3. E. Ferrari and F. Selleri Supp. N.C. 24, 453, 1962.
   H. Pilkuhn CERN 65-24.
4. E. Keil and W. W. Neale CERN / TC / 02 63-3.
5. Riddiford et al. Proc. Int. Conf. on High Energy Acceleration and Instrumentation CERN 1959.
6. W. T. Welford Applied Optics 2, 981, 1963.
   W. T. Welford Applied Optics 2, 1037, 1963.
7. The Magnetic Field of the British 1.5 m. Bubble Chamber CERN / TC / NBC 63-2.
8. S. L. Baker Ph.D. Thesis, University of London 1965.
9. Powell Report to D.S.I.R.
10. J. W. Burren and J. Sparrow Rutherford Lab. Report NIRL / R / 14.
11. J.W. Burren et al. Science Research Council Report.
12. W. E. Humphrey Alvarez Group Memo. 111, Sept. 1959.
13. A. G. Wilson Rutherford Lab. Report NIRL / R / 42.
14. A. G. Wilson Rutherford Lab. Report NIRL / M / 38.
15. J. M. Scarr Rutherford Lab. internal Report 1965.
16. G. A. Smith et al. P.R.L. 10, 138, 1963.

17. K. Gottfried and J. D. Jackson N.C. 33, 309, 1964.

18. J. Allison D.Phil. Thesis Oxford University 1966.

19. F. T. Solmitz UCRL Report 11413.

20. W. W. Neale Private Communication.

21. W. Blum and G. Dehm Collaboration Report (Unpublished).

22. W. Galbraith et al. P.R. 138, B913, 1965.

23. V. E. Barnes et al. P.R.L. 15, 322, 1965.

24. U. Maor CERN / TC / PHYSICS 66-26.

25. G. W. London et al. P.R. 143, 1034, 1966.

26. J. Joseph and H. Pilkuhn N.C. 33, 1407, 1964.

27. Chan Hong-Mo et al. CERN 66 / 1260 / 5 - Th 719.

28. D. J. Crennell et al. Berkeley Conference 1966.

29. V. E. Barnes et al. Berkeley Conference 1966.

30. D. J. Crennell et al. P.R.L. 16, 1025, 1966.

31. K. Paler Ph.D. Thesis University of London 1967.

32. S. C. Frautschi et al. P.R. 126, 2204, 1962.

K. Gottfried and J. D. Jackson P.L. 8, 144, 1964.

33. V. Barger and D. Cline Berkeley Conference 1966.

34. G. Höhler et al. P.L. 20, 79, 1966.

35. D. Amati et al. N.C. 26, 896, 1962.

36. L. Van Hove CERN 65 - 24 Volume III

37. L. Gray et al. P.R.L. 17, 501, 1966.

38. M. Gell-Mann and Y. Ne'eman "The Eightfold Way" published by Benjamin 1965.

S. Okubo Prog. Theor. Phys. (Kyoto) 27, 949, 1962.

39. J. J. Sakurai P.R.L. 9, 472, 1962.
40. L. C. Biedenharn CERN 65 - 41.
41. S. Okubo P.L. 5, 165, 1963.
42. V. F. Weisskopf CERN 66 - 19.
43. H. Sugawara and F. Von Hippel P.R. 145, 1331, 1966.
44. S. L. Glashow and R. H. Socolow P.R.L. 15, 329, 1965.
45. J. S. Lindsey and G. A. Smith P.L. 20, 93, 1966.
46. L. Lyons N.C. 43, 888, 1966.
47. H. M. Fried and J. G. Taylor P.R.L. 15, 709, 1965.
R. J. Rivers P.R. 150, 1256, 1966.
48. J. B. Bronzon and F. E. Low P.R.L. 12, 522, 1964.
49. J. Goldberg Oxford Conference 1965.
Mott et al. Preprint submitted to P.R.L.
50. D. R. O. Morrison P.L. 22, 528, 1966.
51. A. A. Z. Ahmad Ph.D. Thesis University of London 1965.
52. M. Ferro-Luzzi et al. P.L. 17, 155, 1965.
53. T. Joldersma et al. P.R.L. 17, 716, 1966.
54. M. Derrick et al. P.R.L. 18, 266, 1967.
55. P. B. James Preprint.